University of Groningen

High performance motion control for cryogenic nanopositioning mechanisms

Huisman, Robert

IMPORTANT NOTE: You are advised to consult the publisher's version (publisher's PDF) if you wish to cite from it. Please check the document version below.

Document Version
Publisher's PDF, also known as Version of record

Publication date:
2016

Link to publication in University of Groningen/UMCG research database

Citation for published version (APA):
Huisman, R. (2016). *High performance motion control for cryogenic nanopositioning mechanisms: Application to the METIS Cold Chopper mechanism*. [Thesis fully internal (DIV), University of Groningen]. University of Groningen.

Copyright
Other than for strictly personal use, it is not permitted to download or to forward/distribute the text or part of it without the consent of the author(s) and/or copyright holder(s), unless the work is under an open content license (like Creative Commons).

The publication may also be distributed here under the terms of Article 25fa of the Dutch Copyright Act, indicated by the "Taverne" license. More information can be found on the University of Groningen website: https://www.rug.nl/library/open-access/self-archiving-pure/taverne-amendment.

Take-down policy
If you believe that this document breaches copyright please contact us providing details, and we will remove access to the work immediately and investigate your claim.

Downloaded from the University of Groningen/UMCG research database (Pure): http://www.rug.nl/research/portal. For technical reasons the number of authors shown on this cover page is limited to 10 maximum.

Download date: 05-05-2023

High performance motion control for cryogenic nanopositioning mechanisms

Application to the METIS Cold Chopper mechanism

Robert Huisman

rijksuniversiteit
groningen

SRON
Netherlands Institute for Space Research

The research described in this thesis has been carried out at the Faculty of Mathematics and Natural Sciences, University of Groningen, The Netherlands and at the Netherlands Institute for Space Research (SRON) in Groningen.

Cover: Part of the Heart nebula-IC 1805.
Source: [Online] Available from: http://www.mikesastrophotos.com/nebula/heart-nebula-ic-1805 [Accessed 1^{st} January 2016]. Image is blurred. Lissajous profile, generated during the test campaign with the METIS Cold Chopper mechanism, reveals parts of the original sharp image.

Printed by: Ipskamp Drukkers B.V.
Enschede, The Netherlands

ISBN (book): 978-90-367-8601-0
ISBN (e-book): 978-90-367-8602-7

rijksuniversiteit
groningen

High performance motion control for cryogenic nanopositioning mechanisms

Application to the METIS Cold Chopper mechanism

Proefschrift

ter verkrijging van de graad van doctor aan de
Rijksuniversiteit Groningen
op gezag van de
rector magnificus prof. dr. E. Sterken
en volgens besluit van het College voor Promoties.

De openbare verdediging zal plaatsvinden op

vrijdag 12 februari 2016 om 14.30 uur

door

Robert Huisman

geboren op 19 december 1973
te Assen

Promotores
Prof. dr. B. Jayawardhana
Prof. dr. ir. J.M.A. Scherpen

Beoordelingscommissie
Prof. dr. R.F. Peletier
Prof. dr. C. De Persis
Prof. dr. ir. M. Steinbuch

To my parents: Jacob and Fokje Willemina Huisman

To my family: Ilse, Liv and Eva

"I don't pretend we have all the answers. But the questions are certainly worth thinking about."
- Arthur C. Clarke

Contents

Acknowledgments **xi**

List of figures **xiii**

List of tables **xv**

Acronyms **xvii**

1 Introduction **1**
1.1 Astronomical observations . . . 1
1.1.1 Telescope developments . . . 2
1.1.2 Noise sources in astronomical observations . . . 3
1.1.3 The scanning technique . . . 3
1.2 High performance motion control . . . 4
1.2.1 Control solutions to the servomechanism problem . . . 5
1.2.2 Control solutions for point-to-point control . . . 6
1.3 Motivation . . . 7
1.3.1 Chopper mechanism for the HIFI instrument on board the Herschel Space Observatory . . . 8
1.3.2 2D chopper mechanism for the METIS instrument of the European-Extremely Large Telescope . . . 10
1.4 Aim . . . 11
1.5 Contributions . . . 11
1.6 Thesis outline . . . 12
1.7 List of publications . . . 13

2 Preliminaries on control theory **15**
2.1 Classical output regulation for linear systems . . . 15
2.2 Output regulation for hybrid systems . . . 17
2.2.1 Hybrid systems . . . 17
2.2.2 Hybrid output regulation . . . 18
2.3 Repetitive control strategy . . . 20

3 Hybrid control strategy for output regulation in high performance applications 23
3.1 Chopper scanning problem formulation . . . 23
3.2 Introduction to the proposed hybrid control strategy . . . 25
3.3 Hybrid system description . . . 26
3.4 Hybrid output regulation for scanning . . . 30
3.4.1 Practical stability . . . 33
3.5 Practical FF design by offline optimization . . . 34
3.6 Relation to other high performance control strategies . . . 35
3.7 Concluding remarks . . . 37

4 Cryogenic mechatronic design of the HIFI Focal Plane Chopper 39
4.1 HIFI Focal Plane Chopper . . . 39
4.1.1 HIFI-FPC requirements . . . 39
4.1.2 Instrument description . . . 40
4.1.3 Control design . . . 46
4.2 Considerations for cryogenic HIFI-FPC design . . . 52
4.2.1 Impact of cryogenic environment on material choice . . . 52
4.2.2 Cryogenic mechanical design of the HIFI-FPC . . . 53
4.2.3 Thermal issues in control design of the HIFI-FPC . . . 56
4.2.4 Cryogenic testing . . . 58
4.3 HIFI-FPC performance . . . 59
4.4 Concluding remarks . . . 60

5 Synthesis and application of hybrid controller to HIFI-FPC 61
5.1 System identification . . . 61
5.2 Experimental results for square wave chopping . . . 62
5.3 Simulation of OTF observation . . . 64
5.4 Concluding remarks . . . 67

6 High performance motion control of the METIS Cold Chopper Mechanism 69
6.1 MCCD mechanism description . . . 69
6.1.1 Voice coil actuators . . . 72
6.1.2 Position sensors . . . 72
6.2 System identification . . . 73
6.2.1 Sensors and actuator characteristics . . . 73
6.2.2 Plant dynamics . . . 73
6.2.3 Non linear behaviour . . . 76
6.3 Control synthesis . . . 79
6.3.1 Hybrid controller . . . 79
6.3.2 Repetitive controller . . . 81
6.4 Performance . . . 83
6.4.1 Positional stability . . . 84
6.4.2 Settling time . . . 85
6.4.3 Robustness to thermal variations . . . 87
6.5 Implementation issue: Stability of repetitive controller . . . 88

6.6 Concluding remarks 89

7 Conclusions and future work **91**
7.1 Conclusions and outlook 91
7.2 Future work 92

A Experimental setup HIFI-FPC **95**

B Experimental setup MCCD **97**

C MCCD lifetime test results **99**

D MCCD project summary **101**
D.1 MCCD project objectives 101
D.2 MCCD project team 101

Bibliography **102**

Summary **109**

Samenvatting **111**

Acknowledgments

First of all, I would like to express my sincerest gratitude to my supervisor Bayu Jayawardhana. I could count on you day and night to discuss basically everything I encountered during my research and you always provided me with valuable new insights. I learned a lot from you and I admire your patience.

I would like to thank Jacquelien Scherpen for providing me with the opportunity to pursue a PhD and for her tranquility and advice during hectic times.

Frank Helmich, Henk van der Linden and Wolfgang Wild, thank you for motivating me to take this path and for making this possible within SRON.

I could not have done all the experimental work without the valuable help of many of my colleagues at SRON. Wim Horinga, Bert Kramer, Heino Smit, Martin Stokroos, Henk Ode, Duc van Nguyen, Rob van der Schuur and Jarno Panman. Thanks a lot guys, it is good to know that I can count on you. A special thanks goes out to Ad Nieuwenhuizen and Martin Eggens. Ad, thank you for all your work on the HIFI chopper. Martin, thank you for your contributions to both the HIFI and METIS chopper projects and for being a good friend.

I would like to thank Jasper Boomer for his experimental work on the HIFI chopper. Jasper, you did a great job in your little dark corner of the DTPA lab.

Furthermore, I would like to thank Tom Oomen and Joost Bolder from TU Eindhoven for their support with the implementation of the repetitive controller.

My thanks also go out to the METIS team: Bernhard Brandl, Frank Molster, Rieks Jager, Lars Venema, Gabby Kroes, Huub Janssen, Sander Paalvast, Maurice Teuwen, Teun van den Dool, Martin Eggens, Jaap Evers and Bayu Jayawardhana. Thanks for the productive and constructive technical discussions, your support and the great team work. Sander, I want to especially thank you for all your help.

Thanks to all my great colleagues both at SRON and DTPA. I hope that my colleagues at SRON still remember who I am. I promise not to do this again...

I would like to express my gratitude to Rens Waters, Roel Gathier, Frank Helmich, Henk van der Linden, Pieter Dieleman and Gert de Lange. Thank you for making this possible within SRON and for your patience. Especially during a personally difficult period in 2014, the support and flexibility from SRON was invaluable to me. Gert and Yvonne, a special thanks to you for your help during this period.

Erik, Liz, Susanna and Maya thank you for your warm support. Mom and dad, thank you for your unconditional support and for always believing in me and providing me with all the beautiful opportunities in life.

Ilse, Liv and Eva you are the sunshine of my life. Looking at my lovely daughters always puts a smile on my face and gives me the strength to go on. Ilse, it is a privilege to go through life with such a strong and beautiful person and I can't thank you enough for everything you did.

Robert Huisman,
Wiesmoor, January 2016.

List of Figures

1.1 The electromagnetic spectrum 1
1.2 Opacity of the earth's atmosphere to electromagnetic radiation 2
1.3 Basic high performance motion control block diagram 5
1.4 Photograph of the HIFI-FPU flight model 8
1.5 Schematic drawing of the interior of the HIFI-FPU 9
1.6 Artist's impression of the E-ELT 10

2.1 Repetitive control layout 20
2.2 Bode magnitude plot of repetitive loop delay line 21

3.1 Hybrid controller layout 26
3.2 Example of reference profile on hybrid time domain 32
3.3 Comparison of fast reference tracking for different control strategies 36
3.4 Effect of step time of reference profile on settling time of system 37

4.1 Photo of the HIFI Focal Plane Chopper 41
4.2 HIFI-FPC actuator 42
4.3 Schematic drawing of HIFI-FPC LVDT 43
4.4 Cross section of HIFI-FPC LVDT position sensor 44
4.5 C-flex Inconel 718 flexural pivot 44
4.6 Close up of pivot clamp construction of HIFI-FPC 45
4.7 Block diagram of the closed loop HIFI-FPC system 48
4.8 Z-domain root locus plot of the complete HIFI-FPC system 49
4.9 Gain and phase margin of the final HIFI-FPC system 50
4.10 Relation between actuator current and LVDT readout of HIFI-FPC 50
4.11 Relation between actuator current and chop angle of HIFI-FPC 51
4.12 Relation between chop angle and LVDT readout of HIFI-FPC 51
4.13 HIFI-FPC open loop step response at room and cryogenic temperatures 56
4.14 Bode plot of original 10 kHz design LVDT response 57
4.15 Closed loop step response of HIFI-FPC mechanism in space 60

5.1 Square wave chopping reference signal on hybrid time domain 62

5.2 Experimental result for HIFI-FPC chopping with hybrid controller 63
5.3 Close up at stable observation position during chop observation 63
5.4 OTF reference signal on hybrid time domain 64
5.5 Simulation result OTF observation with HIFI-FPC 65
5.6 Error convergence during OTF observation 66
5.7 Error of OTF observation after convergence 66

6.1 Photo and cross section of MCCD 70
6.2 Schematic drawing of the MCCD 70
6.3 Conceptual drawing of the MCCD 71
6.4 Calibration result MCCD 73
6.5 Bode magnitude plot of open loop MCCD for θ_x-direction 74
6.6 Non collocated lumped mass system representative for the dominant 8^{th}-order θ_x-dynamics. The actuator force is applied at the triangular support structure and displacements are measured at the mirror surface relative to the MCCD base frame. 75
6.7 Observed hysteresis in θ_x and fitted model 76
6.8 Non linear MCCD plant model 77
6.9 Effect of hysteresis on feedforward response 79
6.10 Complementary sensitivity and sensitivity function of MCCD 81
6.11 Simulation and experimental results of chopping applying repetitive control . . . 82
6.12 2D positional stability for 8.5 mrad chop observation with MCCD 84
6.13 Histogram of 2D positional stability for 8.5 mrad chop observation with MCCD . 85
6.14 Experimental result of chopping applying hybrid and repetitive controller 86
6.15 Tracking error during 5Hz chop after convergence (after 4.805 sec at θ_y= 8.5 mrad position). Tracking of the hybrid controller is limited due to the non linearities which are not accounted for in the FF design. 86
6.16 Repeatability of chopped positions 87
6.17 Bode magnitude plot of plant at 77K and 63.5K 88
6.18 Simulation of chopping applying repetitive, MbFF and hybrid control 89

A.1 Schematic drawing of experimental setup for HIFI-FPC 95
A.2 Photo of HIFI-FPC test setup 95

B.1 Schematic drawing of experimental setup for MCCD 97

C.1 Lifetime test result MCCD 99

List of Tables

1.1 MCC requirements 11

3.1 Exo-state initial conditions for different observing modes 29
3.2 Plant configurations studied to illustrate the effect of reference step time on settling 36

4.1 HIFI-FPC requirements and realized performance 40
4.2 Relation between HIFI-FPC chop angle and orientation of the HIFI beam 40
4.3 Lot acceptance test program for pivot flight production 46

5.1 Step response and overshoot for chopping with original and hybrid controller . . 64

6.1 Dominant resonances of MCCD for θ_x 74
6.2 Laplace transform coefficients for all 3 DoF's of MCCD dynamics 76
6.3 Fitted parameters of non linear MCCD model 78
6.4 Influence of plant resonances on settling 80
6.5 Tuned parameters of repetitive controller 82
6.6 MCCD requirements and realized performance 83
6.7 Percentage of chopped angles within 1.7 μrad from mean chopped angle 85

Acronyms

bcc	body-centered-cubic
BeCu	BerylliumCopper
CBB	Cold Black Body
CEA Saclay	Commissariat l'énergie atomique et aux énergies alternatives (the French Alternative Energies and Atomic Energy Commission in Saclay)
CTE	Coefficient of Thermal Expansion
DoF	Degree of Freedom
EBZPETC	Extended Bandwidth Zero Phase Error Tracking Control
E-ELT	European-Extremely Large Telescope
EI	Extra Insensitivity
emf	electromotive force
ESA	European Space Agency
ESFRI	the European Strategy Forum on Research Infrastructures
ESO	European Southern Observatory
ETH Zürich	Eidgenössische Technische Hochschule Zürich
fcc	face-centered-cubic
FEA	Finite Element Analysis
FEM	Finite Element Method
FF	Feedforward
FPC	Focal Plane Chopper
FPU	Focal Plane Unit
HBB	Hot Black Body
HIFI	Heterodyne Instrument for the Far Infrared
ILC	Iterative Learning Control
IR	Infrared
JA	Jiles-Atherton
JPE	Janssen Precision Engineering
JPL	Jet Propulsion Laboratory
KU Leuven	Katholieke Universiteit Leuven
LVDT	Linear variable differential transformer
M1	Telescope primary mirror

M2	Telescope secondary mirror
MbFF	Model based feedforward
MCC	METIS Cold Chopper
MCCD	METIS Cold Chopper Demonstrator
METIS	Mid-Infrared E-ELT Imager and Spectrograph
MIMO	multiple-input multiple-output
MPIA	Max Planck Institute for Astronomy in Heidelberg
NOVA	Nederlandse Onderzoekschool voor Astronomie (Dutch research school for astronomy)
NWO	Netherlands Organisation for Scientific Research
OTF	On The Fly
PACS	Photoconducting Array Camera and Spectrometer
RMS	Root-Mean-Square
S	sensitivity function
SI	Specified Insensitivity
SISO	single-input single-output
SPICA	Space Infrared Telescope for Cosmology and Astrophysics
SRON	Netherlands Institute for Space Research
T	complementary sensitivity function
TMT	Thirty Meter Telescope
TNO	De Nederlandse Organisatie voor toegepast-natuurwetenschappelijk onderzoek
UK-ATC	United Kingdom Astronomy Technology Centre in Edinburgh
U Vienna	Universität Wien in Vienna
VCA	Voice Coil Actuator
ZPETC	Zero Phase Error Tracking Control
ZVD	Zero Vibration and Derivative

Chapter 1

Introduction

In this chapter we provide the general background relating to our application of scanning in astronomical observations and to the field of high performance motion control. We discuss the motivation for our study, provide an outline of the thesis and summarize the contributions of the presented work.

1.1 Astronomical observations

Although we can learn about the universe by sending spacecrafts to the sun, other planets, moons and comets, or by observations of neutrinos and gravitational waves, the vast majority of astronomical studies is based on the information brought to us in the form of electromagnetic radiation. The electromagnetic spectrum shown in Fig. 1.1, ranging from the very long wavelength radio waves to the short wavelength and high energetic gamma-rays, can carry information about very different processes in the universe. Low energetic radio waves are for example produced by neutral atomic hydrogen in the interstellar medium, whereas so called gamma ray bursts are thought to be generated in the extremely energetic processes of a supernova or the merger of a binary neutron star system.

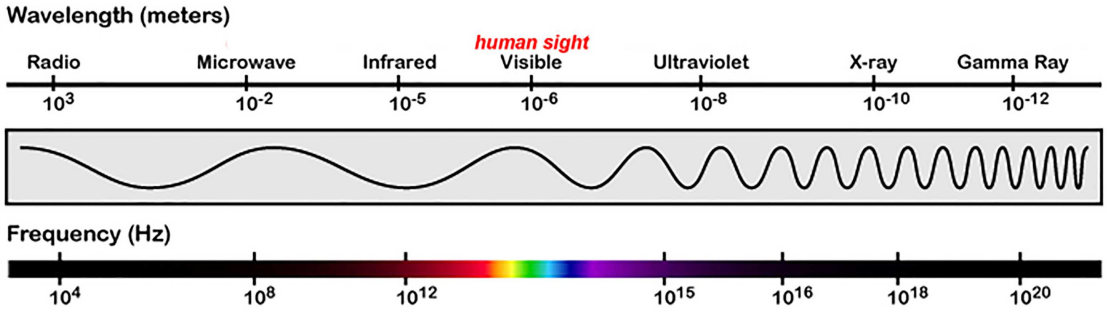

Figure 1.1: The electromagnetic spectrum showing the coarse subdivision of the radiation into the different wavelength regimes. Source: JPL. [Online] Available from: http://planck.caltech.edu/epo/epo-cmbDiscovery3.html [Accessed 20^{st} August 2015]

Not all radiation from space can reach the surface of the earth. In fact, except for the visible, the radio wavelengths and some bands in the infrared (IR), all radiation is absorbed by the atmosphere, as can be seen in Fig. 1.2. This makes it often necessary to observe from high

and dry places (like the Atacama desert in Chile) or even to observe from a balloon, plane or satellite.

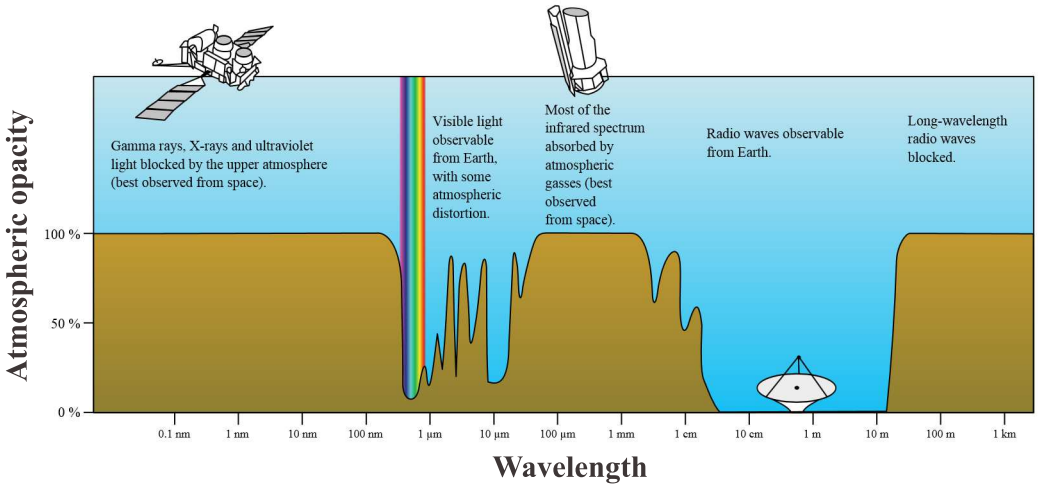

Figure 1.2: Opacity of the earth's atmosphere to electromagnetic radiation. Observations from earth are only possible in the visible, at radio wavelengths and in some bands of the infrared. Source: Wikipedia. [Online] Available from: https://en.wikipedia.org/wiki/Absorption_(electromagnetic_radiation). [Accessed 20^{st} August 2015]

1.1.1 Telescope developments

Different frequency regimes require different telescopes, instrumentation and detection techniques to collect and process the information. Detectors for example, are typically optimized for a small wavelength range, and requirements on mirror quality (e.g., shape and roughness) and alignment scale with the frequency of the radiation. Technology is being pushed further and further and with every new generation of astronomical telescopes, astronomers are able to confirm, tune or reject the existing theories about our understanding of the universe. With new understanding and new ideas come new questions. Questions which often require even more advanced instrumentation to be answered.

For ground based observations in the visible and near/mid infrared, the current developments are towards telescopes with primary mirror (M1) diameters of 30 meters or more. Examples are the Thirty Meter Telescope (TMT) [57] and the European-Extremely Large Telescope (E-ELT) which will be discussed in more detail in Section 1.3.2. These telescopes will deliver an enormous gain in light gathering power (roughly a factor 10) and spatial resolution (roughly a factor 3) in comparison with the currently available state-of-the-art 8 to 10 meter single dish telescopes.

1.1.2 Noise sources in astronomical observations

When performing astronomical observations, the astronomer has to deal with the different noise sources and disturbances which affect the astronomical signal. Depending on the wavelength of the radiation and its origin, the signal from the source can be influenced by the intergalactic, interstellar and interplanetary medium and the atmosphere (if ground based). Especially at IR and submillimeter (submm) wavelengths, the atmosphere not only causes absorption and scattering of the radiation but also generates a very strong background signal as a result of thermal radiation of the medium. This signal is typically much stronger than the signal from the source. Furthermore, density fluctuations (*seeing*) introduce wavefront errors in the signal which, when not accounted for, reduce the spatial resolution in the image. Next to these influences, the signal is polluted by detector and electronic noise as well as thermal radiation from the instrument and environment (through the sidelobes of the diffracted radiation pattern of the telescope when observing at long wavelengths). An extra complication is the temporal variation of these different noise sources.

There are different methods available to handle these observational complications. Current state-of-the-art 8 to 10 meter telescopes like for example the Keck and the VLT use a technique called adaptive optics [38] to reduce the effect of atmospheric seeing. The influence of uncorrelated noise can be reduced by increasing the integration time of the observation. This improves the signal to noise ratio but only with the square root of the integration time. Correlated noise can be partly dealt with by performing a differential measurement, where the measurement of the source is compared to a measurement of only the background. The background signal is collected at a small angular distance (several minutes of arc) from the source. Therefore, the optical path through the atmosphere is considered to be identical in both measurements. Applying this differential measurement technique (referred to as chopping), the background signal can be derived and subtracted from the image which contains the source. The combined on and off measurement has to be performed on time scales shorter then the time scales on which variations in the background signal occur.

1.1.3 The scanning technique

Apart from chopping, altering the line of sight of the telescope is also necessary when observing an extended source (larger than the telescope field of view). In this case the telescope beam has to move over the source in a well defined manner to generate a Nyquist sampled image. Movement of the telescope beam during an observation is generally called scanning.

Different scanning strategies can be considered. In [41] the popular On The Fly (OTF) imaging technique is described for scanning of extended sources. The optimal timing between the on and the off source measurement in an OTF observing scheme for a single pixel heterodyne instrument is discussed in [50]. A comprehensive discussion about the applicability of different scanning strategies is given in [33]. Finally in [19], the effect of different instrument choices, as well as that of different observing techniques, on the efficiency of observations is discussed.

To be able to perform fast scanning observations, without the necessity to rotate the complete telescope or rocking the secondary mirror (M2) [63], a so-called chopper mechanism can be used. This is a relatively small rotatable mirror in the optical path of the scientific instrument behind the telescope, which can quickly be positioned in different orientations thereby changing

the pointing of the complete telescope. This approach is typically used in space applications, of which the chopper mechanism for the Photoconducting Array Camera and Spectrometer (PACS) [34] and the focal plane chopper (FPC) of the Heterodyne Instrument for the Far Infrared (HIFI) described in Section 1.3.1 are examples. However, as the larger size of the optics makes it increasingly difficult to chop using M2, this method becomes more and more relevant for ground based observatories as well.

When a chopping mirror (or M2) is used to perform the task of scanning, an unavoidable side effect is that the position of the beam on M1 is altered during the scanning motion. This can result in another source for fluctuation as thermal radiation from different parts of M1 can vary because of different emissivity or temperatures in different regions of M1. In the case of chopping, this modulation called the offset signal, can be eliminated by the nodding technique [39], or by cooling the M1 mirror to cryogenic temperatures, as is intended for the Space Infrared Telescope for Cosmology and Astrophysics (SPICA) mission [48].

Parallel to the development of more advanced telescopes and instrumentation comes the need for faster and more stable chopper mechanisms. This fact, in combination with the operation of these mechanisms in cryogenic conditions (high vacuum and extremely low temperatures), and the demands on reliability and redundancy, makes it clear that the development of these mechanisms requires full commitment from all fields of mechatronics.

1.2 High performance motion control

From a control perspective, scanning in astronomical applications can be considered to be part of the field of high performance motion control. Here the control objective is to follow a reference trajectory with high precision, where typically the complete path or parts of the trajectory require high speed motions of the mechanism. This is the so called servomechanism problem. A key result in this field is the work by Francis and Wonham [20] on output regulation and the internal model principle, which is discussed separately in Section 2.1.

A related subject is that of point-to-point control. Here the objective is to move from one system state to a new system state in minimal time or with minimal residual vibrations after the step. For both control problems, system constraints (actuator saturation, restrictions on movement, limited amplifier jerk, etc.) have to be accounted for, as well as the issue of robustness of the strategy to plant parameter variations and external disturbances.

Both control problems are of extreme importance for the nanopositioning industry and among others find applications in the field of robotics [3], wafer stage motion control [9] and atomic force microscopy [74]. For our application we are interested in a combination of both strategies, point-to-point control during the step between integration periods and accurate tracking of a reference profile during the observation.

Different control strategies are available in the field of high performance motion control of nanopositioning mechanisms. What these techniques generally have in common is the application of a feedforward (FF) signal for accurate tracking, typically but not necessarily in parallel with a feedback controller for robustness to model uncertainties/variations and disturbances. This is illustrated in Fig. 1.3 where the dotted lines indicate the information channels on which the generation of the FF-signal typically is based.

In [13] it is shown that the inclusion of model based FF (MbFF), instead of feedback control

only, will improve tracking performance even if large plant uncertainties are present in the system model.

The high demand on positioning speed often requires minimization of the inertia of the moving part of the mechanism during the hardware design phase. Lightweighting of the design however can result in shifts of the flexible modes of the mechanism to lower frequencies or the introduction of extra flexible modes. When not properly accounted for, the introduced oscillations can have a disastrous effect on settling time.

Although the design of the FF signal is usually based on the available knowledge of the plant dynamics (model based approach), the details about the generation of the FF signal can vary a lot. In the next sections we briefly discuss different techniques for both the servomechanism and the point-to-point control problem. We do not intend to give a complete overview of the methods available for the two discussed control problems but provide the necessary background and references for further reading.

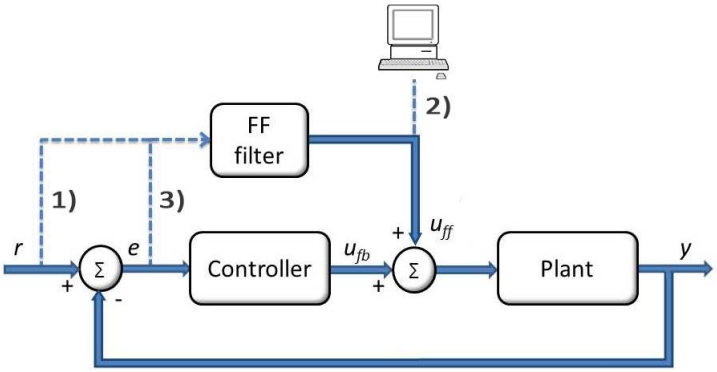

Figure 1.3: Basic high performance motion control block diagram with FF input in parallel with feedback controller. The FF signal can be generated in different ways indicated by the dotted lines. Path 1) uses the reference signal, path 2) determines the FF-signal by offline calculation and path 3) uses the error signal in a feedback loop. For all three approaches the FF filter block has different structure.

1.2.1 Control solutions to the servomechanism problem

Rigid body feedforward

In basic applications, the FF input can be generated accounting only for the inertia of the plant (rigid body/acceleration FF). Based on Newton's second law of motion ($F = ma$), and with the knowledge of the reference trajectory, the required actuator input can be generated. The feedback controller should then provide the corrections needed to compensate for the model mismatch with the real plant dynamics. When extreme tracking accuracy is demanded, this approach is typically inadequate and the flexible modes of the system, together with the suspension of the mass, have to be accounted for. An extension to the rigid body FF is presented in [5] where an inverse model of the dominant flexible mode in the system is included in the form of a skewed notch to increase tracking performance.

Inverse model feedforward

In this case the FF-signal is generated by feeding the reference profile to an inverse of the transfer function of the open loop plant model P_m (path 1 in Fig. 1.3, where the FF filter block is the inverse plant model P_m^{-1}).

Ideally, this would generate the perfect filter for tracking ($rP_m^{-1}P_r = r$), where r is the reference profile and P_r is the transfer function of the real plant. In practice, the perfect plant inverse is often not realizable as the inverse of a strictly proper or non minimum phase plant is respectively non proper and instable. Extra measures are then required for plant inversion, like including a low pass filter to satisfy causality or for example the Zero Phase Error Tracking Control (ZPETC) technique [66] to deal with the instability of the inverse. These changes to the inverse limit the tracking ability of the feedforward generator ($P_m^{-1} \neq P_r^{-1}$). An example of this is given in [67], where the results of stable FF filter design for a non minimum phase system (robot arm), applying both the EBZPETC (based on the ZPETC method) and the added delay method, are compared.

A general limitation, applicable to all model based approaches, is the effect of model uncertainties and unmodeled dynamics of the plant on the accuracy of the plant model. If the model accuracy is limited (with respect to the tracking requirements) the reference profile can be smoothed to limit the amount of energy going into the resonances. The plant constraints can also be accounted for in the design of the reference profile, see for example [36], where the design of a smooth fourth order reference profile, which accounts for plant limitations like maximum jerk, is presented.

Iterative learning control and repetitive control

When a system repeatedly has to follow the same trajectory starting from the same initial conditions, one can also consider the use of iterative learning control (ILC) [7], which was first described in [70] (*text in Japanese*) and [3] . When the reference profile periodically repeats itself, repetitive control [12, 40] can be applied. Early works include [31] and [25]. Different from the model based approach, here the input signal is generated by learning with every repetition (following path 3 in Fig. 1.3 which forms a feedback loop). Both techniques are very similar but in ILC the system evolves on a 2D domain (t, j) with finite time trials t and infinite iterations j, where the initial state of the plant is reset with every iteration j. Whereas for repetitive control, reference signals or disturbances which are periodic are considered, the system evolves on the standard time domain and there is no resetting of the state.

1.2.2 Control solutions for point-to-point control

Two basic approaches can be distinguished in the field of point-to-point control.

- Input shaping: Design an input sequence which results in the requested end position
- Input filtering: Filter an existing input profile to limit residual vibration after the point-to-point movement

For the purpose of input filtering conventional filters can be used which reduce the frequency content of the input signal at specific frequencies (notch filters) or over a certain frequency range (low pass, high, pass, band pass filters). By carefully choosing the location and

the shape of these filters, the effect of the system resonances on the vibration after the step can be reduced.

The input shaping technique [60] explicitly includes the system dynamics in the design of an impulse sequence. This sequence is convolved with the original input signal to produce a new input signal to the plant which effectively reduces residual vibrations. The timing of the impulse sequence is tuned for destructive interference of the resonance modes of the system. The oscillation, introduced by a first impulse to generate motion, is compensated by a second (destructive) impulse after half a period of the considered system resonance. After convolution, the duration of the new input signal is increased as a result of the delayed second input. However, the negative effect this has on settling time is typically less than the limited settling time of the plant with the original input signal, as this will introduce large oscillations directly after the step.

The earliest systematic application of this technique is posicast control described in [62]. Through the years more advanced methods, which are robust to plant uncertainties, were developed. Examples are the Zero Vibration and Derivative (ZVD), the Extra Insensitivity (EI) and the Specified Insensitivity (SI) shapers [71]. However, the increase in robustness of the shaper comes at the cost of increased duration of the shaped input signal and therefore longer settling times.

In typical nanopositioning applications, not only the reduction of residual vibrations but also the time required for performing a step is of crucial importance. A time optimal solution to the point-to-point control problem can be formulated on the basis of Pontryagin's minimum principle. This so called bang bang controller switches between maximum positive and negative actuator inputs to perform the step in minimal time. As the magnitude of the input is clearly defined, the optimization only involves the determination of the moments of switching between both inputs. For a single rigid body, only one switch after exactly half the period of the input is required to perform a step. Higher order systems with damping require more and asymmetrically distributed moments of switching. This aggressive control method is sensitive to model uncertainties and unmodelled dynamics as a small mismatch between the real plant and the model can easily result in unexceptable oscillations after the step. Again, robustness can be added at the cost of time optimality [53].

In [59] the settling performance, with and without model uncertainty, is compared for a number of input filters and input shapers. The difference in performance between the two methods is striking and is clearly in favour of the shaping method. This is supported by the results in [61]. In [58] some background is provided on both input shaping and bang bang type controllers. In [56] three point-to-point control methods are compared on the basis of experimental results.

1.3 Motivation

In this section we introduce the two astronomical instruments which are the motivation for this work. The HIFI chopper mechanism confronted us with the ever increasing challenges during the development of cryogenic space mechanisms. The Metis Cold Chopper (MCC) mechanism, with even more extreme performance requirements, forms a new challenge in this field.

1.3.1 Chopper mechanism for the HIFI instrument on board the Herschel Space Observatory

The Herschel Space Observatory was launched in 2009 on the 14th of May from the European Space Agency (ESA) launch platform in Kourou French Guiana. It has studied the universe during a mission of three and a half years [54]. HIFI is one of three astronomical instruments on board the Herschel Space Observatory. The HIFI instrument is developed by an international consortium led by the SRON Netherlands Institute for Space Research. It performs astronomical observations in seven frequency bands covering the range from 480 to 1250 GHz and from 1410 to 1910 GHz. For a complete description of the instrument and the scientific objectives of the mission, the reader is referred to [24].

The astronomical signal, collected by the main dish of the Herschel telescope, is reflected to the secondary mirror and picked up by the first mirror of the HIFI Focal Plane Unit (FPU). The FPU is situated on the optical bench of the telescope. Figs. 1.4 and 1.5 show a photograph and a schematic drawing of the FPU respectively. The schematic drawing reveals the interior of the FPU. The optics of the instrument are kept at a constant temperature of 15 K, while the scientific detectors in the FPU are cooled to temperatures of 2 K. These low temperatures are required for the operation of the detectors and to avoid degradation of the astronomical signal by thermal radiation from the internal optics of the instrument. The fourth element in the optical train of the FPU (sixth mirror when including the telescope optics) is the HIFI-FPC. In Fig. 1.5 the location of the HIFI-FPC, inside the FPU, is indicated by the red arrow. This steerable mirror can chop the telescope beam between an on-source and an off-source sky position. Next to the chop function, the HIFI-FPC can be used to deflect the HIFI beam to the internal hot and cold load for calibration of the instrument.

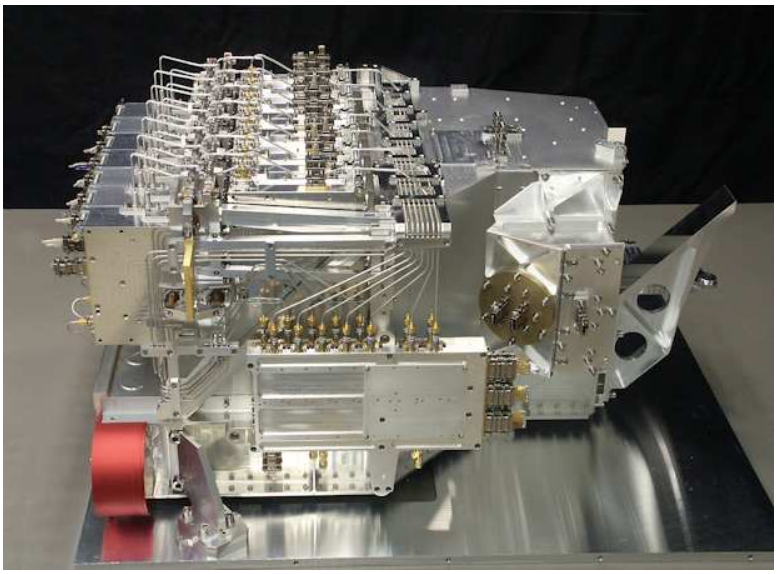

Figure 1.4: Photograph of the HIFI-FPU flight model after completion of the assembly (courtesy of Hans Braun). The red structure serves as protection for the optics. This so called red tag item was removed after integration of the FPU with the Herschel telescope.

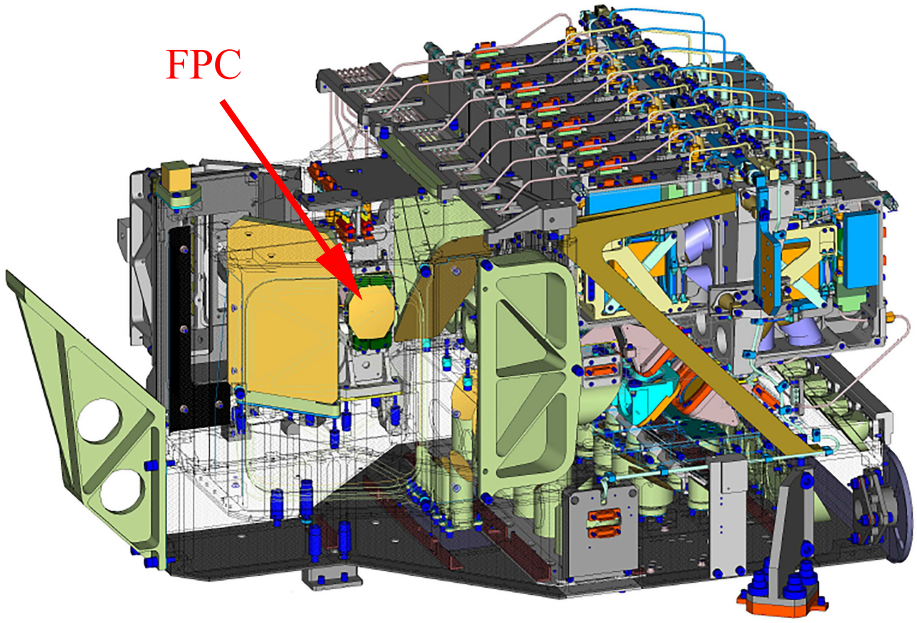

Figure 1.5: Schematic drawing of the interior of the HIFI-FPU (courtesy of Mecon). The location of the HIFI-FPC is indicated with the red arrow.

The HIFI-FPC has been identified as one of the critical elements in the FPU of the HIFI instrument. It is a potential single point of failure in the instrument which requires high reliability and redundancy in the design of the mechanism.

During the development of the HIFI-FPC we were confronted with different mechatronic issues related to the complexity of the instrument, the high performance requirements and the harsh operational environment. An important conclusion of this project is the need for advanced control strategies and an integrated design approach to be able to meet the ever increasing requirements for these kind of mechanisms in future missions. These issues are discussed in more detail in Chapter 4.

The HIFI-FPC has been developed by SRON Netherlands Institute for Space Research, an organization that has ample experience in building space qualified mechanisms since the 1980s. One of the examples, relevant to the development of the HIFI-FPC, is the grating drive mechanism for the ISO SWS instrument [1, 73].

1.3.2 2D chopper mechanism for the METIS instrument of the European-Extremely Large Telescope

The control strategy, described later in Chapter 3, is being developed for application in the MCC [52]. It is one of the critical components in the Mid-Infrared E-ELT Imager and Spectrograph (METIS) [6]. Details about the opto-mechanical design of METIS, and the location of the MCC in the instrument can be found in [35]. METIS will be one of the first three scientific instruments on the E-ELT [16], covering the thermal infrared wavelength range. An artist's impression of the E-ELT is given in Fig. 1.6. With its 39m dish, the E-ELT will be the largest optical/infrared telescope ever. The E-ELT will see first light in 2024 and is being developed by the European Southern Observatory (ESO).

Figure 1.6: Artist's impression of the E-ELT on Cerro Armazones. Showing the 39 meter segmented primary mirror. Source: ESO/L. Calçada. [Online] Available from: http://www.eso.org/public/netherlands/images/eso1440e/ [Accessed 1^{st} September 2015]

While the discussed beam chopping is traditionally done by the telescope's secondary mirror, because of the large dimensions of this mirror this option does not exist for the E-ELT and an alternative solution within METIS had to be found.

The MCC is a tip/tilt mirror at the pupil position of METIS. Tilting the MCC in two dimensions moves the orientation of the telescope beam on the sky without having to move the telescope.

Several challenging performance requirements drive the design of both hardware and control of the MCC (see Table 1.1). Most notably are the requirements for short beam switching times (i.e., high observing efficiency with small overheads, which requires short settling times) and very accurate positional repeatability (which is required for sharp images in co-added, long term exposures). Meeting these requirements simultaneously is very challenging from a control perspective, which is related to the field of high performance motion control.

Table 1.1: MCC requirements. Positional stability is defined as $3\times$ rms $(i.e., \sigma)$ level, all other requirements are defined as absolute maximum. NB: 1.7 μrad corresponds to a mirror displacement at the sensor location of 36 nm.

Description	Requirement	Unit	Remark
Pos. stability	$\leqslant 1.7$	[μrad]	3σ
Pos. repeatability	$\leqslant 1.7$	[μrad]	1.7 μrad = 36 nm at sensor position
Pos. accuracy	$\leqslant 85$	[μrad]	
Settling time	$\leqslant 5$	[msec]	settling within 1.7 μrad of end pos.
Parasitic z-disp.	$\leqslant 200$	[μm]	
Power dissipation	< 1	[W]	for 5 Hz chop
Peak currents	$\leqslant 10$	[A]	over 8.5 mrad
Thermal stability	$\leqslant 1.7$	[μrad]	
Lifetime	$> 10^8$	[cycles]	

To be able to study the feasibility of the required MCC mechanism at an early stage during the METIS development, the METIS Cold Chopper Demonstrator (MCCD) project was initiated (see also Appendix D). The MCCD, and the application of the developed control strategy to this mechanism, is later described in Chapter 6.

1.4 Aim

The research presented in this thesis is strongly related to the MCCD project. The goals of the MCCD project are described in Appendix D. Based on these goals, the following scientific objectives can be formulated:

- Develop an advanced control strategy for the MCCD, which can meet the stringent performance requirements defined for this mechanism
- Verify the applicability of the strategy in a representative cryogenic experimental setup
- Compare the method to existing strategies applicable to the field of high performance motion control

1.5 Contributions

In Chapter 3 we describe a hybrid control synthesis for achieving output regulation in a mechatronic system which has the following requirements: very-fast stepping between different scanning profiles and asymptotic tracking of the scanning profile while satisfying various system

state constraints and performance and stability robustness. Such requirements are highly relevant to chopper mechanisms for astronomical observations and to other advanced instrumentations/machines with nanopositioning mechanisms. We provide necessary and sufficient conditions to solve the chopper scanning control problem by applying recent results on hybrid output regulation [42] and we prove practical stability of the hybrid system for non optimal feedforward signals. We describe hybrid control synthesis with the HIFI-FPC mechanism in Chapter 5 and show an improvement in settling time of 37% by applying this new control strategy.

In Chapter 4 we provide design rules applied to the HIFI-FPC, which are generally applicable to the development of cryogenic mechanisms and are used in the development of the MCCD.

In Chapter 6 we describe the design, system identification, control synthesis and performance of the MCCD. The development of the MCCD mechanism is a joint effort of all members of the MCCD project team (see Appendix D for MCCD project description). During the design phase we contributed to various design choices (e.g., sensor choice, required actuator force, allowed mechanical tolerances) by analysis and simulation. Based on a detailed system identification of the final MCCD hardware we have revealed the presence of hysteresis in the actuators and modelled this effect to gain valuable insight in the characteristics of the mechanism. After synthesis of the hybrid controller as well as of a repetitive controller we have determined all performance aspects of the mechanism and have realized performance which is very close to the stringent requirements defined for the mechanism. To be able to meet the stringent performance requirements of the mechanism during operation in the METIS instrument, we have provided the MCCD team with recommendations on the realization of the final MCC mechanism.

1.6 Thesis outline

The outline of the thesis is as follows. Chapter 2 provides the preliminaries on output regulation, hybrid systems, hybrid output regulation and the repetitive control strategy. In Chapter 3 the hybrid control strategy for high performance motion control of chopper mechanisms is formulated and necessary and sufficient conditions for hybrid output regulation are presented. Chapter 4 describes the cryogenic mechatronic design of the HIFI-FPC. General design considerations for the development of mechanisms that have to operate at cryogenic conditions are discussed and the performance of the HIFI-FPC, applying the original controller, is presented. In Chapter 5 the hybrid control strategy is applied to the HIFI-FPC and the results are compared to the results applying the original controller. Chapter 6 describes the system identification and control synthesis of the hybrid controller and of a repetitive controller with the MCCD. The performance of the MCCD is defined based on an extensive test program of the hardware and recommendations for the final MCC mechanism are provided. Finally, in Chapter 7 the conclusions and recommendations for future research are given.

1.7 List of publications

Journal papers

- R. Huisman, J.W.G. Aalders, M.J. Eggens, J. Evers, H.M. Jacobs, B.J. Van Leeuwen, A.C.T. Nieuwenhuizen, G.R. Ploeger, K.J. Wildeman, B. Jayawardhana and J.M.A. Scherpen. Cryogenic mechatronic design of the HIFI Focal Plane Chopper. Mechatronics 21(8): 1259-1271, 2011.
- R. Huisman, J. Boomer and B. Jayawardhana. Hybrid control synthesis for output regulation with applications to fast motion nano-positioning mechanisms. 2015, under review.
- R. Huisman, S. Paalvast, B. Brandl, T.C. van den Dool, M. Eggens, H. Janssen, G. Aitink-Kroes, F. Molster, M. Teuwen, L. Venema and B. Jayawardhana. High performance motion control of the METIS Cold Chopper Mechanism. 2015, accepted with minor revisions.

Conference papers

- R. Huisman and B. Jayawardhana. On the design of hybrid output regulation for the METIS cold chopper. In Proceedings of the 7th IFAC Symposium on Robust Control Design, Aalborg, 2012.
- S.L. Paalvast, H. Janssen, M. Teuwen, R. Huisman, B. Brandl, F. Molster and L. Venema. Development of a 2D precision cryogenic chopper for METIS. In Proceedings of SPIE, 8450: 845020-845021, 2012.
- S.L. Paalvast, R. Huisman, B. Brandl, H. Janssen, B. Jayawardhana F. Molster, M. Teuwen and L. Venema. Development and characterization of a 2D precision cryogenic chopper for METIS. In SPIE Astronomical Telescopes & Instrumentation, pages 91510D-91510D, International Society for Optics and Photonics, 2014.
- G. Kroes, R. Ter Horst, J. Kragt, R. Roelfsema, R. Navarro, L. Venema, R. Lenzen, R.R. Rohloff, G. Durand, E. Pantin, S. Rayonett et al. METIS opto-mechanical design and packaging study. In: SPIE Astronomical Telescopes & Instrumentation. International Society for Optics and Photonics, p. 77352J-77352J-12. 2010.

Conference abstracts

- R. Huisman and B. Jayawardhana. Tracking periodic signals for simple hysteretic mechanical systems using repetitive internal model. Benelux meeting on systems and control. Heeze, The Netherlands, 2010.
- R. Huisman and B. Jayawardhana. Hybrid Robust Output Regulation for the METIS Chopper. Heijden, The Netherlands, 2012.
- R .Huisman, J. Boomer, B. Jayawardhana and J.M.A. Scherpen. Hybrid control synthesis for output regulation: application to the HIFI focal plane chopper. Houffalize, Belgium, 2013.
- R .Huisman, B. Jayawardhana and J.M.A. Scherpen. Hybrid controller design and verification for the METIS Cold Chopper Mechanism. Heijden, The Netherlands, 2014.

MCCD Project documentation

- H. Janssen, M. Teuwen, R. Huisman and S. Paalvast. Test specification MCCD. MCCD project documentation, Doc: TS_MCCD_02, 2011.
- R. Huisman and B. Jayawardhana. Design verification based on control analysis MCCD. MCCD project documentation, Doc: DV_MCCD_01, 2011.
- R. Huisman. Performance test report METIS Cold Chopper Demonstrator. MCCD project documentation, Doc: TR_MCCD_PT01, 2014.

Popular papers

- R. Huisman. Gecontroleerde precisie op anderhalf miljoen kilometer van de aarde. Mechatronica magazine nr.8, 2011.

Co-authored papers related to the HIFI project

- C. Dedes, M. Röllig, B. Mookerjea, Y. Okada, V. Ossenkopf, S. Bruderer, A.O. Benz, M. Melchior, C. Kramer, M. Gerin et al. The origin of the [C II] emission in the S140 PDRs-new insights from HIFI. arXiv preprint arXiv:1007.4957. 2010.
- Th. de Graauw, F.P. Helmich, T.G. Phillips, J. Stutzki, E. Caux, N.D. Whyborn, P. Dieleman, P.R. Roelfsema, H. Aarts, R. Assendorp et al. The Herschel-Heterodyne Instrument for the Far-Infrared (HIFI). Astronomy & Astrophysics 518: L6, 2010.
- W. Jellema, R. Huisman, M. Candotti, T. Finn, N. Trappe, J.A. Murphy, W. Stafford and W. Wild. Comparison of near-field measurements and electromagnetic simulations of the focal plane unit of the Heterodyne Instrument for the Far-Infrared. In 5th International Conference on Space Optics, Vol. 554, pp. 303-322, 2004.
- M. Mueller, W. Jellema, B. Delforge, D. Teyssier, M. Eggens, R. Huisman and G. Keizer. In-Flight calibration of the HIFI Diplexers. In : Experimental Astronomy. 37, 2, p. 369-379, 2014.
- P.R. Roelfsema, F.P. Helmich, D. Teyssier, V. Ossenkopf, P. Morris, M. Olberg, R. Shipman, C. Risacher, M. Akyilmaz, R. Assendorp et al. In-orbit performance of Herschel-HIFI. Astronomy & Astrophysics, 537, 2012: A17.
- T.A. Van Kempen, L.E. Kristensen, G.J. Herczeg, R. Visser, E.F. Van Dishoeck, S.F. Wampfler, S. Bruderer, A.O. Benz, S.D. Doty, C. Brinch et al. Origin of the hot gas in low-mass protostars-Herschel-PACS spectroscopy of HH 46. Astronomy & Astrophysics, 518, L121, 2010.

Chapter 2

Preliminaries on control theory

This chapter provides the theoretical background which is required for the formal definition of the hybrid control strategy and the proof of output regulation in Chapter 3. It also describes the repetitive control method which is applied to the MCCD as an alternative to the hybrid control method in Chapter 6.

A pivotal result in the field of reference tracking is the work of Francis and Wonham [20] on output regulation and the internal model principle, which is discussed in Section 2.1. Section 2.2 defines the structure of a general hybrid system and gives necessary and sufficient conditions for output regulation of hybrid systems. These results are based on [23] and [42]. Finally, Section 2.3 provides some background on the repetitive control strategy.

2.1 Classical output regulation for linear systems

In the following, we consider a SISO LTI plant defined by

$$\left.\begin{aligned} \dot{x} &= A_G x + B_G u + P w, \quad x(t_0) = x_0, \\ y &= C_G x, \end{aligned}\right\} \tag{2.1}$$

where $x \in \mathbb{R}^n$ is the state vector, $u \in \mathbb{R}$ is the input, $y \in \mathbb{R}$ is the output, A_G is the state matrix, B_G is the input matrix and C_G is the output matrix of the plant. The state $w \in \mathbb{R}^s$ is the state of the so called exosystem that can generate reference and/or disturbance signals and is given by

$$\left.\begin{aligned} \dot{w} &= S w, \quad w(t_0) = w_0, \\ r &= Q w, \end{aligned}\right\} \tag{2.2}$$

where Q and S are real constant matrices with appropriate dimensions. Disturbances are introduced to the plant by the mapping of w through the disturbance input matrix P. The matrices A_G, B_G, C_G and P are real constant matrices with appropriate dimensions.

Based on these system descriptions, the tracking error of the plant w.r.t. the reference signal r, can be defined as

$$e = Q w - C_G x, \tag{2.3}$$

where $e \in \mathbb{R}$.

To be able to guarantee robust stability of the plant and to optimize performance, we introduce a dynamic feedback controller, which processes the tracking error e and generates the input u to the plant. This controller has the following form

$$\left.\begin{aligned} \dot{x}_c &= A_C x_c + B_C e, \quad x_c(t_0) = x_{c0}, \\ u &= C_C x_c, \end{aligned}\right\} \tag{2.4}$$

where $x_c \in \mathbb{R}^m$ and A_C, B_C and C_C are real constant matrices with appropriate dimensions.

Based on these definitions the dynamics of the complete closed loop system can now compactly be formulated as

$$\begin{aligned} \dot{w} &= Sw, \\ \begin{bmatrix} \dot{x} \\ \dot{x}_c \end{bmatrix} &= \begin{bmatrix} A_G & B_G C_C \\ -B_C C_G & A_C \end{bmatrix} \begin{bmatrix} x \\ x_c \end{bmatrix} + \begin{bmatrix} P \\ B_C Q \end{bmatrix} w, \\ y &= \begin{bmatrix} C_G & 0 \end{bmatrix} \begin{bmatrix} x \\ x_c \end{bmatrix}. \end{aligned} \tag{2.5}$$

For the closed loop system defined in (2.5) we are interested in defining sufficient and necessary conditions for stability and asymptotic reference tracking. This problem is called the problem of output regulation and can be formulated as follows

Output regulation problem: Given $\{A_G, B_G, C_G, P, Q, S\}$, find controller matrices $\{A_C, B_C, C_C\}$ such that:
1) The closed loop system (2.5) is stable
2) For any initial condition $\begin{bmatrix} x_0 \\ x_{c0} \end{bmatrix}$ and w_0, $\lim_{t\to\infty} e(t) = 0$

Without loss of generality, we can consider $\sigma(S) \in \bar{\mathbb{C}}^+$, as $\sigma(S) \in \mathbb{C}^-$ would make the exosystem stable and reduce the problem to that of internal stability (if we satisfy 1) then 2) is automatically satisfied).

To solve the problem of output regulation we first give a definition of an invariant manifold of a dynamical system.

Invariant manifold: A manifold $\mathcal{M}$ is said to be forward and backward invariant for the dynamics described in (2.1) if the following implication holds:

$$x(0) \in \mathcal{M} \Leftrightarrow x(t) \in \mathcal{M} \quad \forall t \in \mathbb{R}_+.$$

Now if we are able to stabilize the system by a suitable choice of $\{A_C, B_C, C_C\}$, the invariant manifold, which defines the steady state response of the closed loop system to r, can be formulated as

$$\mathcal{M} = \left\{ (x, x_c, w) \in \mathbb{R}^n \times \mathbb{R}^m \times \mathbb{R}^s : \begin{bmatrix} x \\ x_c \end{bmatrix} = \begin{bmatrix} \Pi_x \\ \Pi_c \end{bmatrix} w \right\}.$$

Substituting this in (2.5) gives us the following regulator equation

$$\begin{bmatrix} \Pi_x \\ \Pi_c \end{bmatrix} S = \underbrace{\begin{bmatrix} A_G & B_G C_C \\ -B_C C_G & A_C \end{bmatrix}}_{A_{cl}} \begin{bmatrix} \Pi_x \\ \Pi_c \end{bmatrix} + \begin{bmatrix} P \\ B_C Q \end{bmatrix}, \tag{2.6}$$

which forms a Sylvester equation. Equation (2.6) has a unique solution Π if and only if $\sigma(A_{cl}) \neq \sigma(S)$. This condition is satisfied by our definition of the exosystem and the assumption of closed loop stability.

If this solution also satisfies

$$0 = Q - C_G\Pi_x.$$

then we have output regulation.

Theorem 2.1.1 [20] *Let (A_G, B_G) be stabilizable and let (A_G, C_G) be detectable. The controller* (2.4) *solves the problem of output regulation if and only if there exist $\Pi_x \in \mathbb{R}^{n\times s}$ and $\Pi_c \in \mathbb{R}^{m\times s}$ such that*

$$\begin{aligned} \Pi_x S &= A_G\Pi_x + B_G C_C \Pi_c + P, \\ \Pi_c S &= -B_C C_G \Pi_x + A_C \Pi_c + B_C Q, \\ 0 &= Q - C_G \Pi_x, \end{aligned} \tag{2.7}$$

Internal model principle: The internal model principle states that the problem of output regulation can be solved, if and only if $\sigma(S) \subset \sigma(A_C)$. If this is satisfied, we say that the controller incorporates a duplicate (an internal model) of the exosystem dynamics which generates the reference signal. This internal model has to be observable from the plant input u and controllable from the error signal e.

2.2 Output regulation for hybrid systems

2.2.1 Hybrid systems

We utilize the hybrid formalism and notation as given in [23]. A hybrid system is a system which exhibits both continues time and discrete time dynamics denoted respectively as flow and jump dynamics. An example is a billiard ball bouncing from wall to wall on a billiard table. In this case, the flow dynamics satisfy Newtons laws (ignoring friction etc.) and define the trajectory of the ball in between collisions with the walls. In a collision, the abrupt change in velocity can be described by a jump in the state of the system. The different dynamics are typically applicable to certain subspaces of the state space defined by the characteristics of the system.

More precisely, an autonomous hybrid linear system can be defined as

$$\left.\begin{aligned} \dot{x} &= A_G x,\ x \in C \\ x^+ &= M_G x,\ x \in D, \end{aligned}\right\} \tag{2.8}$$

where $x \in \mathbb{R}^n$ is again the state vector and x^+ denotes the state after the jump transition has occurred. The flow map $x \mapsto A_G x$ describes the flow dynamics on the flow set $C \subset \mathbb{R}^n$ and the jump map $x \mapsto M_G x$ defines the jump dynamics from the jump set $D \subset \mathbb{R}^n$.

Solutions of the hybrid system are parametrized by a hybrid time domain E. A subset E of $\mathbb{R}_{\geqslant 0} \times \mathbb{N}$ is a hybrid time domain if it is the union of infinitely many intervals of the form $[t_j, t_{j+1}] \times \{j\}$, where $0 = t_0 \leqslant t_1 \leqslant t_2 \leqslant \ldots$, or of finitely many such intervals, with the last one possibly of the form $[t_j, t_{j+1}] \times \{j\}$, $[t_j, t_{j+1}) \times \{j\}$, or $[t_j, \infty) \times \{j\}$. A solution of (2.8) on E is called a hybrid arc. For details on the solution of (2.8), we refer to [23].

When an external input is applied, following the definition of [49], the non autonomous hybrid linear system can be defined as

$$\left.\begin{aligned} \dot{x} &= A_G x + B_G u,\ (x,u) \in C \\ x^+ &= M_G x + N_G u,\ (x,u) \in D, \end{aligned}\right\} \tag{2.9}$$

where it is assumed implicitly that x and u share the same hybrid time domain. For details on the solution of (2.9), we refer again to [49].

2.2.2 Hybrid output regulation

Based on the definitions in Section 2.1 and 2.2.1 we are now able to formulate necessary and sufficient conditions for hybrid output regulation as presented in [42]. We follow the same plant description as in Section 2.1.

Consider the hybrid plant with flow and jump dynamics described by

$$\left.\begin{array}{ll} \dot{\tau}_c = 1 & \\ \dot{\zeta} = A_G\zeta + B_G u + Pw,\ \zeta(0,0) = \zeta_0 & \forall(\tau_c,\zeta,u) \in [0,\tau_{max}] \times \mathbb{R}^n \times \mathbb{R} \\ & \\ \tau_c^+ = 0 & \\ \zeta^+ = M_G\zeta + N_G w & \forall(\tau_c,\zeta) \in \tau_{max} \times \mathbb{R}^n \\ y = C_G\zeta, & \end{array}\right\} \tag{2.10}$$

where τ_c is a clock variable with a dwell time τ_{max} which defines the moment of jumping of the system.

The reference signal can be defined by the following hybrid exosystem

$$\left.\begin{array}{lll} \dot{\tau}_c &= 1 & \\ \dot{w} &= Sw,\ \ w(0,0) = w_0 & \forall(\tau_c,w) \in \mathcal{W} \\ & & \\ \tau_c^+ &= 0 & \\ w^+ &= Jw & \forall(\tau_c,w) \in \mathcal{W} \cap (\{\tau_{max}\} \times \mathbb{R}^s) \\ r &= Qw, & \end{array}\right\} \tag{2.11}$$

where $\mathcal{W} := \{(\tau_c, w) : \tau_c \in [0, t_{obs}], w \in W(\tau_c)\}$, and the set valued mapping $\tau_c \mapsto W(\tau_c) \subset \mathbb{R}^s$ which is continuous with compact values, defines the domain of exosystem states during flow.

The regulation error during the flow is given by $e = Qw - C_G x$ and changes as $e^+ = (CN + QJ)w + CMx$ with every jump of the system.

Instead of the dynamic controller of (2.4) we now consider a hybrid controller of the form

$$\left.\begin{array}{lll} \dot{\tau}_c &= 1 & \\ \dot{\xi} &= A_C\xi + B_C e,\ \xi(0,0) = \xi_0 & \forall(\tau_c,\xi,e) \in [0,\tau_{max}] \times \mathbb{R}^m \times \mathbb{R} \\ \tau_c^+ &= 0 & \\ \xi^+ &= \Phi\xi + \Psi e & \forall(\tau_c,\xi,e) \in \{\tau_{max}\} \times \mathbb{R}^m \times \mathbb{R} \\ u &= C_C\xi + D_C e & \end{array}\right\}. \tag{2.12}$$

The closed loop hybrid system can then compactly be formulated as follows

$$\left.\begin{array}{lll} \dot{\tau}_c &= 1, \quad \dot{w} = Sw, \quad w(0,0) = w_0 & \\ \begin{bmatrix}\dot{\zeta}\\ \dot{\xi}\end{bmatrix} &= \mathcal{H}_{cl}\begin{bmatrix}\zeta\\ \xi\end{bmatrix} + \mathcal{L}_{cl}w,\ \begin{bmatrix}\zeta(0,0)\\ \xi(0,0)\end{bmatrix} = \begin{bmatrix}\zeta_0\\ \xi_0\end{bmatrix} & \forall((\tau_c,w),\zeta,\xi) \in \mathcal{W} \times \mathbb{R}^n \times \mathbb{R}^m \\ & & \\ \tau_c^+ &= 0, \quad w^+ = Jw & \\ \begin{bmatrix}\zeta^+\\ \xi^+\end{bmatrix} &= \mathcal{J}_{cl}\begin{bmatrix}\zeta\\ \xi\end{bmatrix} + \mathcal{M}_{cl}w & \forall((\tau_c,w),\zeta,\xi) \in (\mathcal{W} \cap (\{\tau_{max}\} \times \mathbb{R}^s)) \times \mathbb{R}^n \times \mathbb{R}^m \end{array}\right\} \tag{2.13}$$

with

$$\mathcal{H}_{cl} := \begin{bmatrix} A_G - B_G D_C C_G & B_G C_C \\ -B_C C_G & A_C \end{bmatrix} \mathcal{L}_{cl} := \begin{bmatrix} B_G D_C Q \\ B_C Q \end{bmatrix}$$
$$\mathcal{J}_{cl} := \begin{bmatrix} M_G & 0 \\ -\Psi C_G & \Phi \end{bmatrix} \mathcal{M}_{cl} := \begin{bmatrix} N_G \\ \Psi Q \end{bmatrix}$$

The standard problem of hybrid output regulation, as studied in [42], can be defined as follows

Hybrid output regulation problem: Given the plant (2.10) and exosystem (2.11) find a controller (2.12) such that:

1) The hybrid closed loop system (2.13) is stable

2) For any initial condition $\begin{bmatrix} \zeta_0 \\ \xi_0 \end{bmatrix}$ and w_0, $\lim_{t+j\to\infty} e(t,j) = 0$

Again we are interested in defining an invariant set of the form

$$\mathcal{M} = \left\{ ((\tau, w), \zeta, \xi) \in \mathcal{W} \times \mathbb{R}^n \times \mathbb{R}^m : \begin{bmatrix} \zeta \\ \xi \end{bmatrix} = \begin{bmatrix} \Pi_x \\ \Pi_c \end{bmatrix} w \right\}$$

for which hybrid output regulation is solvable.

Let ϕ_{cl} be the state transition matrix of the flow dynamics

$$\begin{bmatrix} \dot{\zeta} \\ \dot{\xi} \end{bmatrix} = \mathcal{H}_{cl} \begin{bmatrix} \zeta \\ \xi \end{bmatrix}.$$

In other words $\phi_{cl}(\tau_{max}) = \exp(\mathcal{H}_{cl}\tau_{max})$ and $\phi_{cl}(t_0) = I_{n+m}$.

To be able to define the conditions for hybrid output regulation, we first define necessary and sufficient conditions for the existence and uniqueness of a steady state of the hybrid system.

Theorem 2.2.1 [42] *There exists a unique steady state of the hybrid closed loop plant* (2.13) *if and only if the following two conditions hold*

A1) *Non-resonance condition: The eigenvalues of* $\mathcal{J}_{cl}\phi_{cl}(\tau_{max})$ *and of* $J \exp(S\tau_{max})$ *are disjoint.*

A2) *Internal stability condition: The eigenvalues of the matrix* $\mathcal{J}_{cl}\phi_{cl}(\tau_{max})$ *lie within the unitary disk.*

The following technical lemma is due to [42] on the solvability of output regulation for hybrid systems that is related to the solvability of a hybrid regulator equation.

Theorem 2.2.2 [42] *Suppose that the hybrid controller* (2.12) *is such that the closed-loop system* (2.13) *satisfies* **(A1)** *and* **(A2)**. *Then there exist a unique solution* Π *to the following equations*

$$\begin{aligned} 0 &= \mathcal{H}_{cl}\Pi - \Pi S + \mathcal{L}_{cl} \\ 0 &= \mathcal{J}_{cl}\Pi - \Pi J + \mathcal{M}_{cl} \end{aligned} \tag{2.14}$$

Assume, additionally, that the set $\mathcal{W}$ *is forward and backward invariant for the hybrid system described by* (2.11). *Then the hybrid controller* (2.12) *solves the problem of output regulation if and only if the following equation is satisfied*

$$Q - C_G \Pi_x = 0 \tag{2.15}$$

where Π_x *is the matrix obtained by extracting the first* n *rows from* Π.

2.3 Repetitive control strategy

As for the considered application we are interested in periodic reference tracking, we focus on the repetitive method here. For details about ILC the reader is referred to the discussion in Section 1.2.1.

Fig. 2.1 shows the general repetitive control layout. The repetitive loop is placed in parallel with a feedback controller. It consists of a so called L-filter for phase compensation, a Q-filter to add robustness and a delay line. The lead term z^{γ} in the delay line can be used to partly compensate for the phase lag in the loop as described in [40]. The gain k_r was added as an extra degree of freedom for tuning of the loop.

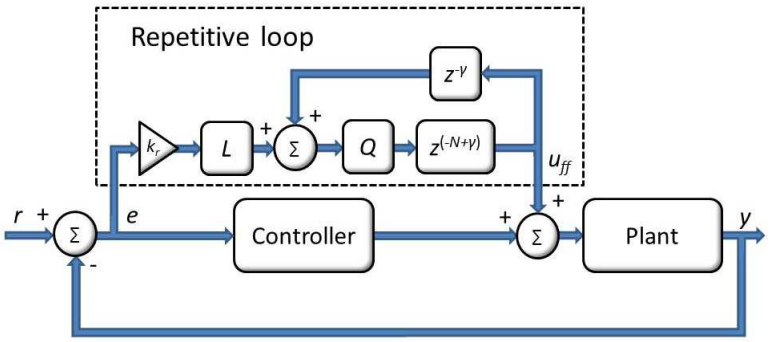

Figure 2.1: Repetitive control layout. The repetitive loop is placed in parallel with the standard feedback controller. N is the number of discrete samples in one repetition. The phase lead γ and the gain k_r are used to tune the performance of the repetitive controller.

The delay line can generate any periodic signal with period N, it adds an internal model to the feedback controller which allows for zero error tracking of any repetitive reference signal with period N.

This can be understood if we examine the transfer function of the delay line. Setting $\gamma = 0$, the transfer function can easily be computed to be $\frac{1}{z^N-1}$ which has the bode magnitude plot given in Fig. 2.2. Essentially the delay line adds high gain to the controller at all harmonic frequencies of the fundamental frequency $1/(N.\Delta t)$ of the periodic reference (or periodic disturbance), which allows for good tracking (and periodic disturbance attenuation).

The learning update law of the repetitive loop can be formulated as follows:

$$z^N U_{ff}(z) = Q(U_{ff}(z) + z^{\gamma} L k_r E(z)), \tag{2.16}$$

where $z^N U_{ff}(z) = U_{ff}(z+N)$ is the new input which will be applied during the next repetition and is constructed from the input of the current repetition $U_{ff}(z)$ and from the error $E(z+\gamma)$ as a result of this input.

From the feedback loop we have

$$E(z) = -S_p U_{ff}(z), \tag{2.17}$$

where $S_p = P/(1 + PC)$ is the plant sensitivity function. Combining (2.16) and (2.17) gives us

$$E(z + N) = Q(1 - z^{\gamma} S_p k_r L)E(z),$$

which can be interpreted as the error propagation with every repetition.

For stability we need

$$|Q(1 - z^{\gamma} S_p k_r L)| < 1$$

Taking $L = {S_p}^{-1}$, $\gamma = 0$ and $k_r = 1$ theoretically delivers perfect tracking after only one iteration (dead-beat solution). However, for the same reasons as mentioned in Section 1.2.1 an exact inverse is typically not realizable. Different techniques, such as ZPETC [66], are available for the design of L. The Q-filter can be designed as a low pass filter to guarantee stability of the system, but this comes at the cost of reduced tracking performance.

This technique is less sensitive to the accuracy of the system model and is therefore more robust to unmodelled dynamics and plant uncertainties. The technique is known to amplify the influence of random noise and disturbances [45] which is critical for the considered application. The reproducibility of the plant is generally considered to be a measure for the tracking accuracy that can be attained by repetitive control.

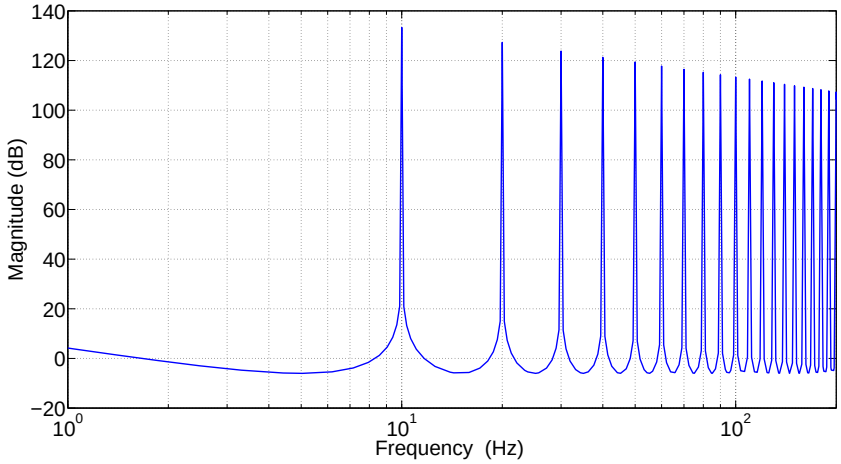

Figure 2.2: Bodemagnitude plot of the delay line implemented in the repetitive loop. The peaks at the harmonic frequencies of the repetition period allow for good tracking of the periodic reference signal (or good rejection of periodic disturbances).

Chapter 3

Hybrid control strategy for output regulation in high performance applications

In this chapter we define a controller that can satisfy output regulation and is able to meet the stringent requirements on settling time and positional stability which are generally demanded for nanopositioning mechanisms. The proposed controller can deal with input constraints and is robust to the negative effects of noise sources and disturbances.

Using recent progress in hybrid control theory [42, 23] and by reformulating our closed-loop system into a hybrid system, we can show rigorously that output regulation is achieved, i.e., asymptotic tracking during the flow dynamics is guaranteed for a wide range of periodic reference trajectories. In particular, we provide necessary and sufficient conditions on the jump map and the flow dynamics for asymptotic stability.

In Section 3.1, we formulate the scanning problem that is relevant for our astronomical application and is the basis for our subsequent controller development. A general outline of the control strategy is given in Section 3.2. In Section 3.3, we discuss the reformulation of the scanning problem into the hybrid control framework and we formulate the hybrid control strategy. In Section 3.4 we define necessary and sufficient conditions for hybrid output regulation and discuss practical stability of the system. The design of the FF signal is discussed in Section 3.5. Finally, we will discuss the relation of our method to other relevant control strategies in Section 3.6.

The results in this chapter are published in [30] and [27].

3.1 Chopper scanning problem formulation

We consider a linear 2 degrees of freedom (DoF) n^{th} order system, with constraints on the input u, as our general chopper mechanism. We limit our system description to 2 DoF's as this is appropriate for the application considered (MCCD). Assuming decoupled DoF's, extension to higher dimensions is however trivial. The plant dynamics for such a system can compactly be written by

$$\left.\begin{aligned} \dot{x} &= A_G x + B_G u, \quad x(t_0) = x_0 \quad \forall (x,u) \in \mathbb{R}^{2n} \times \mathbb{R}^2, \\ y &= C_G x, \end{aligned}\right\} \tag{3.1}$$

with

$$A_G = \begin{bmatrix} A_{G_1} & 0 \\ 0 & A_{G_2} \end{bmatrix} \; B_G = \begin{bmatrix} B_{G_1} & 0 \\ 0 & B_{G_2} \end{bmatrix} \; C_G = \begin{bmatrix} C_{G_1} & 0 \\ 0 & C_{G_2} \end{bmatrix},$$

where A_{G_i}, B_{G_i} and C_{G_i} are the state space matrices for the i^{th} DoF that are given in canonical form as follows

$$A_{G_i} = \begin{bmatrix} 0 & 1 & 0 & \dots & 0 \\ \vdots & 0 & 1 & \dots & 0 \\ \vdots & \vdots & \ddots & \ddots & \vdots \\ a_{in-1} & a_{in-2} & \dots & \dots & a_{i0} \end{bmatrix}$$

$$B_{G_i} = \begin{bmatrix} 0_{(1\times n-1)} & b_n \end{bmatrix}^T \quad C_{G_i} = \begin{bmatrix} 1 & 0_{(1\times n-1)} \end{bmatrix}.$$

For standard chopper mechanisms, the input u represents typically the current or voltage input signal to the actuator and the output y is the measured displacement. Although additional measurement for feedback control can be considered, we do not consider such information in our present work.

Prior to defining formally the chopper scanning control problem, we need to introduce the following few definitions related to the desired scanning reference profile.

Reference flows: The set of smooth functions $\mathcal{R}_p : [0, \tau_p] \to \mathbb{R}^2$, $p = 1, \dots, q$, are called the *reference flows*. These reference flows represent the set of desired displacement trajectories of the chopper (which can be constant) during the different integration periods $[t_k, t_k + \tau_p]$ that constitute an astronomical observation, where t_k denotes the starting time of the k^{th} integration period.

Flow selection: The mapping $\mathcal{S} : \mathbb{Z}_+ \to \{1, 2, \dots, q\}$ is called the *flow selection*. It defines the reference flow $p \in \{1, 2, \dots, q\}$ for every integration period $k \in \mathbb{Z}_+$.

Scanning reference profile: Using $\mathcal{R}_p$ and $\mathcal{S}$, and by denoting

$$t_k := \sum_{j=0}^{k-1} \tau_{\mathcal{S}(j)}$$

we can define the *scanning reference profile* $r : \mathbb{R}_+ \to \mathbb{R}^2$ by

$$r(t) = \mathcal{R}_{\mathcal{S}(k)}(t - t_k) \qquad \forall t \in [t_k, t_{k+1}) \ \ \forall k \in \mathbb{Z}_+.$$

One of the known problems associated to the scanning reference profile as defined above is the discontinuity in r that can arise due to the different terminal condition of $\mathcal{R}_{\mathcal{S}(k-1)}$ and the initial condition of the subsequent reference flow $\mathcal{R}_{\mathcal{S}(k)}$. In order to allow the physical implementation of the scanning reference profile, it is common to introduce an admissible stepping time $t_s > 0$ between subsequent reference flows. Using t_s, the *admissible scanning reference profile* $r : \mathbb{R}_+ \to \mathbb{R}^2$ can then be defined by

$$r(t) = \begin{cases} \mathcal{R}_{\mathcal{S}(k)}(t - t_k - kt_s) \\ \qquad \forall t \in [t_k + kt_s, t_{k+1} + kt_s), k \in \mathbb{Z}_+ \\ \\ \mathcal{T}_{\mathcal{S}(k)}(t - t_k - (k-1)t_s) \\ \qquad \forall t \in [t_k + (k-1)t_s, t_k + kt_s), k \in \mathbb{Z}_+ \end{cases}$$

where for every k, $\mathcal{T}_{\mathcal{S}(k)} : [0, t_s) \to \mathbb{R}^2$ is any admissible trajectory that connects the terminal condition of scanning reference profile $\mathcal{R}_{\mathcal{S}(k-1)}$ with the initial condition of $\mathcal{R}_{\mathcal{S}(k)}$.

Using the above definitions, we can now define the chopper scanning control problem as follows.

Chopper scanning control problem: For the system (3.1), design a control law $u = K(t, x)$ where K can be a dynamical controller such that:
1) For $r(t) = 0$ the origin is an asymptotically stable equilibrium
2) For $r(t) \neq 0$ the output y converges to r asymptotically during the integration periods of the observation.

For solving the chopper scanning control problem as defined above, we formulate a hybrid control strategy. A sketch of this strategy is given in Section 3.2.

3.2 Introduction to the proposed hybrid control strategy

In this section, to introduce our hybrid control strategy, we give a qualitative formulation of the method developed for high performance reference tracking of the MCCD. The formal description of the method, and the proof of output regulation is given in the subsequent sections.

In Section 1.1.3 it has been mentioned that a typical astronomical observation consists of periods of integration on the source and possibly fast steps from the end of one integration profile to the start position of the next. The integration periods are related to the servomechanism problem discussed in Section 1.2.1. The steps do not require the accurate tracking of a given reference profile (as long as certain plant limitations are accounted for), which means that the control strategy applied here is related to the field of point-to-point control.

The general block diagram describing the hybrid control architecture is given in Fig. 3.1. Different from the standard MbFF approach we do not sum the FF input and the action from the closed loop controller, but we apply only the FF signal during the step and switch to the feedback controller after the step. This avoids possible negative influences of the feedback controller as a result of its limited bandwidth in relation to the fast changing reference profile [56], which is discussed in more detail in Section 3.6.

The feedback controller, related to the robustness of the closed loop system to disturbances and noise sources, should be tuned for every practical application separately depending on the specific system dynamics, the present noise sources and disturbances and the system requirements. It includes an internal model of the exosystem flow dynamics which generates the reference profile during the integration periods. The trigger determines the moment of switching.

To asymptotically track a combination of different reference flows during one observation (for example when chopping between two constant reference positions), we include memory states and switch the active control states related to tracking of the current reference flow with the passive memory states applicable to the next reference flow at the start of each new integration period. Before memorizing, the active control states related to the internal model are reset to their initial conditions, which after convergence guarantees zero error tracking directly at the start of every new reference flow (this also implies a bumpless transition when switching between feedforward and feedback control).

As the proposed strategy requires switching of the system between feedforward and feedback control, which involves memorizing of and switching between different sets of control

states at every start of a scanning period, proof of output regulation is not trivial. The structure of the controller and the results on hybrid output regulation motivated us to formulate the complete system in the hybrid framework, which is discussed in more detail in Section 3.3.

The point-to-point control method applied for the stepping between different scanning profiles is described in Section 3.5.

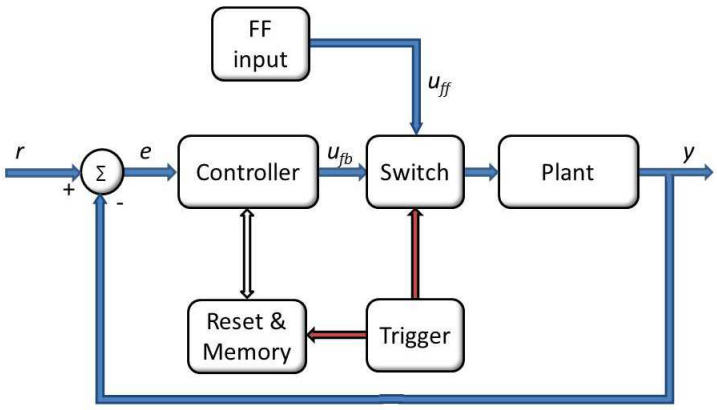

Figure 3.1: Hybrid controller layout. The FF input is applied without the feedback controller during the steps. After the step the feedback controller is activated and the feedforward signal is switched off. At the start and at the end of every step the switch is triggered and the control states, related to the internal model, are reset, memorized and interchanged.

3.3 Hybrid system description

Suppose that the minimal-time problem, that corresponds to the optimal control problem of reaching the nominal initial state $x(t_k + kt_s)$ related to the tracking of $\mathcal{R}_{\mathcal{S}(k)}$ from the terminal state $x(t_k + (k-1)t_s)$ of the previous integration period (with the input constrained within a compact set U and with, possibly, state constraints) is solvable and the minimal time t_{min} is always less than the settling time requirement t_{set}, i.e., $t_{min} < t_{set}$. Hence, we can define a constant $t_s > 0$ such that $t_{min} \leqslant t_s \leqslant t_{set}$ holds for all possible desired positions. Let $t_j^+ = t_j + t_s \forall j \in \mathbb{N}$ and let $u_j : [t_j, t_j^+] \to U$ denote the input signal that brings the plant from the point (x_j, u_j) at time t_j to (x_j^+, u_j^+) at t_j^+. Such constrained input signals u_j exist by the solvability of the minimal-time problem.

Observe that by applying u_j to (3.1) for any arbitrary initial state x_j and initial time t_j, we have

$$x(t_j^+) = M_G x(t_j) + N_j \qquad \forall j \in \mathbb{N}, \tag{3.2}$$

where the plant transition matrix $M_G := \exp(A_G t_s)$ and

$$N_j = \int_{t_j}^{t_j^+} \exp(A_G(t_j^+ - \lambda)) B_G u_j(\lambda)\, \mathrm{d}\lambda.$$

Eq. (3.2) resembles the jump dynamics in the hybrid system framework. Thus if we apply the input signal u_j at the time interval $t \in [(j+1)t_{obs} + jt_s, (j+1)(t_{obs}+t_s)]$, where t_{obs} defines the length of the observation period between two consecutive steps, then the dynamics of the plant can be rewritten in the hybrid systems formulation by defining the hybrid time domain E as follows.

We first define the control input u by

$$u(t) = \begin{cases} u_j(t) \;\; \forall t \in [(j+1)t_{obs} + jt_s, (j+1)(t_{obs}+t_s)] \\ \qquad \forall j \in \mathbb{N} \\ v(t) \qquad \text{otherwise} \end{cases} \tag{3.3}$$

where v is an additional control signal that can be used for feedback control. Let $\Omega : \mathbb{R}_+ \to \bigcup_{j=\mathbb{N}} [j(t_{obs}+t_s), (j+1)t_{obs} + jt_s]$ be the time-warping map and $\Omega(\tau) = \lfloor \tau / t_{obs} \rfloor t_s + \tau$ for all $\tau \in \mathbb{R}_+$. In other words, the range of Ω is the time intervals where u_j is not applied. Using the time-warping map Ω and following [23], we can define the hybrid time domain E by

$$E := \bigcup_{j=\mathbb{N}} [jt_{obs}, (j+1)t_{obs}] \times \{j\}.$$

The dynamics of x on E can equivalently be described by the following hybrid system

$$\left.\begin{array}{rll} \dot{\tau}_c &= 1 & \\ \dot{\zeta} &= A_G\zeta + B_G v(\Omega(\tau)), \;\; \zeta(0,0) = \zeta_0 & \forall (\tau_c, \zeta, v) \in [0, t_{obs}] \times \mathbb{R}^{2n} \times \mathbb{R}^2 \\ & & \\ \tau_c^+ &= 0 & \\ \zeta^+ &= M_G\zeta + N_j & \forall (\tau_c, \zeta) \in t_{obs} \times \mathbb{R}^{2n} \\ y &= C_G\zeta, & \end{array}\right\} \tag{3.4}$$

where $\zeta_0 = x(\Omega(\tau_0))$, v is the additional control signal as before and τ_c is a clock variable with a dwell time t_{obs} which defines the moment of jumping of the system. By direct evaluation of the solution x to (3.1) and by noticing that the initial condition ζ_0 is related to x, we obtain that $x(\Omega(\tau)) = \zeta(\tau, j)$ holds $\forall (\tau, j) \in E$.

This reformulation of the plant dynamics into hybrid setting opens the possibility of assigning optimal control solutions during the first t_s seconds (which are computed off-line for the nominal positions) and implementing a hybrid feedback controller to stabilize the system.

Following the hybrid output regulation setting as in [42], we can adopt the following exosystem which generates the reference signal r and is also defined on the hybrid time domain E as above

$$\left.\begin{array}{rll} \dot{\tau}_c &= 1 & \\ \dot{w} &= Sw, \;\; w(0,0) = w_0 & \forall (\tau_c, w) \in \mathcal{W} \\ & & \\ \tau_c^+ &= 0 & \\ w^+ &= Jw & \forall (\tau_c, w) \in \mathcal{W} \cap (\{t_{obs}\} \times \mathbb{R}^s) \\ r &= Qw, & \end{array}\right\} \tag{3.5}$$

where

$$S = \begin{bmatrix} S_1 & 0 \\ 0 & S_2 \end{bmatrix} \quad J = \begin{bmatrix} J_1 & 0 \\ 0 & J_2 \end{bmatrix} \quad Q = \begin{bmatrix} Q_1 & 0 \\ 0 & Q_2 \end{bmatrix}$$

with

$$S_i = \begin{bmatrix} \Upsilon_i & 0 \\ 0 & 0 \end{bmatrix}_{(4q\times 4q)} \quad \Upsilon_i = \begin{bmatrix} 0 & \omega_{n_i} & 0 & 0 \\ -\omega_{n_i} & 0 & 0 & 0 \\ 0 & 0 & 0 & 1 \\ 0 & 0 & 0 & 0 \end{bmatrix} \quad J_i = \begin{bmatrix} 0 & I_{(4*(q-1))} \\ M_{e_i}^{-1} & 0 \end{bmatrix}$$

$$M_{e_i} = \exp(\Upsilon_i * t_{obs}) \qquad Q_i = \begin{bmatrix} 1 & 0 & 1 & 0 & 0_{(1\times(4(q-1))} \end{bmatrix}$$

and

$$w = \begin{bmatrix} w_1 & w_2 \end{bmatrix}^T \; w_i = \begin{bmatrix} w_{i1} & w_{i2} & \dots & w_{iq} \end{bmatrix} \; q \in \mathbb{N}$$
$$w_{ip} = \begin{bmatrix} w_{ip1} & w_{ip2} & w_{ip3} & w_{ip4} \end{bmatrix}.$$

Finally $\mathcal{W} := \{(\tau_c, w) : \tau_c \in [0, t_{obs}], w \in W(\tau_c)\}$, where the set valued mapping $\tau_c \to W(\tau_c) \subset \mathbb{R}^s$ is continuous with compact values. The parameters ω_{n_1} and ω_{n_2} are the angular velocity of oscillators 1 and 2, respectively. The matrices M_{e_1} and M_{e_2} are the transition matrices related to respectively Υ_1 and Υ_2. The presence of the inverse of these terms in the jump matrix J guarantees that the active exo-state variables are reset to their initial value after every period of flow, even if $t_{obs} \neq 2\pi/\omega_{n_i}$. Based on the above hybrid exosystem and corresponding to our intended application, we consider any reference flow $\mathcal{R}_p$ that can be defined by the four states w_{ip}. The initial condition $w_0 := w(0,0)$ defines the amplitude and phase of oscillation and the start position and constant velocity of the reference signal.

The defined exosystem can generate all astronomical observation modes that are discussed in [33], except for spiral chopping. The reference signal can be generated by choosing the appropriate initial conditions in combination with the required form of N_j to jump between the different flow sets. These initial conditions are summarized in Table 3.1.

Based on this exosystem description and applying the internal model principle as in [42], the hybrid controller can now be described in the following way

$$\left.\begin{array}{rll} \dot{\tau}_c &= 1 & \\ \dot{\xi} &= A_C\xi + B_C e, \quad \xi(0,0) = \xi_0 & \forall(\tau_c, \xi, e) \in [0, t_{obs}] \times \mathbb{R}^m \times \mathbb{R}^2 \\ \tau_c^+ &= 0 & \\ \xi^+ &= \Phi\xi + \Psi e & \forall(\tau_c, \xi, e) \in \{t_{obs}\} \times \mathbb{R}^m \times \mathbb{R}^2 \\ v(\Omega(\tau)) &= C_C\xi + D_C e & \end{array}\right\} \tag{3.6}$$

where

$$A_C = \begin{bmatrix} A_{C1} & 0 \\ 0 & A_{C2} \end{bmatrix} \qquad A_{Ci} = \begin{bmatrix} \star & 0 \\ 0 & S_i \end{bmatrix}$$

$$B_C = \begin{bmatrix} \star & B_{C1} & 0 & 0 \\ 0 & 0 & \star & B_{C2} \end{bmatrix}^T$$

$$B_{C1} = \begin{bmatrix} k_1 & 0 & k_2 & k_3 & 0_{(1\times(4(q-1)))} \end{bmatrix}$$

$$B_{C2} = \begin{bmatrix} k_4 & 0 & k_5 & k_6 & 0_{(1\times(4(q-1)))} \end{bmatrix}$$

$$C_C = \begin{bmatrix} \star & Q_1 & 0 & 0 \\ 0 & 0 & \star & Q_2 \end{bmatrix} \qquad D_C = \begin{bmatrix} \star \end{bmatrix}$$

$$\Phi = \begin{bmatrix} I_{(m/i-4q)} & 0 & 0 & 0 \\ 0 & J_1 & 0 & 0 \\ 0 & 0 & I_{(m/i-4q)} & 0 \\ 0 & 0 & 0 & J_2 \end{bmatrix} \quad \Psi = \begin{bmatrix} \star & 0 \\ 0 & 0 \\ 0 & \star \\ 0 & 0 \end{bmatrix},$$

the parameters k_i, $i = 1, \ldots, 6$ are controller gains. The elements in $\star$ are related to the design of a robust feedback controller and can be designed according to each different application. The identity matrices in Φ indicate that the states related to $\star$ are not changing as a result of the jump. The $J_i's$ in the ϕ matrix are identical to the jump matrices of the exosystem. Again the inverse of M_{e_i} guarantees that in the steady state, the active control states related to the internal model jump back to the correct initial state at the end of the flow period. The variable e is the error signal, i.e., $e = r - C_G\zeta$.

Table 3.1: The exo-state initial conditions that are relevant for different observing modes as discussed in [33]. The variable q defines the number of unique scanning reference profiles which constitute an observation mode, i stands for the DoF. The initial exo-state $w_{ip}(0,0)$ gives the initial condition for any of the profiles in both DoF's with $(\alpha_p, \beta_p, \dot{\alpha}_p, \dot{\beta}_p, Os) \in \mathbb{R}$

Obs. mode	q	i	w_{ip1}	w_{ip2}	w_{ip3}	w_{ip4}
Stare	1	1	0	0	α_p	0
		2	0	0	β_p	0
Chopping	2	1	0	0	α_p	0
		2	0	0	β_p	0
DREAM	12	1	0	0	α_p	0
		2	0	0	β_p	0
Random	> 1	1	0	0	α_p	0
		2	0	0	β_p	0
OTF	> 1	1	0	0	α_p	$\dot{\alpha}_p$
		2	0	0	β_p	0
B.B.B.[1]	> 1	1	0	0	α_p	$\dot{\alpha}_p$
		2	0	0	β_p	$\dot{\beta}_p$
Lissajous [2]	1	1	Os_{11}	Os_{12}	0	0
		2	Os_{21}	Os_{22}	0	0

[1] Requires multiple t_{obs}
[2] Requires $\omega_{n_1} \neq \omega_{n_2}$

The complete closed loop hybrid system is given by

$$\left.\begin{aligned} \dot{\tau}_c &= 1, \quad \dot{w} = Sw, \quad w(0,0) = w_0 \\ \begin{bmatrix} \dot{\zeta} \\ \dot{\xi} \end{bmatrix} &= \mathcal{H}_{cl} \begin{bmatrix} \zeta \\ \xi \end{bmatrix} + \mathcal{L}_{cl} w, \quad \begin{bmatrix} \zeta(0,0) \\ \xi(0,0) \end{bmatrix} = \begin{bmatrix} \zeta_0 \\ \xi_0 \end{bmatrix} \\ & \qquad \forall ((\tau_c, w), \zeta, \xi) \in \mathcal{W} \times \mathbb{R}^{2n} \times \mathbb{R}^m \\ \tau_c^+ &= 0, \quad w^+ = Jw \\ \begin{bmatrix} \zeta^+ \\ \xi^+ \end{bmatrix} &= \mathcal{J}_{cl} \begin{bmatrix} \zeta \\ \xi \end{bmatrix} + \mathcal{M}_{cl} w \\ & \qquad \forall ((\tau_c, w), \zeta, \xi) \in (\mathcal{W} \cap (\{t_{obs}\} \times \mathbb{R}^s)) \times \mathbb{R}^{2n} \times \mathbb{R}^m \end{aligned}\right\} \tag{3.7}$$

with

$$\mathcal{H}_{cl} := \begin{bmatrix} A_G - B_G D_C C_G & B_G C_C \\ -B_C C_G & A_C \end{bmatrix} \quad \mathcal{L}_{cl} := \begin{bmatrix} B_G D_C Q \\ B_C Q \end{bmatrix}$$

$$\mathcal{J}_{cl} := \begin{bmatrix} M_G & 0 \\ -\Psi C_G & \Phi \end{bmatrix} \quad \mathcal{M}_{cl} := \begin{bmatrix} N_{w_j} \\ \Psi Q \end{bmatrix}$$

where N_j is related to the exo-state through N_{w_j}, i.e., $N_j := N_{w_j} w$.

Based on the control input for the original plant as in (3.3) and the hybrid control law for the additional control input v as in (3.6), we can now reformulate the chopper scanning control problem in the hybrid framework as follows:

Chopper scanning hybrid control problem: Design a hybrid controller (3.6) for the hybrid plant (3.4) such that the closed-loop system (3.7) has bounded trajectories and $\lim_{t+j\to\infty} e(t,j) = 0$ uniformly.

3.4 Hybrid output regulation for scanning

Let ϕ_{cl} be the state transition matrix of the flow dynamics

$$\begin{bmatrix} \dot{\zeta} \\ \dot{\xi} \end{bmatrix} = \mathcal{H}_{cl} \begin{bmatrix} \zeta \\ \xi \end{bmatrix}.$$

In other words $\phi_{cl}(t_{obs}) = \exp(\mathcal{H}_{cl} t_{obs})$ and $\phi_{cl}(t_0) = I_{n+m}$.

Using the results on output regulation for hybrid systems as discussed in 2.2, the aforementioned chopper scanning hybrid control problem is solvable if and only if there exists an invariant manifold

$$\mathcal{M} = \left\{ ((\tau_c, w), \zeta, \xi) \in \mathcal{W} \times \mathbb{R}^{2n} \times \mathbb{R}^m : \begin{bmatrix} \zeta \\ \xi \end{bmatrix} = \Pi w \right\}$$

which is globally attractive and for which $e = Qw - C_G \zeta$ is equal to zero.

Based on Lemma 2.2.2, the following proposition establishes a necessary and sufficient condition for the existence of an invariant manifold $\mathcal{M}$ which is attractive and has zero error.

Proposition 3.4.1 *Assume that the restriction of $\mathcal{H}_{cl}$ to the active subspace is Hurwitz. Then there exists an attractive invariant manifold $\mathcal{M}$ such that $Qw - C_G\zeta = 0$ if and only if*

$$\gamma := \left| \sigma_{\max} \left(\prod_{h=0}^{l-1} \mathcal{J}_{cl_{(l-h)}} \Phi_{cl}(t_{obs_{(l-h)}}) \right) \right| < 1, \tag{3.8}$$

where $\sigma_{\max}$ is the largest eigenvalue of the matrix and l is the number of scans contained in the smallest repeating sequence of scans with different t_{obs}. In particular, we have that $e = r - C_G\zeta \to 0$ as $\tau + j \to \infty$.

Proof: Without loss of generality, we prove the proposition for the 1 DoF case, i.e., $((w, \zeta, \xi, u) \in \mathbb{R}^{s/2} \times \mathbb{R}^n \times \mathbb{R}^{m/2} \times \mathbb{R})$. As we consider systems with decoupled DoF's the proof is valid for any DoF satisfying the dynamics defined in Section 3.3.

Our assumption on (3.8) is equivalent to the condition **(A1)** but it allows for the use of different t_{obs} in a single reference profile. From this equivalence the necessity of (3.8) for output regulation is directly clear. We recognize that, as our exosystem is neutrally stable (i.e., it has eigenvalues on the imaginary axis), by satisfying **(A1)**, the non-resonance condition **(A2)** holds trivially. In the following, to prove sufficiency of condition (3.8), we will construct explicitly the solution Π that defines our attractive invariant manifold $\mathcal{M}$ with zero error.

It is immediate to check that, to satisfy condition (2.15), we require that $\zeta = \Delta_p w$ where

$$\Delta_p = \begin{bmatrix} Q_1 & Q_1 S_1 & Q_1 S_1^2 & \dots & Q_1 S_1^{(n-1)} \end{bmatrix}^T.$$

The corresponding control states, related to the internal model of the controller, can then be formulated as $\xi_{im} = \Delta_c w^*$, where

$$\Delta_c = \begin{bmatrix} 1/b_n (Q_1^* \Upsilon_1^n - C_{G_1} {A_{G_1}}^n \Delta_p^*) \Sigma_1 \\ 1/(\omega_n b_n)(Q_1^* \Upsilon_1^n - C_{G_1} {A_{G_1}}^n \Delta_p^*) \Sigma_1 S_1 \\ 1/b_n (Q_1^* \Upsilon_1^n - C_{G_1} {A_{G_1}}^n \Delta_p^*) \Sigma_2 \\ 1/b_n (Q_1^* \Upsilon_1^n - C_{G_1} {A_{G_1}}^n \Delta_p^*) \Sigma_2 S_1 \end{bmatrix}$$

with $\Sigma_1 = \begin{bmatrix} I_{(2)} & 0 \\ 0 & 0 \end{bmatrix}$, $\Sigma_2 = \begin{bmatrix} 0 & 0 \\ 0 & I_{(2)} \end{bmatrix}$, w^* and Q_1^* are the first for elements of w and Q_1, respectively, and Δ_p^* is the matrix consisting of the first four columns of Δ_p. The memorized states are constant and are also related to the states of the exosystem by Δ_c.

Since we have shown that the closed-loop dynamics is internally stable, the control states related to the stabilization of the system vanish in the invariant manifold. The zero error tracking solution of the closed-loop hybrid system can then be related to the exo-states in the following way:

$$\begin{bmatrix} \hat{\zeta} \\ \hat{\xi} \end{bmatrix} = \left[\begin{array}{cccc} & \Delta_p & & \\ \hline & & 0_{(m_\star \times 4q)} & \\ \Delta_c & 0 & \dots & 0 \\ 0 & \Delta_c & \dots & 0 \\ \vdots & \vdots & \ddots & \vdots \\ 0 & 0 & \dots & \Delta_c \end{array}\right] w, \tag{3.9}$$

where the $m_\star$ stands for the number of control states related to the stabilization of the system.

We use (3.9) as a candidate for the Π matrix which defines the invariant manifold of (3.7). By recognizing that by the solvability of the minimum time problem $N_{w_j} = \Pi_x J_1 - M_{G_1}\Pi_x$, where Π_x is the matrix obtained by extracting the first n rows of Π, we can compactly formulate the output regulation equations (2.14) and (2.15) as:

$$\Pi S_1 = \begin{bmatrix} A_{G_1} & B_{G_1}C_{C_1} \\ 0 & A_{C_1} \end{bmatrix} \Pi$$
$$\Pi J_1 = \left[\begin{array}{cc} M_{G_1} & 0 \\ 0 & \Phi_1 \end{array}\right] \Pi + \left[\begin{array}{c} \Pi_x J_1 - M_{G_1}\Pi_x \\ \hline 0 \end{array}\right].$$

where M_{G_1} and Φ_1 are not explicitly defined but represent the 1 DoF version of M_G and Φ. This shows that (3.9) satisfies our regulator equations (2.14) and (2.15).

Finally, by Lemma 2.2.2, we achieve output regulation of the hybrid closed-loop system (3.7). □

To illustrate what we exactly mean by l in (3.8), as an example a 1 DoF reference profile is given in Fig. 3.2. Two different t_{obs} are required to describe this profile. The smallest repeating sequence of observation times is defined by $(t_{obs_1}, t_{obs_1}, t_{obs_2})$ which means that $l = 3$ in this specific case. We further note that the shape of the different reference flows is completely defined by the initial conditions of w and is not important here, if t_{obs_1} would be equal to t_{obs_2}, the use of $l = 1$ in (3.8) would suffice.

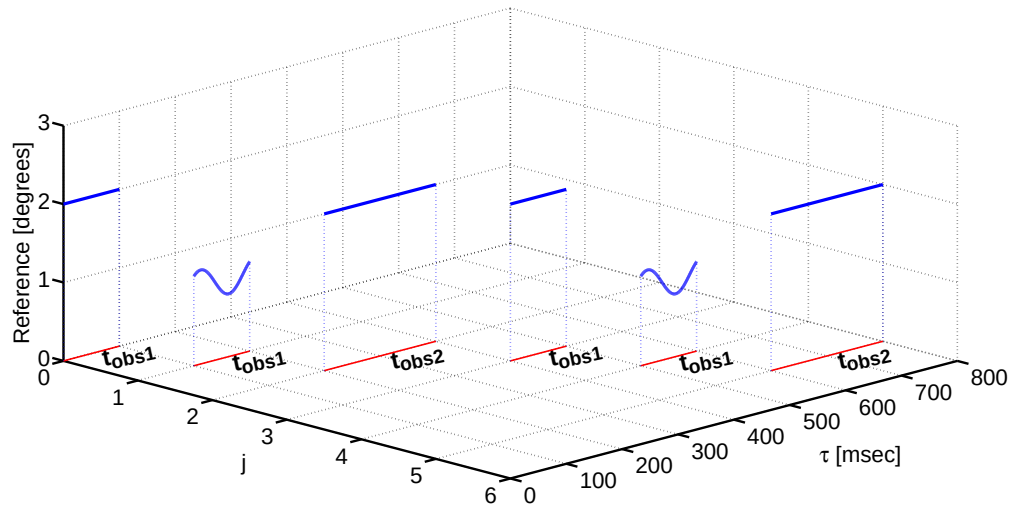

Figure 3.2: Example of a 1 DoF reference profile (blue) on hybrid time domain E (red) where two different integration times (t_{obs_1} and t_{obs_2}) are combined in one observation mode.

3.4.1 Practical stability

In the foregoing discussion we assumed that $\mathcal{T}_{\mathcal{S}(k)}$ is ideal. In practice, this is typically not the case as plant uncertainties, unmodeled dynamics, plant limitations and noise sources influence the step. The result will be minor offsets of the initial flow state from the invariant manifold. The non-ideal term N_j', related to the feedforward design during stepping, can however never destabilize the plant as shown in the following proposition.

Proposition 3.4.2 *Consider* (3.7) *with a non-ideal N_j in $\mathcal{M}_{cl}$ given by $N_j' = N_{w_j} w + \Delta$. Then for every initial conditions $\left[\zeta(0,0)\ \xi(0,0)\right]^T$ and for every $|\Delta| < \infty$, we have that $\lim_{j\to\infty} \left[\zeta(\tau_0, j)\ \xi(\tau_0, j)\right]^T$ is bounded.*

Proof: As N_j' in general cannot be expressed in terms of w, we cannot apply the approach in [42] for the proof of stability. Instead by first defining

$$\begin{bmatrix}\zeta(t_{obs}, j)\\ \xi(t_{obs}, j)\end{bmatrix} = \phi_{cl} \begin{bmatrix}\zeta(\tau_0, j)\\ \xi(\tau_0, j)\end{bmatrix} + \mathcal{C}_{fl}$$

where

$$\mathcal{C}_{fl} = \int_{\tau_0}^{t_{obs}} exp(\mathcal{H}_{cl}(t_{obs} - \lambda))\mathcal{L}_{cl} r(\lambda)\, \mathrm{d}\lambda,$$

we can formulate the propagation of the state as follows:

$$\begin{bmatrix}\zeta(\tau_0, j)\\ \xi(\tau_0, j)\end{bmatrix} = (\mathcal{J}_{cl}\phi_{cl})^j \begin{bmatrix}\zeta(0,0)\\ \xi(0,0)\end{bmatrix} + \textstyle\sum_{i=0}^{j-1} (\mathcal{J}_{cl}\phi_{cl})^i \mathcal{J}_{cl}\mathcal{C}_{fl} + \sum_{i=0}^{j-1} (\mathcal{J}_{cl}\phi_{cl})^i \mathcal{C}_{ju}, \tag{3.10}$$

where

$$\mathcal{C}_{ju} = \begin{bmatrix}0\\ \Psi Q\end{bmatrix} w + \begin{bmatrix}N_j'\\ 0\end{bmatrix}.$$

Examining the three terms on the right hand side of (3.10) separately for the non-trivial case of $\left[\zeta(0,0)\ \xi(0,0)\right]^T$, $\mathcal{C}_{fl}$ and $\mathcal{C}_{ju}$ not all zero, we can directly conclude that the first term will vanish if **(A1)** is satisfied. The last two terms both require the given sum to be finite. By eigenvalue decomposition of $\mathcal{J}_{cl}\phi_{cl}$ we have that

$$\sum_{i=0}^{j-1} (\mathcal{J}_{cl}\phi_{cl})^i = \mathcal{Q} \sum_{i=0}^{j-1} \mathcal{R}^i \mathcal{Q}^{-1}$$

where $\mathcal{Q}$ is the matrix with the eigenvectors of $\mathcal{J}_{cl}\phi_{cl}$ as its columns and $\mathcal{R}$ is the diagonal matrix with the eigenvalues $\{\sigma_i\}_{i=1\ldots n+m}$ of $\mathcal{J}_{cl}\phi_{cl}$ on the diagonal. Now if **(A1)** is satisfied we can write

$$\lim_{j\to\infty} \sum_{i=0}^{j-1} \mathcal{R}^i = \begin{bmatrix} \frac{1}{1-\sigma_1} & 0 & \dots & 0 \\ 0 & \frac{1}{1-\sigma_2} & \dots & 0 \\ \vdots & \dots & \ddots & 0 \\ 0 & \dots & 0 & \frac{1}{1-\sigma_{n+m}} \end{bmatrix} = \bar{\mathcal{R}},$$

by recognizing that in the given sum, all diagonal entries form a geometrical series which converges to $\frac{1}{1-\sigma_i}$. So if $(A1)$ is satisfied $\sum_{i=0}^{j-1}(\mathcal{J}_{cl}\phi_{cl})^i = \mathcal{Q}\bar{\mathcal{R}}\mathcal{Q}^{-1} < \infty$.

We can conclude that **(A1)** guarantees stability of (3.7) even if N_j is not ideal. □

3.5 Practical FF design by offline optimization

Consider the plant dynamics in (3.1). The FF signal u_j can be generated by applying quadratic programming to the following optimization problem with input constraints

$$\min_{u\in U} \| \, x_d(t_s) - x(t_s) \, \|_2 \tag{3.11}$$

where U is the set of allowed control inputs $U := \{u_j \in \mathbb{R}^n : |u_{ji}| \leqslant u_{max}\}$, for some maximum allowed input u_{max} based on the system specifications. The state $x_d(t_s)$ is the desired plant state at the end of the step (at time t_s) and $x(t_s)$ is the realized end state as a result of the discrete FF input sequence

$$u_j = \begin{bmatrix} u(0) \\ u(\Delta t) \\ u(2\Delta t) \\ \vdots \\ u(t_s - \Delta t) \end{bmatrix},$$

which can be formulated as follows

$$x(t_s) = e^{A_G t_s} x(0) + \Phi u_j$$

with

$$\Phi = \begin{bmatrix} \phi_1 & \phi_2 & \dots & \phi_n \end{bmatrix}$$

and

$$\phi_i = A_G^{-1} e^{A_G(t_s - t_i)}(I - e^{-A_G \Delta t}) B_G$$

where t_i stands for the start time of discrete input u_{ji} and Δt is the sampling time. We include inequality constraints in the optimization to limit the allowed changes between adjacent discrete steps of the FF signal, which smooths the input profile and therefore reduces residual vibration. These constraints can be formulated as follows

$$\mathcal{M} u_j \leqslant b$$

with

$$\mathcal{M} = \begin{bmatrix} -1 & 1 & 0 & 0 & \dots & 0 \\ 1 & -1 & 0 & 0 & \dots & 0 \\ 0 & -1 & 1 & 0 & \dots & 0 \\ 0 & 1 & -1 & 0 & \dots & 0 \\ \vdots & & \ddots & & & \end{bmatrix},$$

and the vector b contains the limits which define the allowed changes between individual inputs u_{ji}. This approach can handle input constraints, allows for smoothing of the input signal and deals with the discrete nature of the FF input naturally. Practical considerations relating the application of the method to the MCCD hardware are discussed in 6.3.1.

3.6 Relation to other high performance control strategies

When considering fast motion profiles, as the closed loop system bandwidth itself is typically insufficient, it is standard to use a feedforward controller for fast stepping in parallel with a feedback controller for stability robustness and noise reduction. The design of an accurate FF input is non trivial, especially if higher order dynamics have to be taken into account [5] and [60].

Typically, if reference profiles with high frequency content are considered, the tracking ability is limited, resulting in non ideal initial conditions at the start of the integration period. The important difference in our approach w.r.t. standard MbFF, is that the closed loop controller is only active during the integration periods. It is turned off during the step to avoid possible negative influences of the feedback loop on settling as a result of its limited bandwidth [56] and integrator build up during the step.

To illustrate this, we first simulate the response of a critically damped plant $P_e = \frac{10^4}{(s^2+2.10^2 s+10^4)}$ with integral control $C_e = \frac{10}{s}$ to a smooth but very fast reference trajectory designed by the method described in [36]. We compare the hybrid method with the MbFF technique and with MbFF with a Clegg integrator reset element [11] in the feedback path (MbFF-R). As we are not obliged to the use of the method described in 3.5 for the generation of the FF input, and for the sake of comparison, we apply the same FF input to all three control strategies. The FF input is generated by passing the reference signal through an inverse plant model with a first order low pass filter (bandwidth = 10^3 rad/s).

Fig. 3.3 shows the results of the simulation. The quality of the FF input is limited by the necessary use of the low pass filter. For both model based FF strategies we observe integrator build up during the step which increases the momentum of the plant. The combination of the integrator build up and the extra momentum gained during the first 10 msec of the step cause the large overshoot observed when applying the MbFF technique. The reset controller resets the integrator to zero when crossing the zero error line but still experiences overshoot as a result of the increased momentum. The hybrid controller has no integrator build up during the step and considerably reduces the settling time of the plant.

As a next step we simulate the effect of the step time of the reference profile on the settling time of a second order plant for the MbFF and the hybrid strategy. For completeness we also include the result when applying the feedback loop without the FF path. The FF signal is based on an inverse plant model which exhibits frequency dependent inaccuracies. We apply a PID controller which is tuned for a certain bandwidth and limited overshoot of the closed loop plant. The different configurations studied are summarized in Table 3.2.

For clarity the effect of noise and disturbances is excluded from the results as, for the field of nanopositioning, this will typically affect the positional stability of the plant before it has a significant effect on settling time. Plant constraints are not considered in the simulation.

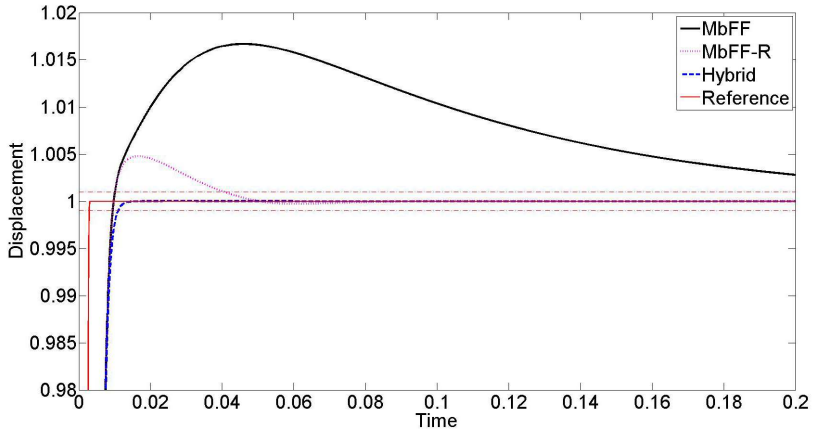

Figure 3.3: Comparison of fast reference tracking for different control strategies. The 4^{th} order reference profile performs the step from 0 to 1 in 2.9 msec. The horizontal dashed lines give the tolerance band for settling within 0.1% of the step. Settling for MbFF = 277 msec, for MbFF-R = 41 msec and for Hybrid = 11 msec.

Table 3.2: Plant configurations studied to illustrate the effect of reference step time on settling. Configurations 1 and 2 represent a critically damped plant. The FF signal is based on a plant model inverse with high frequency inaccuracies modelled by a 1000 rad/sec bw. low pass filter. Configurations 3 and 4 describe a plant with a resonance. The model mismatch is in the limited representation of the resonance. For both scenarios PID controllers are tuned with different cl. bandwidths.

Config.	**Plant**	**Inverse plant model**	**PID parameters**	**Cl. bw. [rad/sec]**
1	$\frac{10^4}{s^2+2\times10^2 s+10^4}$	$\frac{10^2 s^2+2\times10^4 s+10^6}{s^2+2\times10^3 s+10^6}$	k_p=2 k_i=102 $k_d = 9.83\times10^{-3}$	100
2	″	″	k_p=3.47 k_i=173 $k_d = 1.73\times10^{-2}$	173
3	$\frac{10^4}{s^2+10^2 s+10^4}$	$\frac{10^6 s^2+1.2\times10^8 s+10^{10}}{s^2+2\times10^5 s+10^{10}}$	k_p=1.12 k_i=81.5 $k_d = 3.85\times10^{-3}$	100
4	″	″	k_p=2.57 k_i=137 $k_d = 1.21\times10^{-2}$	173

Figure 3.4 shows the results of the simulations. The hybrid controller outperforms the MbFF for fast reference profiles. For slower reference profiles the closed loop improves the tracking of the reference and the MbFF approach shows slightly better results. As can be expected, increasing the closed loop bandwidth reduces the settling time.

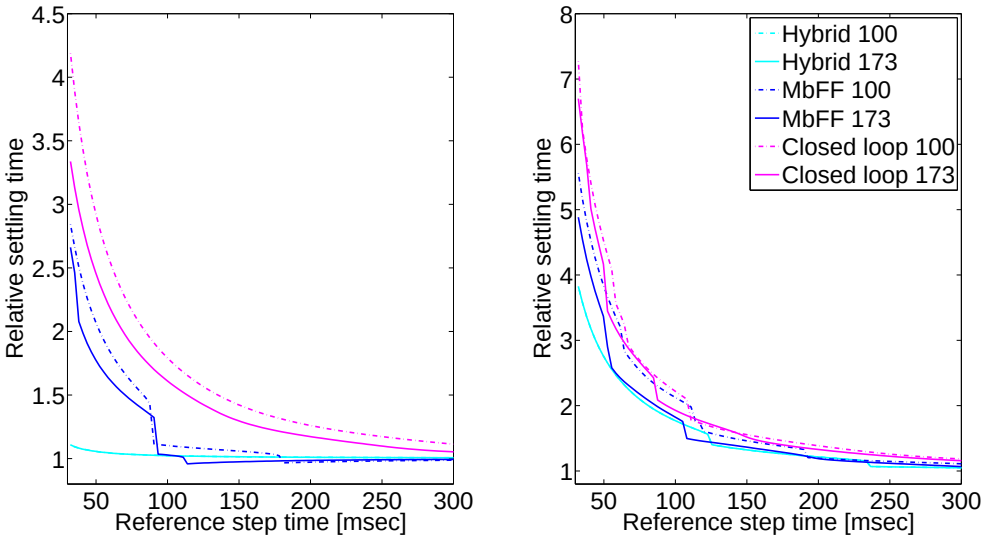

Figure 3.4: Effect of step time of reference profile on settling time of system configurations given in Table 3.2, for the hybrid, MbFF and closed loop only control strategies (Left: results for config. 1 and 2. Right: results for config. 3 and 4). The relative settling is defined as the settling time of the plant normalized by the applied reference step time. The Hybrid 100 and 173 results largely overlap because of the limited influence of the PID controller after the step (as a result of the very small error signal).

The results vary with every specific configuration, but generally speaking it can be concluded that for fast reference profiles, with respect to the typically limited controller bandwidth, open loop stepping performs better.

3.7 Concluding remarks

We have formulated a new control strategy for output regulation of fast stepping nanopositioning mechanisms. In the method we switch between an open loop feedforward input for fast stepping and a closed loop controller, which satisfies the internal model principle, for accurate tracking and high positional stability during periods of flow. Control states related to the internal model are reset, memorized and interchanged after every integration period of the mechanism. Resetting of the control states is similar to reset control [11] and impulsive control [69], where the state of a feedback controller is subject to sudden changes dictated by the reference profile or the tracking error. A clear distinction with our method however is the definition of the initial control states at the start of every flow and that we perform the step in open loop.

We have defined necessary and sufficient conditions for output regulation of different scanning reference profiles given in [33] by reformulating the system in the hybrid framework and applying the results of [42].

In practice, limitations in the accuracy of the FF signal will always result in small offsets from the invariant manifold which describes zero error tracking, directly after the jump. The result on practical stability proves that these limitations can never destabilize the hybrid system.

The strategy is compared (in simulation) to other high performance control strategies to show the advantageous of open loop stepping when tracking reference profiles with high frequency content.

The strategy is applied to the HIFI-FPC in Chapter 5 and to the MCCD in Chapter 6.

Chapter 4

Cryogenic mechatronic design of the HIFI Focal Plane Chopper

The difficulties encountered during the development of the HIFI-FPC, motivated us to study the possibility to apply more advanced control strategies for application in future chopper mechanisms to further improve the performance of these mechanisms, as has been discussed in Section 1.3.1. These efforts resulted in the hybrid control strategy, which has been described in Chapter 3. In Chapter 5 we discuss the synthesis and application of this new control strategy to the HIFI-FPC and we show how this can lead to a large improvement in performance without the need for detailed redesign of the hardware.

This chapter presents the mechatronic design of the HIFI-FPC and several technical considerations in achieving nominal operation at 15 K with strict performance requirements and environmental constraints. It shows how the constraints in material choice, differences in CTE, etc. influence the design, assembly and test campaign of the hardware and gives a flavour of this field of engineering/research. The performance of the flight model of the HIFI-FPC, before integration with the HIFI instrument and during operation in space, are presented applying the original controller. The issues discussed here are directly applicable to the development and testing of the MCCD which are discussed in Chapter 6.

In Section 4.1, the design of the HIFI-FPC is given focusing on the mechatronic components and the control of the system. The different aspects, related to the development of the HIFI-FPC mechanism for operation in cryogenic conditions, are discussed in Section 4.2. In Section 4.3, the performance of the HIFI-FPC both in the test lab and in space is presented. We conclude with an outlook on the demands on thermal behavior of mechanisms in future space missions.

The results in this chapter are published in [26].

4.1 HIFI Focal Plane Chopper

4.1.1 HIFI-FPC requirements

Table 4.1 summarizes the HIFI-FPC design requirements related to the dynamical performance of the mechanism. This is not a complete overview of the requirements but gives the relevant parameters for the mechatronic and control design of the instrument. The required chop frequency of the mechanism, for chopping between an astronomical source and a background position, is 5 Hz. The settling time of the mechanism is limited to 40 ms in order to minimize the dead time when chopping between the on- and off-source positions. Table 4.2 gives a list of the standard chopper positions. The associated orientations of the telescope beam on the sky and on the internal calibration loads are also given. The stringent settling time requirement

is only applicable to the 4.9° chop range for chopping between different sky positions. This requirement is relaxed for chopping to the calibration source.

The performance requirements, given in Table 4.1, in combination with the design limitations introduced by the cryogenic environment, demand a careful mechatronic design of the mechanism.

Table 4.1: HIFI-FPC requirements and realized performance. Measurements were performed in the lab at an operating temperature of 9 K.

Description	Requirement	Result	Unit	Remark
Pos. stability	< 30	2	[”]	1σ
Pos. repeatability	< 90	17	[”]	Max. allowed offset
Pos. resolution	$\leqslant 60$	25	[”]	
Settling time	$\leqslant 40$	38	[ms]	0.5% criterion
Power dissipation	$\leqslant 2$	2	[mW]	for 5Hz chop over 4.9°
Chop range	15	✓	[°]	
LVDT resolution	< 30	1	[”]	
LVDT linear stroke	9	✓	[mm]	
LVDT noise level	$\leqslant 0.9$	✓	[mV]	
Pivot lifetime	$> 10^8$	✓	[cycles]	over 5° chopangle

Table 4.2: Relation between the chop angle of the HIFI-FPC and the actual orientation of the HIFI beam. The total chop range of 15° is limited by the end stops. CBB stands for Cold Black Body and HBB stands for Hot Black Body

Chop angle	HIFI beam orientation
-4°	Endstop position (outside observing range)
-2.45°	-1.5” on the sky
0°	0° on the sky
+2.45°	+1.5” on the sky
+8°	HIFI internal CBB
+10.4°	HIFI internal HBB
+11°	Endstop position (outside observing range)

4.1.2 Instrument description

Fig. 4.1 shows the final flight model of the HIFI-FPC. The mirror can rotate around its vertical axis over a total angle of 15 degrees. The total weight of the HIFI-FPC is 520 grams, the rotatable mirror assembly weighs 125 grams. The height of the chopper is 140 mm.

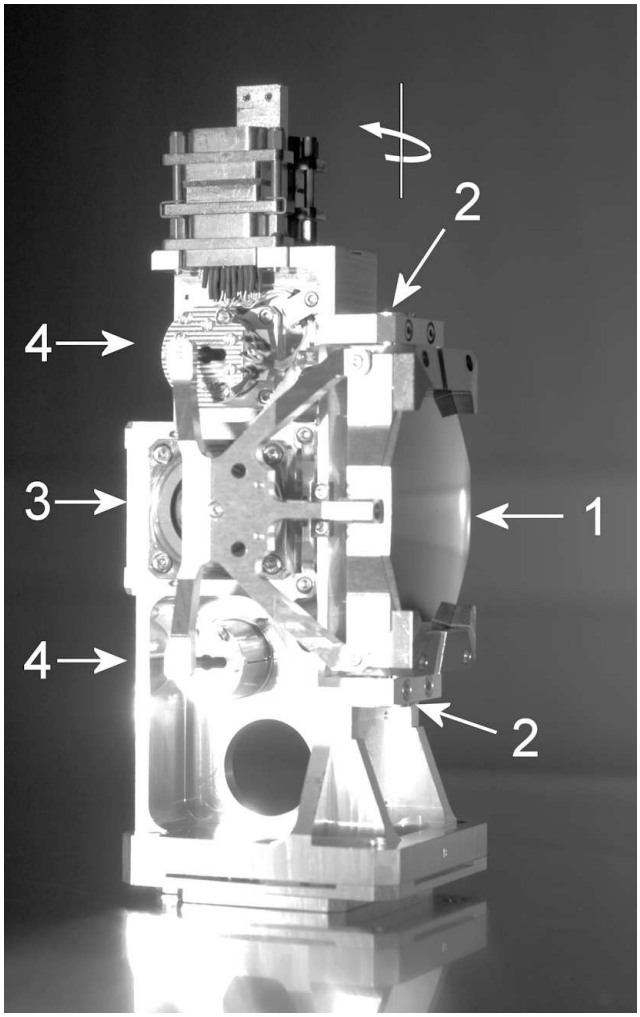

Figure 4.1: Flight model of the HIFI Focal Plane Chopper; 1 = Chopper mirror; 2 = Flexural pivots; 3 = Actuators; 4 = Linear variable differential transformer (LVDT) type position sensors. The positive chop orientation is indicated by the arrow above the mechanism pivot axis.

In Section 4.1.2 - 4.1.2 the critical components which support the rotation of the mirror are described. In all cases frictionless contacts between the frame and mirror assembly have been used. The reason for this choice will be discussed in more detail in Section 4.2.2.

Voice coil actuators

The movement of the mirror is provided by two voice coil type actuators working together in pushpull configuration. Two instead of one actuator have been used for redundancy and to reduce the required power for the rotation of the mirror. The actuators are fed by a current source providing a maximum current of 23.7 mA each. The current limiter is applied to minimize the heat dissipation through the coils.

Fig. 4.2 shows the design of the actuator. The shape of the soft magnetic core as well as that of the permanent magnet is chosen to allow for the required rotational movement of the coil holder in the actuator housing. This non symmetrical shape slightly reduces the efficiency of the actuator but avoids the necessity of a complex construction using various pivotal points that would be needed to convert the rotational movement of the mirror assembly into a translational movement of the actuator coil.

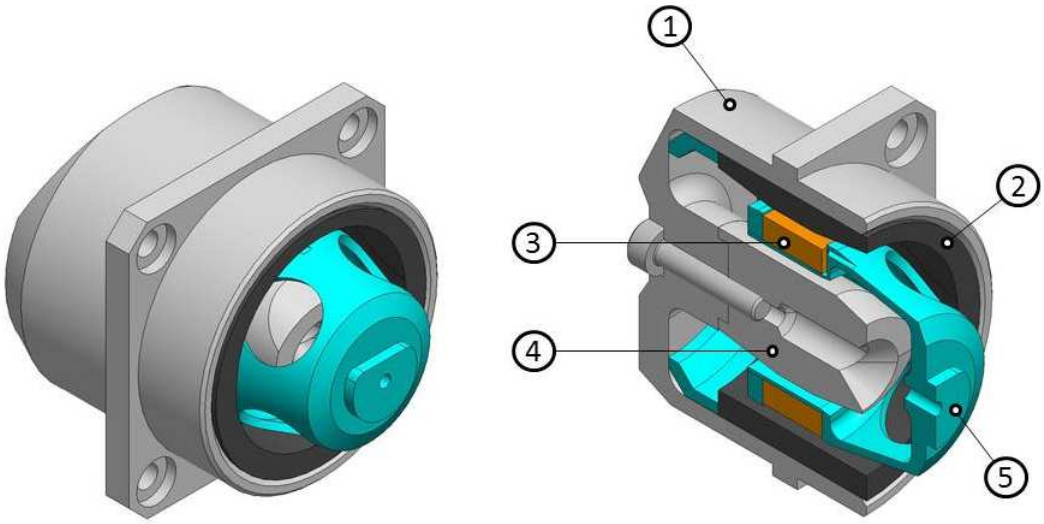

Figure 4.2: Left: Schematic drawing of the HIFI-FPC actuator. Right: Cross section of HIFI-FPC actuator; 1 = Soft magnetic actuator housing, 2 = Permanent magnet, 3 = Coil, 4 = Soft magnetic core of the actuator housing, 5 = Aluminum coil holder attached to the mirror assembly.

The actuator coils, consisting of 2600 turns of Posyn-TH copper wire with a diameter of 50 μm, are stacked in an orthocyclic pattern to optimize the fill factor of the wiring. The wires are isolated using Polyimid insulation with a thickness of 3 μm. The copper wiring is soldered with Sn50Pb48Cu1.5 tin/lead solder depleted with copper to avoid that the copper of the small diameter wire is dissolved in the solder.

To limit the mass and moment of inertia of the mirror assembly, the voice coils of the actuators are attached to the back side of the Chopper mirror. A drawback of this design is that the generated heat is dissipated onto the mirror assembly and that an electrical connection to the movable part of the mechanism has to be created. BerylliumCopper (BeCu) straps have been used to make the electrical connection between the frame and the mirror assembly. The design considerations for using the voice coil as actuator for the HIFI-FPC are presented in Section 4.2.2. The choice of placing the actuator coils on the mirror assembly and not on the HIFI-FPC frame is justified in Section 4.2.3.

LVDT position sensors

In order to accurately determine the orientation of the chop mirror, the instrument is equipped with two linear variable differential transformer (LVDT) type position sensors (see Fig. 4.3). A schematic drawing of the cross section of these sensors is given in Fig. 4.4. The LVDT sensor consists of three coils that are placed in line. The center coil is excited with an alternating voltage and creates a constantly changing magnetic field inside the LVDT unit. The magnetic field is picked up by the two secondary coils generating an alternating current in the electrical circuitry of both coils. A soft iron core, attached to the mirror assembly of the chopper, is placed inside the coil assembly of the LVDT. The coupling of the magnetic field to the two secondary coils is dependent on the actual position of the core in the coil assembly. Therefore, after calibration of the system, the differences in the amplitude of the generated currents in both secondary coils can be used to determine the orientation of the mirror. The HIFI-FPC is calibrated in an optical setup using a theodolite to accurately relate the angular orientation of the mirror to the LVDT readout.

The LVDT response is affected by the temperature-dependent characteristics of the sensor circuitry and the carrier frequency must be chosen carefully in order to reduce its sensitivity to temperature changes. This will be discussed further in Section 4.2.3. In the final design of the HIFI-FPC, the carrier frequency is 2.6 kHz, which is far away from the resonance frequency of the sensor circuitry. Similar coils as for the actuators are used in the LVDT. Only the dimensions and number of windings (2000 turns for the primary coil and 4000 turns for the secondary coils) are different. Only one sensor is active during the operation of the instrument, the other sensor is provided for redundancy.

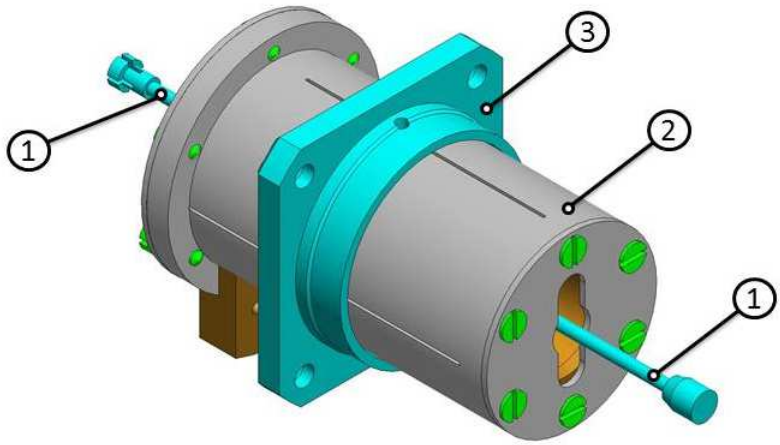

Figure 4.3: HIFI-FPC LVDT position sensor; 1 = Aluminum arms attached to mirror assembly; 2 = Stainless steel casing; 3 = Aluminum interface block for integration with HIFI-FPC frame.

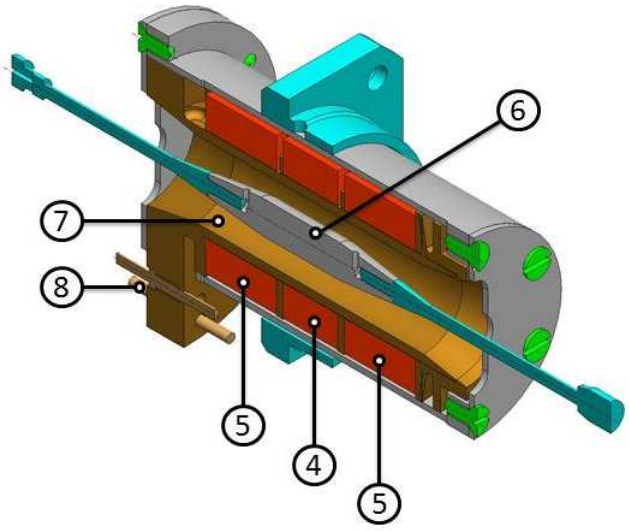

Figure 4.4: Cross section HIFI-FPC LVDT position sensor; 4 = Primary coil; 5 = Secondary coils; 6 = Stainless steel core; 7 = Vespel support structure; 8 = PhosphorBronze connector pins.

Flexural pivots

For supporting the mirror assembly and guiding the rotational movement of the system, Inconel 718 flexural pivots from the C-flex Bearing Company have been used. Fig. 4.5 shows a schematic drawing of the type of pivot used for the HIFI-FPC. The two cylindrical parts of the pivots can be rotated with respect to each other without introducing any friction between the two components. One cylinder is clamped inside the chopper frame and the other cylinder is clamped in the mirror frame (see Fig. 4.6). Clamping instead of gluing or soldering creates the opportunity for alignment of the mirror after the final assembly of the unit.

Figure 4.5: Left: C-flex Inconel 718 flexural pivot. Right: Cross section of flexural pivot showing the two separate cylinders and the three blade springs connecting both parts.

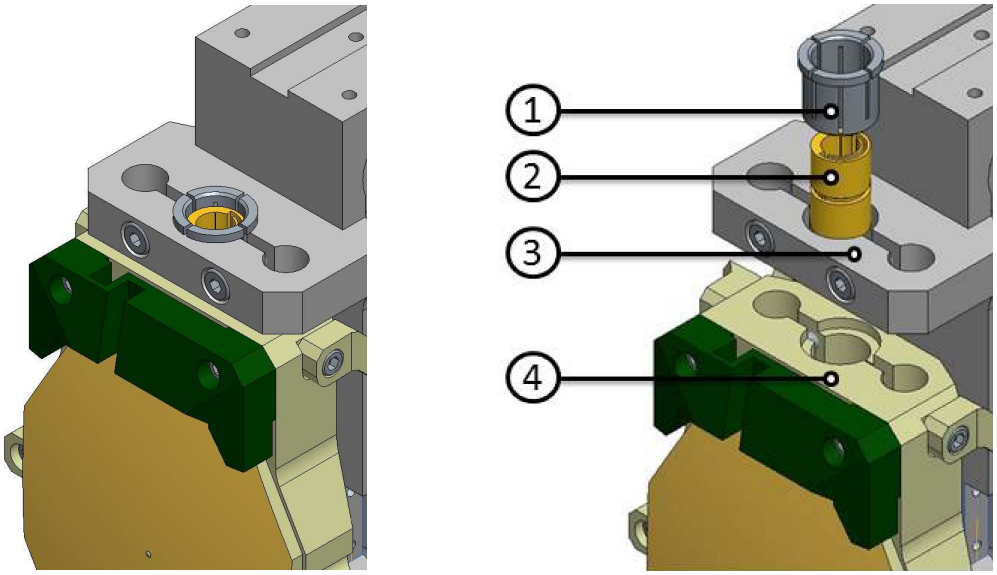

Figure 4.6: Left: Close up of pivot clamp construction in HIFI-FPC frame and mirror. Right: Exploded view of pivot clamp construction; 1 = Clamping bush; 2 = Flexural pivot; 3 = clamp construction in frame; 4 = clamp construction in mirror.

The pivots are thought to be the most critical components with respect to the reliability of the mechanism. When damaged, these units form a single point of failure in the functioning of the HIFI-FPC. The strong demands on their resistance to fatigue and the extreme vibration loads during the launch of the telescope set high requirements on these components.

As there were no standard pivots available which could satisfy all the HIFI-FPC requirements, an elaborate development program was set up in close collaboration between C-flex and SRON. During this program different alloys were examined on strength, resistance to fatigue, quality of welded joints, spring rate, hysteresis and manufacturability. Because of its favorable properties, Inconel was chosen for the flight batch of the pivots.

To guarantee the homogeneity of the production process of all 50 pivots from the flight batch, the same lots of materials were used and the same production procedure was applied to all components by the same operator. Furthermore, to maximize reliability, the units went through an extensive lot acceptance test program as described in Table 4.3.

Table 4.3: Lot acceptance test program for pivot flight production batch of 50 pieces.

Lot acceptance test	**Comments**
Materials and plating certification inspection	
100% visual inspection	Braze appearance, cleanliness, damage
100% dimensional inspection	Outer dimensions, spring clearance, element alignment
One randomly selected piece destructive physical analysis for braze and material inspection	
Two randomly selected pieces for random vibration testing	Qualification loads in a fight representative configuration
Three pieces tested on hysteresis, torsional spring rate and shear load capacity	
Two pieces life time tested for 1e5 cycles at $+/-$ 11.4° deflection	
Two pieces life time tested for 1e7 cycles at $+/-$ 6.7° deflection	

4.1.3 Control design

Mathematical modeling

A mathematical model of the mechatronic system has been identified for the development of a controller for the HIFI-FPC. Fig. 4.7 shows the mechatronic block diagram of the HIFI-FPC which contains the dynamical model of the mechanism, the power amplifiers, the LVDT pre-processing electronics, the converters and the digital controller.

The dynamics of the HIFI-FPC mechanism are described by the following differential equation:

$$(J + 2mr^2)\ddot{\theta} + 2d\dot{\theta} + 2k\theta = 2rBlI \tag{4.1}$$

where θ is the angular displacement of the mirror, I is the input current to the voice coils, J is the moment of inertia of the mirror assembly (including the two LVDT cores), m is the mass of the voice coils, r is the perpendicular distance from the center of rotation (pivot axis) to the line of action of the actuator force, d is the eddy current damping in the aluminum coil holders of the actuators, k is the spring constant of the pivots, B is the magnetic flux in the voice coils and l is the total length of the wire in the coils. We remark that the damping component is dominated by the eddy current friction in the voice coils. The mechanical friction is negligible due to the use of pivots and the lack of air friction (see also Section 4.2.2). The right hand side of 4.1 describes the voice coils torque and is proportional to the applied electrical current I.

The values for J, m, r and l in 4.1 are taken from the mechanical model of the mechanism. The spring constant has been measured for different angles @ 300 K and 4K and the magnetic

field strength is based on values supplied by the magnet manufacturer. Finally, the damping in the system has been tuned w.r.t. the open loop response of the HIFI-FPC to a step signal at a temperature of 9 K. This open loop response, together with the simulated response, is given in Fig. 4.13. The identified transfer function of the mechanism is given by 4.2 where the poles are located at -18.4 and -95.5.

$$H_{FPC}(s) = \frac{2811}{s^2 + 113.9s + 1757.2} \tag{4.2}$$

We remark that the given transfer function of the HIFI-FPC is only valid when the mechanism is operated at cryogenic temperatures. It has been observed that the dynamical behavior of the HIFI-FPC mechanism at cryogenic temperatures differs from that at room temperature. In Section 4.2.3, the effects of temperature changes on the physical characteristics of the HIFI-FPC are described.

The voice coil is driven by a current stage in order to minimize the influence of the electromotive force (emf), generated by the movement of the actuator coil, on the controller. The current stage is designed such that it has a bandwidth of 2400 Hz or 15,000 rad/s and a phase lag at 20 Hz $\leqslant 1\,\mathrm{deg}$. The resulting current stage is modeled as a second-order low-pass filter, where the input is the driving voltage and the output is the electrical current to the voice coil. Its transfer function, which is identified based on the open-loop frequency response of the current stage, is given by the following equation:

$$H_{cs}(s) = \frac{547997173}{s^2 + 10880s + 231233600} \tag{4.3}$$

The LVDT circuitry, which consists of the LVDT and the LVDT signal conditioning, is used to demodulate the LVDT signal and to filter out high frequency components. The filter is designed such that it has a cut-off frequency at 3550 rad/s. The circuit is modeled as a second-order low-pass filter which is identified using the open-loop frequency response. The transfer function of the LVDT circuit is given by the following equation:

$$H_{LVDT}(s) = \frac{5877581}{s^2 + 928s + 5597696} \tag{4.4}$$

In contrast to the HIFI-FPC mechanism, the electronics are placed outside the cryogenic chamber and they are always operated in room temperature conditions. In other words, there is no thermal effect on the electronics.

Feedback controller design

Based on the necessary exponential decay of the response to reach the 40 ms settling time requirement, the minimal bandwidth of the overall system had to be at least 20 Hz.

The bandwidth of the closed loop system without a controller installed was 17 Hz. To be able to increase the bandwidth, while keeping a stable system, phase compensation by a differentiating term was introduced. This adds phase margin to the system. A pole was added to this differentiator to limit its high frequency gain. The high requirement on the positional accuracy

(steady state error) of the mechanism required an integrator in the controller. This integrator adds a phase lag of 90 ° which had to be compensated by a second differentiating term in the controller.

For fine tuning after launch and to be able to implement different control parameters if redundancy would be lost, it was decided to utilize a digital instead of an analog controller. The sampled data controller was designed by discretizing the plant and then tuning the controller. The plant discretization was based on the step-invariant transformation method [10]. The sample frequency for the z-domain was 1.5 kHz. The final controller is a lag-lead compensator which is given by:

$$C(z) = \frac{K_1}{2}\frac{(z-a)}{(z-1)}\frac{K_2}{32}\frac{(z-b)}{(z-c)} \tag{4.5}$$

where a = 0.9863, b = 0.8643, c = 0.1455, K_1 = 18 and K_2 = 200.992.

When both components of the compensator are placed in the forward path of the closed loop system the performance is limited by the differentiating term in the second compensator. In this configuration a satisfactory settling time can be reached but the overshoot of the response is too big ($\sim$ 40%). This can be dealt with by introducing a prefilter [15] of the form given in 4.6 into the system.

$$\frac{32}{K_2}\frac{(z-c)}{(z-b)} \tag{4.6}$$

The filter eliminates the zero of the second compensator in the complementary sensitivity function while maintaining the same DC gain. The closed loop structure with the prefilter is equivalent to a structure where the second compensator term is placed in the feedback path of the control loop.

In order to deal with the saturation in the current stage, an additional anti-windup strategy [21] has been added to compensator 1. The final configuration with the two compensators is given in Fig. 4.7.

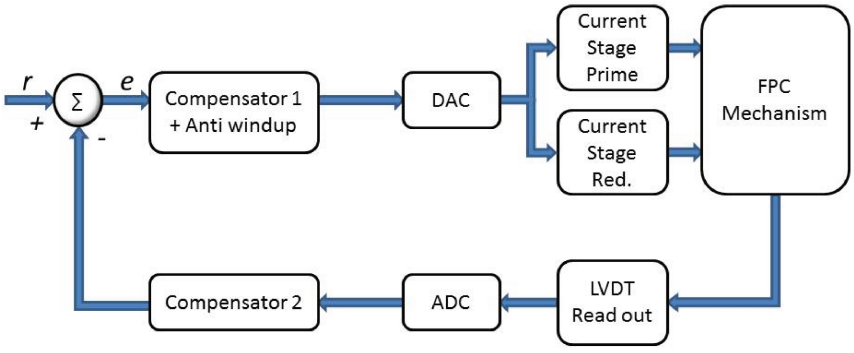

Figure 4.7: Block diagram of the closed loop chopper system showing the dynamical model of the mechanism, the power amplifiers, the LVDT pre-processing electronics, the converters and the digital controller. Anti-windup is present in Compensator 1.

To model the computational delay introduced by the quantization process, a one-step delay (z^{-1}) was added to the discrete time model.

Fig. 4.8 shows the root locus of the overall system. K_1 and K_2 are chosen such that the closedloop system has a damping ratio close to 0.5 (Q closed loop = 1/2, β = 1). The bandwidth of the overall system is 66.6 Hz which is well above the required 20 Hz bandwidth. The bode plot of the loop gain including the phase and gain margins of the system is shown in Fig. 4.9. The gain margin is 7.16 dB (at 112 Hz) and the phase margin is 34.5 (at 52.7 Hz). With these settings the system meets all its performance requirements and stability is guaranteed.

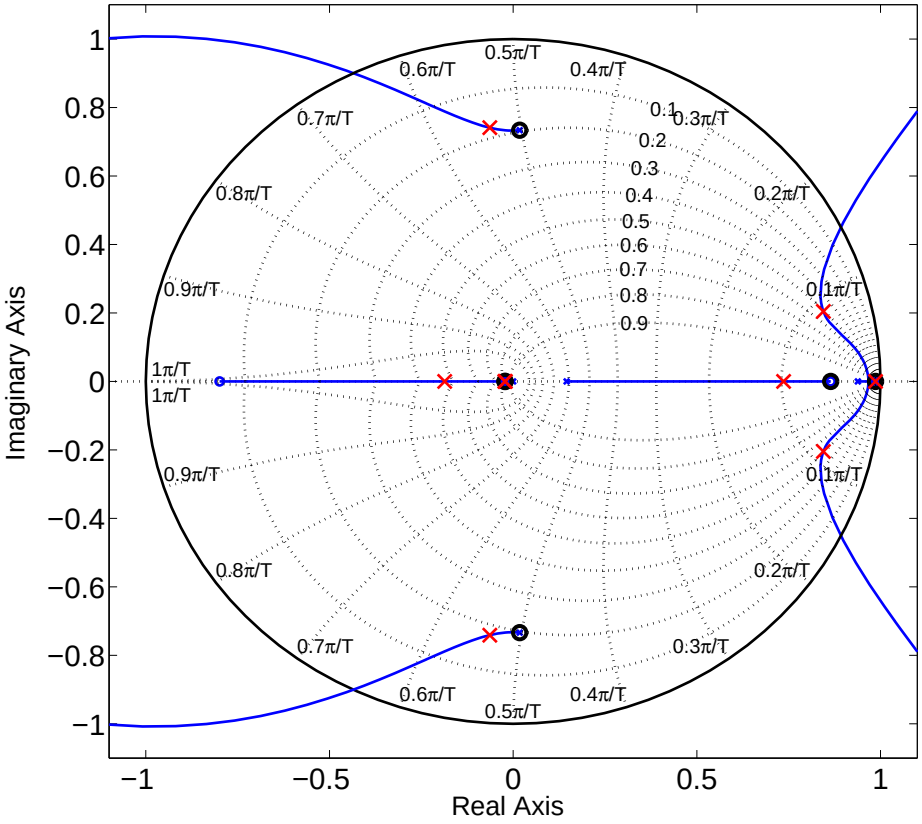

Figure 4.8: Z-domain root locus plot of the complete HIFI-FPC system including the compensator. Red crosses and black circles indicate respectively the pole and zero locations of the tuned system.

Figs. 4.10, 4.11 and 4.12 show the experimental results which characterize the static open loop response of the mechanism for nominal use (both actuators active with prime LVDT at an operating temperature of 4 K). Non-linear behavior in the HIFI-FPC mechanism is observed at the outer regions of the chopper stroke (see Fig. 4.10). This non-linearity is mainly the result

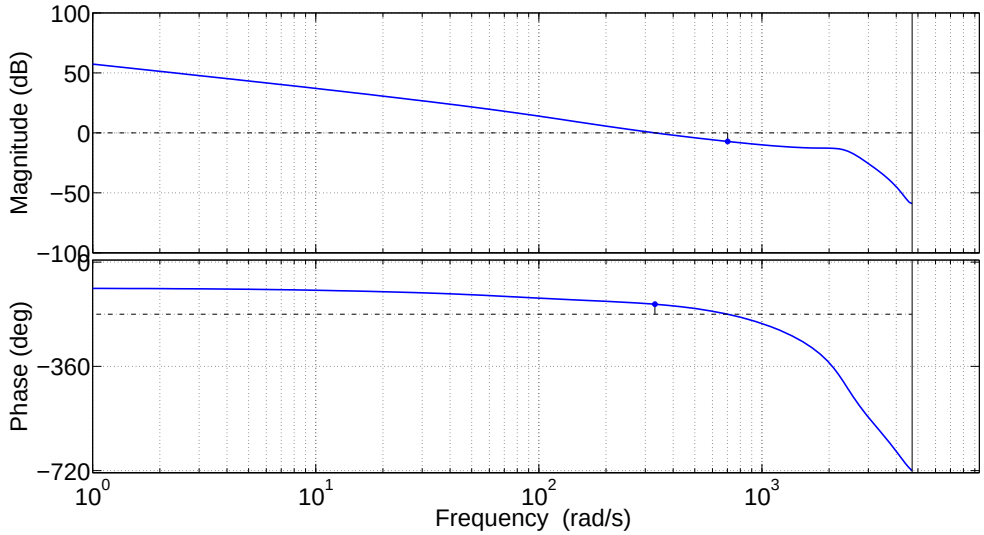

Figure 4.9: Loop gain of the final HIFI-FPC system. Gain and phase margin are indicated in the figure.

of the actuator coil partly moving outside the densest regions of the magnetic field created by the permanent magnet of the actuator when the mirror is rotated over large chop angles (see Fig. 4.11). The LVDT delivers a relatively small contribution to the total non-linearity in the response (see Fig. 4.12) and the pivot stiffness is linear over the complete chop range.

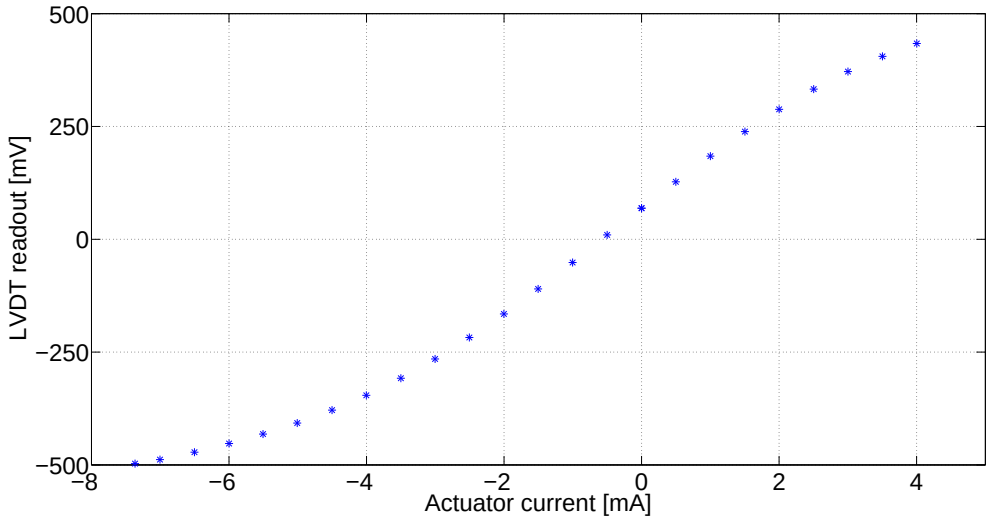

Figure 4.10: Static open loop relation between the actuator current and the LVDT readout of the HIFI-FPC.

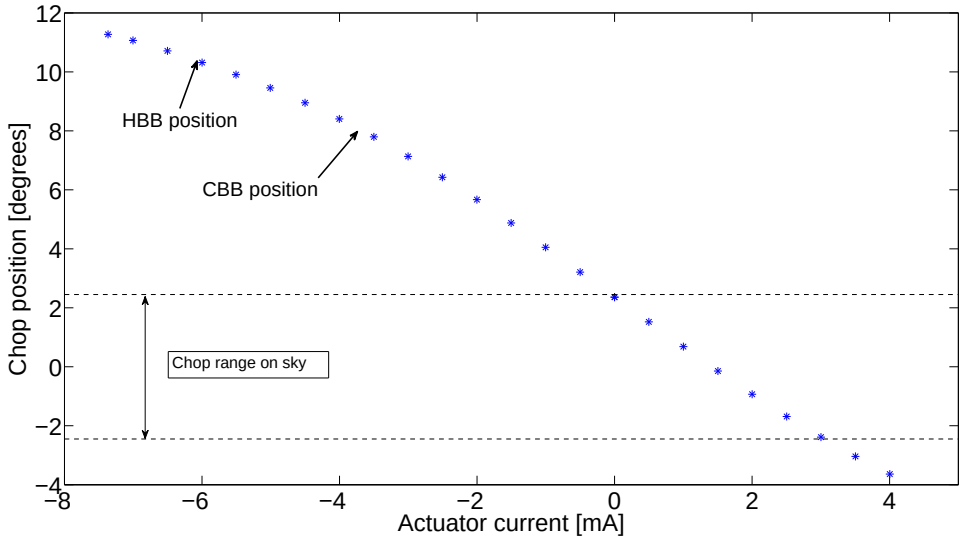

Figure 4.11: Static open loop relation between the actuator current and the chop angle of the mechanism. The on sky chop range (from -2.45° to 2.45°) and the CBB and HBB positions are indicated in the figure.

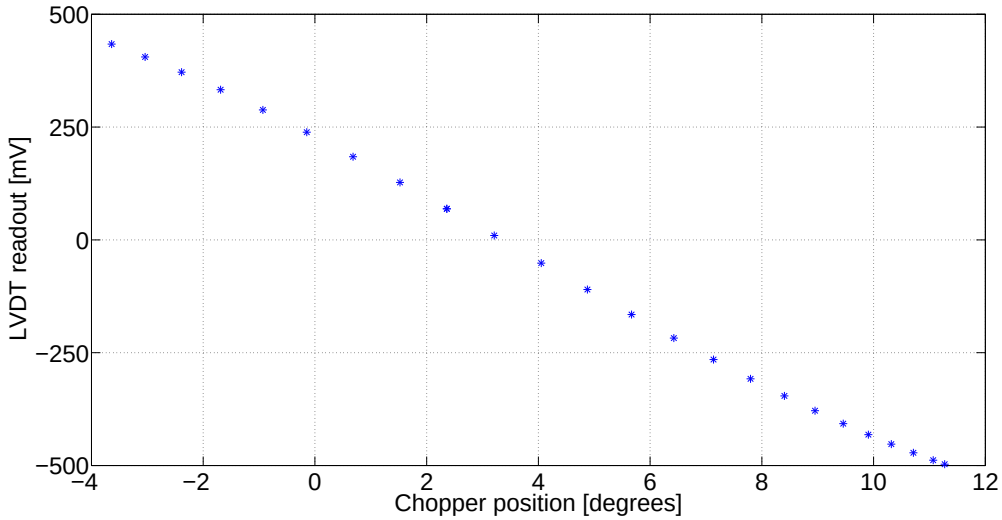

Figure 4.12: Static open loop relation between the chopper angle and the LVDT readout.

In order to deal with this problem, the controller was tuned for an optimal performance over the 4.9° chop range in which the chopper is pointing the telescope beam to the sky (see also Table 4.2). In this chop range the non-linearities are small, which makes it possible to reach the 40 ms requirement on the settling time of the mechanism. Large chop angles are required

to deflect the HIFI beam to the internal calibration sources. Despite the nonlinearity in the actuator, the controller is still able to steer the chopper to these large angles albeit with larger settling time. The chopper takes approximately 80 ms when it has to move to these positions. However, the requirements for chopping to the calibration source are less stringent and also for this mode of operation the performance stays well within the specifications.

4.2 Considerations for cryogenic HIFI-FPC design

In general the space environment is very hostile to satellites. Depending on its distance from the earth, the satellite is affected by the earths magnetic field, is subjected to extreme temperature changes and vacuum conditions, is exposed to atomic oxygen in low earth orbit, is electrostatically charged by what is left of earths atmosphere and is subjected to direct ultraviolet radiation from the sun. Furthermore, it is vulnerable to collisions with man-made space debris and is bombarded by cosmic rays, the solar wind, and micrometeoroids [64, 72].

The HIFI-FPC mechanism we are considering here is placed inside the Herschel cryostat and is well shielded from most of these influences. However, the cryogenic environment inside the cryostat itself puts various constraints on the design and testing of the mechanism. Not only the low temperature but also the vacuum conditions limit the possible design options. Here the different aspects related to the design and functioning of the HIFI-FPC in the cryogenic environment are discussed. In Section 4.2.1, the general impact of the environment on materials is described. Then, in Section 4.2.2, cryogenic design considerations applied to the HIFI-FPC and the FPU are given. Thermal issues related to the control of the mechanism are discussed in Section 4.2.3. In Section 4.2.4, we describe the difficulties involved with the testing of the mechanism in cryogenic conditions.

4.2.1 Impact of cryogenic environment on material choice

Possibly the biggest impact of the cryogenic environment on the design of the instrument is the limited choice of materials and lubricants. Some metals and most organic materials start outgassing under vacuum conditions. The evaporated material can contaminate optical components or cause problems in electrical instrumentation. Most lubricants freeze up when they are cooled down to these extreme temperatures.

The physical characteristics of common structural materials abruptly change when being cooled down below a temperature where a phase transition takes place. When the lattice of the material changes from face-centered-cubic (fcc) to body-centered-cubic (bcc), the character of the material changes from ductile to brittle. For structural components in particular, the use of brittle materials should be avoided as their strength is unpredictable.

For most materials, the strength and the resistance against fatigue increase when they are cooled down. These properties are of great importance for cryogenic mechanisms and are utilized throughout the HIFI-FPC design. Stainless steel from the 300 series possesses these properties. This is also true for Al-6061, which is used for the frame and mirror of the mechanism, and for the Inconel pivots [46].

The thermal conductivity as well as the heat capacity of the materials drops off quickly when the temperature is brought down to cryogenic temperatures. At these low temperatures

the thermal conductivity is strongly dependent on the chemical composition of the material, e.g. purity where metals are concerned [43]. This has to be taken into account when thermal cycles of the mechanism are performed (see also Section 4.2.4).

The electrical resistance of pure metals goes down with a decrease in temperature. For the copper wiring of the LVDT and the actuator coils the resistance drops off a factor of approximately 100 between room temperature and 4 K. This helps very much to reduce the operational dissipation.

In Section 4.2.2 it is explained how these considerations are taken into account in the mechanical design of the HIFI-FPC.

4.2.2 Cryogenic mechanical design of the HIFI-FPC

In Section 4.1.2 it was already stated that frictionless contacts have been chosen for all interfaces between the rigid structure and the rotatable mirror assembly of the mechanism. The relative movement of the flexural pivot cylinders is realized through the bending of the spring blades. In the LVDT, there exists no contact between the core and the coils of the system. In the actuator, the contact between the mirror and the structure of the HIFI-FPC is only through the BeCu straps. In this case, the relative movement is allowed by the bending of these straps instead of any frictional movement between the components. These design choices have been made to avoid the use of lubricants and the negative effects of hysteresis and wear in the system.

As stated in Section 4.1.2, Inconel 718 has been used as pivot material because of its favorable mechanical properties (strength and fatigue) in cryogenic conditions. Unfortunately this alloy has a poor thermal conductivity. The consequences of this design choice for the thermal behavior of the mechanism are discussed in more detail in Section 4.2.2.

Whenever stainless steel is required for structural components of the mechanism, alloys from the 300 series are to be preferred. However, the magnetic permeability of this material becomes very low at cryogenic temperatures. The magnetic permeability of stainless steel from the 400 series remains high in cryogenic conditions. Therefore, and because the mechanical loads on the LVDT are very low even during the launch of the satellite, stainless steel from the 400 series has been applied as core material and for the casing of the LVDT. This optimizes the magnetic field in the assembly and reduces stray interfering fields.

For high speed and accurate actuation, piezo actuators are often used in mechanisms. Yet, it is known that the performance of piezo actuators quickly drops when they are operated at cryogenic temperatures [44, 55]. The driving voltage of the actuator has to be increased dramatically when the actuator is used at these temperatures. This, in combination with the large required throw of the mirror makes this type of actuator unsuitable for the HIFI-FPC. The voice coil actuator is chosen because of its favorable performance characteristics in cryogenic conditions in combination with the frictionless movement between the parts.

Differences in Coefficient of Thermal Expansion

The differences in the Coefficient of Thermal Expansion (CTE) [43] of the various materials that are used in the mechanism create a real challenge for the mechanical designer of the instrument. This is particularly important during the cool down and warm up process of the mechanism, as temperature differences can easily rise above 100 K if this process is not actively controlled.

For compactly built units such as the LVDT, that contain very different materials, large internal stresses or even fracture can occur if the design does not allow for differential expansion between the parts. When a problem in the electrical circuit of such a unit arises at cryogenic conditions, troubleshooting can be very difficult as the broken interconnection may be deep inside the complex assembly and may be difficult to detect without destructive disassembly. This can lead to costly repairs and large time delays during the test program of the mechanism. To prevent this from happening the LVDT design allows for differential shrinkage between the parts.

The mirror assembly of the HIFI-FPC is thermally isolated from the frame of the mechanism. The only contact between the mirror assembly and the frame is through the spring blades of the pivots and the BeCu-straps. The thermal conductivity of the pivots is very low because of the small cross sectional area of the blades and because of the relatively low specific thermal conductivity of the Inconel. The specific thermal conductivity of the BeCu material is high but the cross sectional dimensions of the straps (thickness = 20 μm; width = 1.4 mm) are kept very small to limit their stiffness, thereby avoiding any significant influence of these components on the dynamical behavior of the mechanism. Unfortunately this also limits the thermal conductivity of these parts. Thermal strapping (i.e. creating a strong thermal link between different mechanical components by the use of a metal (typically copper or aluminum) strap) of the mirror to the structure is avoided, as this will also influence the dynamical characteristics of the system.

The thermally isolated mirror assembly can cause problems during the thermal cycling of the mechanism. During the cool down and warm up process, the differences in temperature between the HIFI-FPC frame and the mirror assembly can induce mechanical stresses in the components. This can lead to changes in the orientation of the mirror or even deformations of the structural parts, which influence the optical quality of the instrument by changing the surface quality or the alignment of the mirror.

Thermal gradients between the structure and the mirror assembly can also affect the clamping forces on the pivots. When the mirror assembly is lagging behind in temperature during the cool down process of the system, the difference in shrinkage between the mirror and the pivots reduces the clamping force on the pivots. The lower clamping force further reduces the thermal contact between both parts. In this situation the system is susceptible to changes in the mirror alignment caused by external forces on the system. The gravitational force is not big enough to cause an effect but mechanical shocks during handling of the cryostat and the forces introduced by the differences in shrinkage of the structure and the mirror assembly can change the mirror alignment.

In order to deal with these issues, the following restrictions were introduced on the thermal cycling of the mechanism: A limit of 20 K/h was set on the cool down and warm up speed of the HIFI-FPC, the allowed temperature differences between the structure and the mirror assembly were restricted to ΔT = 40 K and handling of the cryostat was prohibited during the cooling down and warming up process. Verification measurements of the alignment of the HIFI-FPC mirror were performed before and after the different thermal cycles during the qualification program of the mechanism to ascertain that the optics had remained unchanged.

The HIFI-FPC temperatures were monitored using PT1000 sensors. These are standard resistive thermal devices using platinum as the resistive component. The use of temperature sensors on the mirror assembly has been avoided because of their influence on the dynamical charac-

teristics of the mechanism (stiffness of wiring, change in moment of inertia). Instead, the ohmic resistance of the actuator coils was measured during the thermal cycles. As the temperature dependence of the resistance of the coil wiring was known, this gave a rough but sufficient value for the temperature of the mirror assembly.

Thermal mechanical design verification of the HIFI-FPC

During the design phase of the mechanism, thermal-mechanical calculations in steady state conditions @ 4K have been performed to determine the effect of the differences in CTE of the materials on the mechanical integrity of the mechanism, the heat dissipation and the to be expected temperature differences in the instrument during operations. The knowledge about the thermal properties of the different materials is based on the given references complemented by lab experiments of the thermal conductivity of aluminum and copper and that of different thermal contacts.

For complex assemblies, like the actuators and LVDTs, the reliability of the thermal calculations is limited because of insufficient knowledge about some of the parameters involved (for example the thermal contact resistance between the coils and the structure is not accurately known). To get a complete overview of the effects of the cryogenic environment on the mechanism, the HIFI-FPC was subjected to an elaborate test program (see Section 4.2.4).

Transient analysis of the thermal effects on the mechanism is not required because of the steady state conditions in which the operation of the mechanism takes place. The potentially large temperature differences during the cool down and warm up of the mechanism are limited by actively controlling this process.

General mechanical thermal design solutions implemented in HIFI

For completeness, the general thermal design considerations that were applied in the HIFI FPU are shortly discussed in this subsection.

Thermal strapping is needed to keep the detectors at the required operating temperature of 2 K leaving the rest of the HIFI instrument at 15 K. For the thermal strapping of the instrument, high purity (99.999%) aluminum has been used. The specific thermal conductivity of this material is comparable to that of high purity copper which is often used for thermal strapping. The match in CTE with respect to the aluminum structure (type: Aluminum-6061) clearly benefits the mechanical design of the instrument.

The thermal contacts at interface points of the strapping have been optimized by creating large contact areas. In most cases bolted interfaces are required but for permanent connections solder joints have been used to further optimize the thermal conductivity of the strapping. Castolin 190 NH, which is an aluminum/silicon solder, was used for this purpose. Castolin 190 FL was used as flux material. The thermal conductivity of these contacts and their suitability for use in the cryogenic environment have been studied at an early stage in the project in a separate development test program. The results of these tests show an increase in thermal conductivity w.r.t. the bolted connection. These observations are confirmed by the literature [22]. No degradation of the contacts was observed during the development test program or during the extensive qualification program of the HIFI FPU.

For the structural support of the strapping, Vespel has been used. This material combines low thermal conductivity with ample mechanical strength. For thermal isolation of the HIFI detectors from the main structure, stainless steel tubes from the 300 series, with a diameter of 1.5 mm and a wall thickness of only 50 μm have been used. The relatively low thermal conductivity (in comparison with other metals) of the stainless steel in combination with its high strength makes it another good candidate whenever thermal isolation and structural support have to be combined.

4.2.3 Thermal issues in control design of the HIFI-FPC

Influences of temperature changes on open loop step response

Temperature changes can alter the physical characteristics of the mechatronic system which can in turn influence the performance of the mechanism. In Fig. 4.13 the open loop step response of the chopper at room temperature and at a temperature of 4 K are given. The differences in the response are caused by the differences in the eddy current damping in the aluminum coil holder of the actuators. This parameter becomes approximately 2.5 times bigger when going from ambient to cryogenic conditions. This has to be taken into account in the design and test program of the mechanism. A separate set of control parameters are used for the closed loop control at ambient and at cryogenic conditions.

Not only temperature changes in the mechanism but also in the harness and electronics of the system can be of importance. In Section 4.2.3 the influences of temperature variations on the LVDT response is discussed.

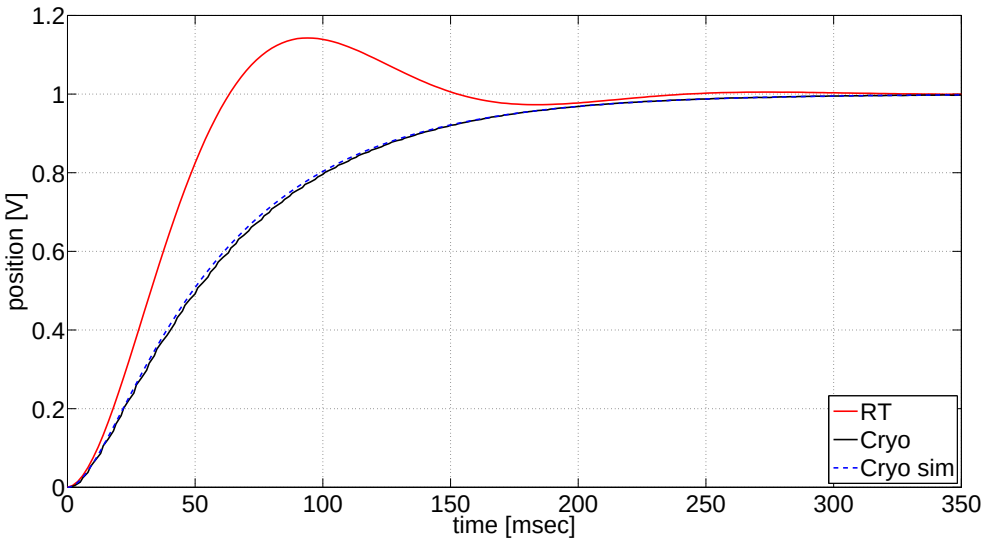

Figure 4.13: HIFI-FPC open loop step response at room temperature (293 K) and at 4K. Also showing the simulation result (blue dotted line).

Influences of temperature changes on LVDT response

The bode plot of the response for the original 10 kHz LVDT circuit design is given in Fig. 4.14. The frequency response of the LVDT circuitry has a resonance peak at approximately 15 kHz. In principle, the positional resolution of the LVDT will increase when a higher carrier frequency is used. However, when the carrier frequency of the LVDT is chosen too close to the resonance frequency of the system, small changes in the position and shape of the resonance peak, caused by thermal variations in the LVDT circuitry, strongly affect the coupling of the prime carrier signal to the secondary LVDT coils.

This problem was encountered during the test phase of the mechanism, where temperature changes in the five meter long harness of the HIFI-FPC, produced small changes in the harness resistance and the capacitive coupling between the different wires. As the harness is part of the electrical circuitry of the LVDT, these minor changes in the electrical characteristics of the wiring caused a shift in the location of the resonance peak. This produced a non-negligible change in the response of the LVDT. The problem was tackled by reducing the LVDT carrier frequency from 10 kHz to 2.6 kHz.

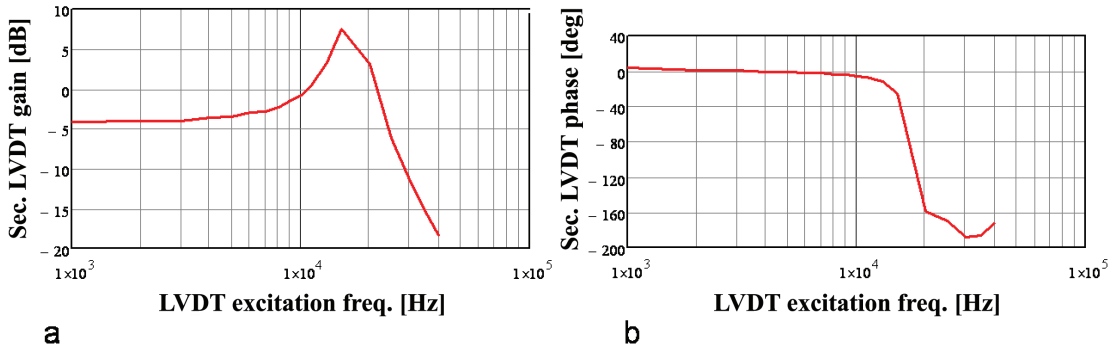

Figure 4.14: a: Magnitude plot of the original 10 kHz design LVDT response. b: Phase plot of the original 10 kHz design LVDT response.

Thermal design versus dynamical characteristics

In some cases there is a conflict between a good thermal design of the mechanism and the design considerations with respect to the dynamical characteristics of the unit. For example, the choice of placing the actuator coils on the mirror assembly of the HIFI-FPC, rather than the heavy magnet casing, has a clear advantage with respect to the control of the mechanism because it reduces the moment of inertia. However, the thermal effects are negative as the heat generated by the coils is collected by the thermally isolated mirror assembly. The CAD model of the mechanism indicated that the inertia of the mirror assembly could be reduced by more than a factor of three when placing the coils on the moveable part of the mechanism. A worst case estimate of the temperature rise in the mirror assembly, as a result of the heat dissipation in the coils, showed that this would be limited to five degrees. Comparing these results with the requirements of the mechanism, the choice was made to place the coils on the mirror assembly

to optimize performance without jeopardizing the structural integrity of the mechanism.

Another example is the use of flexural pivots (no friction, low hysteresis) and the absence of thermal strapping attached to the mirror assembly. This makes the system suitable for control but limits the ability to get rid of the developed heat in the actuator coils. From the perspective of thermal stability and the thermal budget, the maximum heat dissipation by the actuators should be limited. This of course also limits the available power to control the mechanism.

There are no clear design criteria to deal with these conflicting requirements. For every new case an optimal balance has to be found between the different aspects of the design. For the HIFI-FPC, analysis tools like for example Matlab-Simulink, Finite Element Methods (FEM) and MathCad have been used to optimize the design. The quality of the design has been verified in an elaborate test program in which all functional and performance requirements have been tested.

4.2.4 Cryogenic testing

From the preceding sections it is clear that a detailed understanding of the temperature dependent behavior of the mechanism is of crucial importance in order to develop a reliable and well performing mechanism, and although the engineer can make use of different design tools and the available knowledge about the temperature dependent properties of the materials used, an elaborate test program is thought to be absolutely essential to verify the cryogenic compatibility of the design.

An important part of the qualification test program for the HIFI-FPC consisted out of the thermal cycles to cryogenic temperatures. The mechanism first was cooled ten times to a temperature of 4K and after this, another six times to a temperature of 77 K. During this program different tests were performed in ambient and cryogenic conditions to verify the structural integrity of the mechanism.

Test campaigns can take a lot of time as the cooling down as well as the warming up of the test setup should be executed in a well-controlled manner avoiding large temperature differences in the setup (see also Section 4.2.2).

Designing a good setup for testing in cryogenic conditions is not a trivial task. In Section 4.2.4, the considerations for the design of the HIFI-FPC test setup are described.

It is not always necessary to perform the tests at cryogenic conditions. In Section 4.2.1 it has been described that in general the strength and material resistance to fatigue become better when the material is cooled down. This was of great use for the extensive lifetime test program of the pivots. Although the better fatigue properties are partly canceled by the increase in internal stresses in the material with the same angular deflection at cryogenic conditions, lifetime testing at ambient conditions could be considered as worst case. This justified a pivot lifetime test program at ambient conditions which greatly simplified the test setup and thereby the reliability of the measurements.

Test setup

For the test program of the HIFI-FPC we used a cryostat to create a test environment at stable temperatures of 77 K and 4 K. The closed cryostat is provided with a window which allows optical tests to be performed on the HIFI-FPC mirror surface in cryogenic conditions.

As already mentioned in Section 4.2.1, in cryogenic conditions the specific heat capacity of the materials used is very low. Therefore, the thermal balance is easily influenced by power dissipation in the components, parasitic heat input through the harness of the test setup and radiative heat input through the windows in the cryostat vessel. Temperature measurements can be affected by radiative heat input on the temperature sensors and parasitic heat input via the wiring of the sensors.

Using adequate radiative shielding of the sensors and using baffles around the cryostat windows one can limit the influence of radiative heat input. For the wiring an optimal balance between the thermal conductance of the cabling and the heat dissipation developed in the wiring has to be found. For the HIFI-FPC test setup manganin wiring has been used. The thermal conductivity of this material is low and, although the impedance of the wiring is relatively high, the heat dissipation is limited because the currents running in the system are reasonably low. To further reduce the parasitic heat input by the wiring, heat sinks to intermediate temperature stages have been used.

4.3 HIFI-FPC performance

The final performance of the HIFI-FPC flight model has been determined in the lab before integration of the mechanism with the HIFI instrument. The test results are summarized in the third column of Table 4.1. The requirements are given in the second column of the same table. It can be seen that all performance requirements are met.

After the launch of the satellite, a health check of the HIFI-FPC has been performed in which the structural integrity and the dynamical behavior of the unit have been checked. No anomalies where found in this test. Fig. 4.15 shows the closed loop step response of the mechanism after launch.

The response of the chopper has evidently not changed as a result of the launch or because of the small differences in operating temperature (9 K lab environment w.r.t. 15 K space conditions). Therefore it has not been necessary to change the digital control parameters, a contingency that had been built into the satellite operational system.

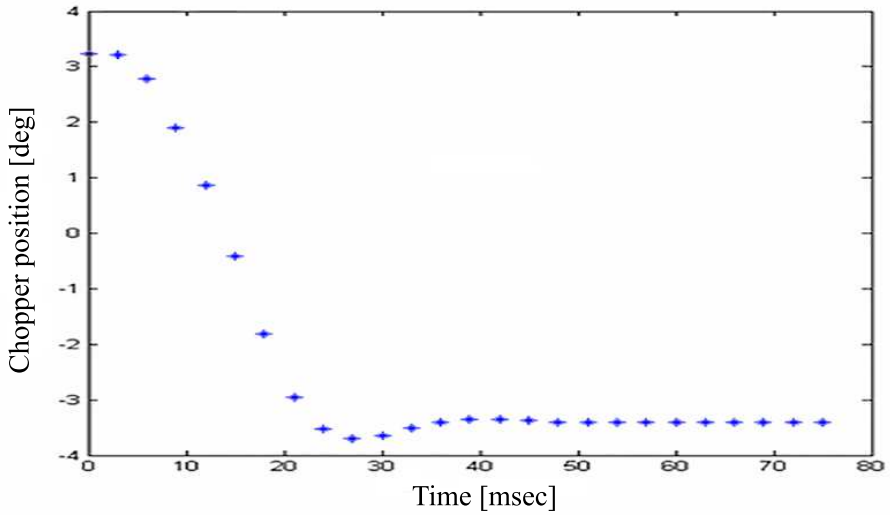

Figure 4.15: Closed loop step response of HIFI-FPC mechanism in space. Measurement performed every 3 ms.

4.4 Concluding remarks

In this chapter, thermal issues that were important for the design and development of the HIFI-FPC and which can be relevant for the development of future mechatronic systems in cryogenic conditions have been discussed.

In general, the choice of material is critical and the use of lubricants should be avoided if possible. Material properties can vary considerably in the temperature range from ambient to cryogenic temperatures. The control strategy has to be insensitive to changes in the physical parameters as a result of thermal variations in the system.

The HIFI-FPC is performing well within the defined requirements for the mechanism. However, with respect to the settling time, the margins between the performance and the requirements are only small.

The general demand for more stringent performance requirements and in most cases the increase in complexity of chopper mechanisms, ask for further optimization of the mechatronic design of the instruments where all aspects of the system should be developed in parallel in an integrated design approach [2, 68].

It should be clear that thermal issues play an important role in the final performance of the mechanism and should be taken into account during the design and test program of the instrument.

Considering the different building blocks of mechatronics (mechanics, electronics, computer systems and control) and the discussed hardware limitations which are imposed by the cryogenic environment, we believe that the biggest progress can be made by the application and further development of advanced control strategies for these mechanisms.

Chapter 5

Synthesis and application of hybrid controller to HIFI-FPC

In this chapter, we evaluate the efficacy of our proposed control strategy using an exact copy of the HIFI-FPC. We compare our results with those using the original controller of the HIFI-FPC described in 4.1.3.

In the experiment we considered square wave chopping, which is the standard mode of operation for the HIFI-FPC. As we would also like to verify performance for 2 DoF observation modes, we show the results of an OTF observation by simulation, using a virtual 2 DoF HIFI-FPC mechanism.

As discussed in Section 3.3, the feedforward stepping input for both observation modes is calculated off-line, by the method described in Section 3.5, and applied after every tracking period.

Section 5.1 describes the system identification of the HIFI-FPC. In Section 5.2 we apply the hybrid controller to the hardware. The simulation results for 2D OTF scanning using the HIFI-FPC are given in Section 5.3. The results are discussed in 5.4. The test setup used in the experiments is described in Appendix A.

The results in this chapter are published in [30].

5.1 System identification

Based on the step response of the mechanism, the state space description of the combined amplifier, plant and sensor was deduced using the system identification toolbox in Matlab. The high sensor and amplifier bandwidth, w.r.t. the plant dynamics, allows us to model the plant as a second-order system, treating the amplifier and sensor as a pure gain in the system. The state space description of the mechanism is then given by

$$\begin{bmatrix} \dot{x}_1 \\ \dot{x}_2 \end{bmatrix} = \begin{bmatrix} 0 & 1 \\ -1553.6 & -115.3 \end{bmatrix} \begin{bmatrix} x_1 \\ x_2 \end{bmatrix} + \begin{bmatrix} 0 \\ 2849 \end{bmatrix} u$$

$$y = \begin{bmatrix} 1 & 0 \end{bmatrix} \begin{bmatrix} x_1 \\ x_2 \end{bmatrix}$$

The plant input u is constraint to $\{u \in U : |u| \leqslant 23.7\text{mA}\}$. The small differences in the dynamics of this characterization and the model of the system described in 4.2 can be explained by the different choppers used (flight hardware vs spare model). The gain difference is caused by the differences in amplifiers.

5.2 Experimental results for square wave chopping

The square wave reference profile is illustrated in Fig. 5.1. It is jumping between two stable positions α_1 and α_2 with a period T and describes a hybrid arc on the hybrid time domain.

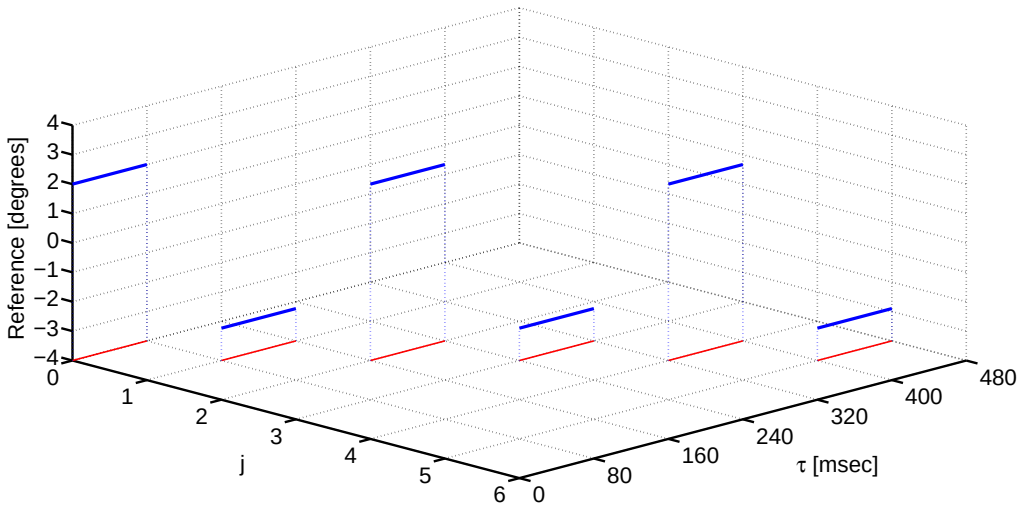

Figure 5.1: 1 DoF Square wave chopping reference signal (blue) on hybrid time domain E (red).

We perform a chop sequence with constant observation positions $\alpha_1 = 2$ and $\alpha_2 = -2.9$ degrees. For square wave chopping the initial state of the exosystem is given by

$$w(0,0) = \begin{bmatrix} 0 & 0 & \alpha_1 & 0 & 0 & 0 & \alpha_2 & 0 \end{bmatrix}^T.$$

We apply a hybrid PI controller, which was tuned using Matlabs sisotoolbox. With only the two control states related to the integrator active, the matrices of the hybrid controller given in (3.6) can be written in the following compact form

$$\begin{aligned} A_C &= \begin{bmatrix} 0 & 0 \\ 0 & 0 \end{bmatrix} \; B_C = \begin{bmatrix} k_i \\ 0 \end{bmatrix} \; C_C = \begin{bmatrix} 1 & 0 \end{bmatrix} \; D_C = k_p \\ \Phi &= \begin{bmatrix} 0 & 1 \\ 1 & 0 \end{bmatrix} \; \Psi = \begin{bmatrix} 0 \\ 0 \end{bmatrix}, \end{aligned} \tag{5.1}$$

where $k_i = 7 \times 10^{-3}$ and $k_p = 0.5$ are respectively the integrator and proportional gain.

With every jump the integrator and memory state exchange values. In this way, for both reference positions, the integrator state quickly converges to its required value where it stays during the rest of the chopping sequence. During the jump, the open loop control input rotates the mirror to its new observation position. Applying this controller, γ in (3.4.1) can be computed to be 0.99994 which proves that output regulation for this system is satisfied.

The experimental results are shown in Fig. 5.2 and 5.3. The vertical dotted lines indicate the moment of switching between the open loop and closed loop controller. The close up in Fig. 5.3 clearly shows the difference in settling time between the two controllers.

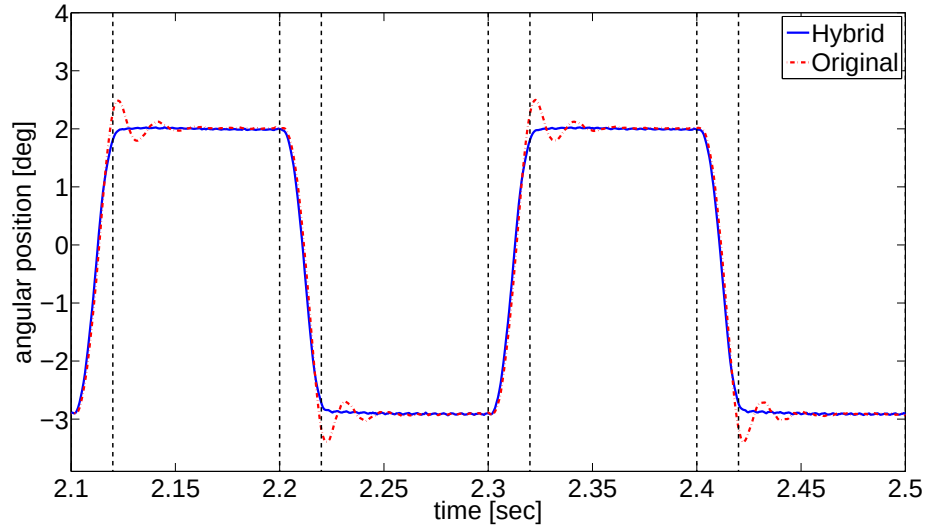

Figure 5.2: Experimental result for HIFI-FPC square wave chopping with hybrid controller. The result when applying the original controller is included for comparison. The vertical dotted lines indicate the start and end points of the jump and flow intervals

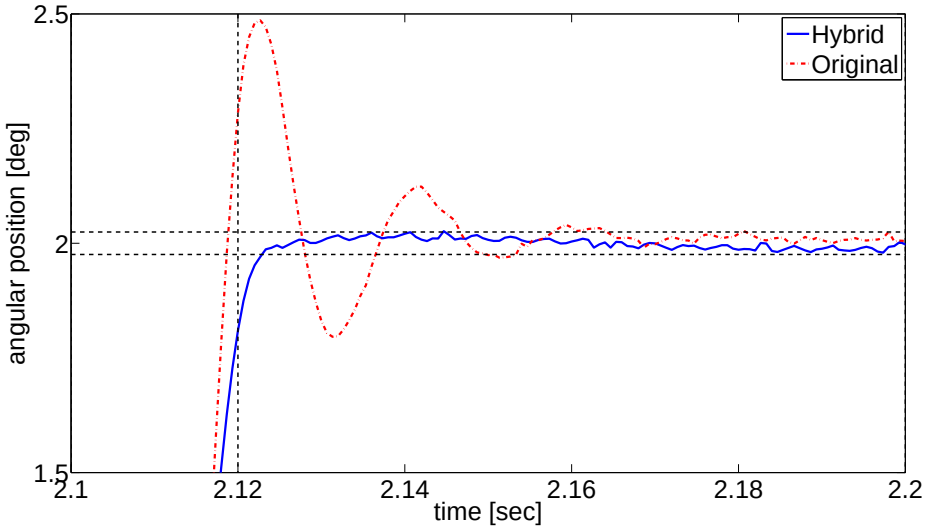

Figure 5.3: Close up at the 2 degrees observation position. The figure clearly shows the improved settling behaviour when applying the hybrid controller

Table 5.1 summarizes the results for chopping using the original and the new chop strategy for different settling time criteria. The results for the 0.5% criterion are directly applicable to the HIFI-FPC requirements. The 38 msec of the original controller can not be reproduced with this setup. However, the results for both controllers are produced using the same setup and can therefore be compared.

Table 5.1: Step response and overshoot for square wave chopping when applying the original and hybrid controller to the HIFI-FPC

	Original controller	**Hybrid controller**
% overshoot	10%	0%
0.5% settling	49 ms	31 ms
1% settling	47 ms	24 ms
2% settling	43 ms	21 ms

5.3 Simulation of OTF observation

The OTF reference (Fig. 5.4) is given for both DoF's seperately on the hybrid time domain. It executes a linear motion in the 1^{st} DoF where the sign of the motion changes with every scan, and jumps between different stable positions for the 2^{nd} DoF.

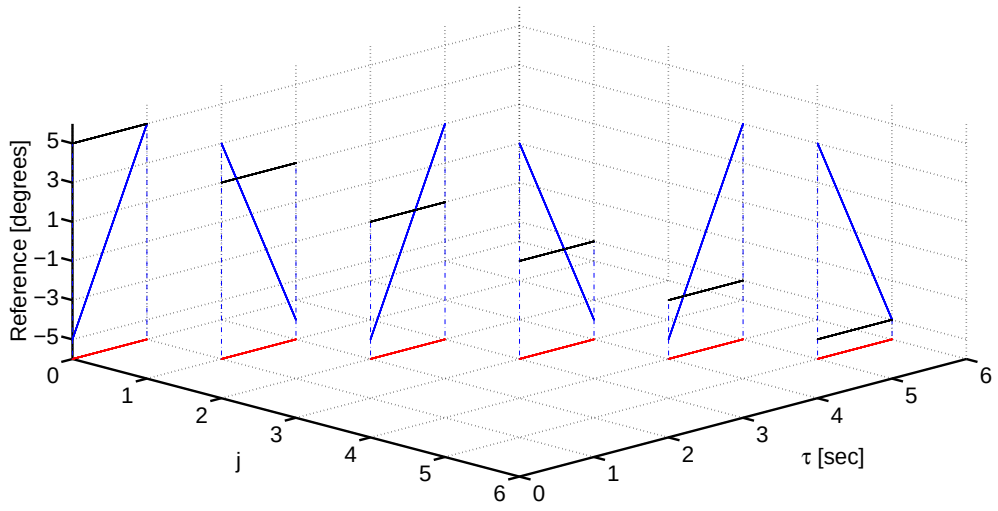

Figure 5.4: 2 DoF OTF reference signal (Blue: 1^{st} DoF; Black: 2^{nd} DoF) on hybrid time domain E (red). NB: The hybrid arc for both DoF's is plotted in one figure.

The OTF observation starts at an offset position of $[-5, +5]$ degrees. It runs over a square array of 10 by 10 degrees with a constant velocity of 10 deg/s in DoF 1 during flow, and jumps over an angle of -2 degrees in DoF 2 after every scan period. $t_{obs} = 1$ sec and $t_s = 40$ msec.

The description of the complete initial state of the exosystem is omitted for reasons of space but can be constructed from Table 3.1 with $q = 6$, $\alpha_{1...6} = [-5, 5, -5, 5, -5, 5]$, $\dot{\alpha}_{1...6} = [10, -10, 10, -10, 10, -10]$ and $\beta_{1...6} = [5, 3, 1, -1, -3, -5]$. We apply the hybrid controller given in (3.6) with $k_1 = 0$, $k_2 = 7$, $k_3 = 20$, $k_4 = 0$, $k_5 = k_2$ and $k_6 = 0$. As we only require a proportional term for error convergence, the $*$ in all control matrices except for D_c are replaced with zeros. D_c forms a 2 by 2 diagonal matrix with $k_p = 0.5$ on the diagonal. For this system $\gamma = 0.52498$.

Fig. 5.5 shows the simulation result of the OTF observation. The complete observation profile is executed 3 times. With every cycle the trajectory converges further to the steady state, which accurately follows the reference profile. This is illustrated in Fig. 5.6 where the error convergence is plotted on the hybrid time domain. In Fig. 5.7 a close up of the error after convergence is shown. The result when applying the original controller is also given. The small error that is left after convergence when applying the hybrid controller is caused by the limitations of the feedforward input.

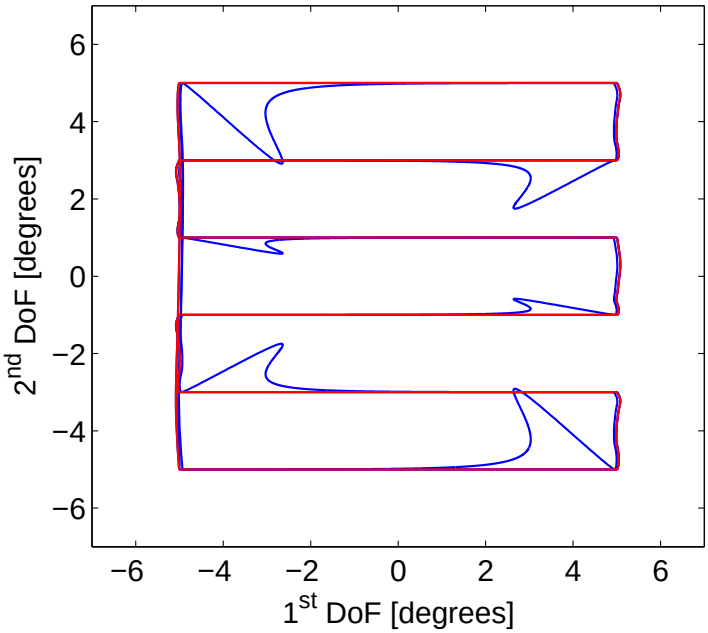

Figure 5.5: Simulation of response of hybrid system to the OTF reference profile (blue line). Red line gives the result after convergence (3^{th} iteration).

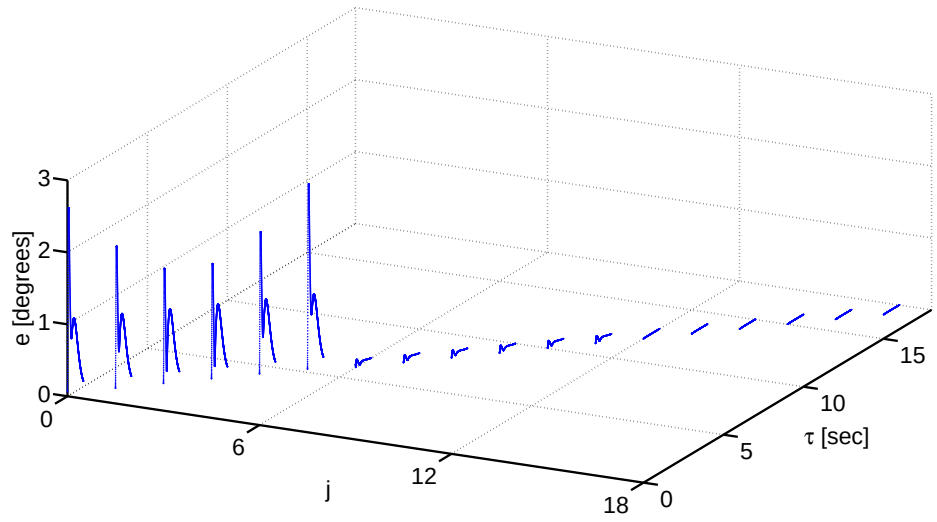

Figure 5.6: Error convergence (formulated as the euclidean norm of the error $\|e\|_2 = ({e_1}^2 + {e_2}^2)^{1/2}$) on hybrid time domain during simulation of OTF observation. The 6 flow trajectories in 1 OTF scan converge with every repetition of the complete OTF profile.

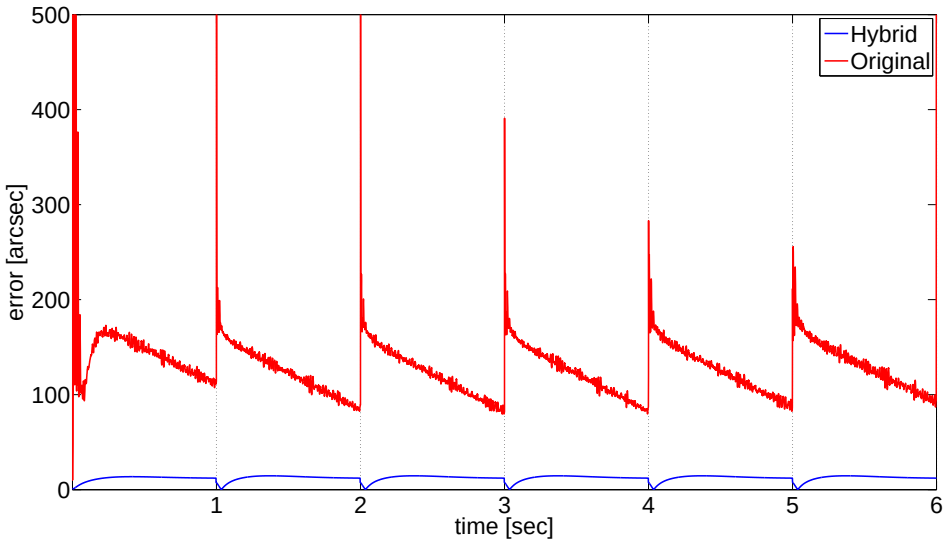

Figure 5.7: Error of OTF observation after convergence when applying hybrid controller (blue). NB: for comparison the result when applying the standard controller (red) is also given, leaving out the data points related to the ”jump” between the different linear scans. The vertical dotted lines indicate the jumps of the system.

5.4 Concluding remarks

We tested the hybrid control strategy on an exact copy (spare flight model) of the HIFI-FPC, and compared the results to those when applying the standard controller. The results show an improvement in settling time of 37%.

These tests where performed before finalization of the MCCD hardware, however to gain early insights in the performance of the controller for 2D scan profiles, we simulated the response of a 2D HIFI-FPC mechanism to an OTF reference profile. As expected from the calculated value of γ, the controller stabilizes the plant and again shows a large improvement in tracking w.r.t. the original controller.

These results support the ideas stated in Section 4.4 about the application of advanced control strategies for chopper mechanisms.

Chapter 6

High performance motion control of the METIS Cold Chopper Mechanism

The MCCD, which has been introduced in Section 1.3.2, forms a new challenge in the development of cryogenic chopper mechanisms. Its requirements on positional stability, repeatability and settling time for 2D movement profiles in a cryogenic operational environment are extreme. Compared to the HIFI-FPC, which already provided us with a number of challenges during its development, these requirements are orders of magnitude (a factor 86 for positional stability, a factor 257 for repeatability and a factor 8 for settling time) more demanding.

These extreme requirements have resulted in a novel mechatronic design, implementing interferometric position sensors with extremely high positional resolution and low noise levels and a redesign of the actuators to reduce the moving mass and optimize the force constant. This had to be done while taking into account the cryogenic design and test limitations which have been discussed in Chapter 4.

In this chapter we describe the design, control synthesis and performance of the MCCD mechanism. In Section 6.1 we start by presenting the cryogenic mechatronic design of the MCCD and discuss the critical mechatronic components. In Section 6.2 we describe in detail the system identification of the hardware which revealed the presence of hysteresis in the system. We discuss how the hysteresis limits the model accuracy of the plant. The results when incorporating hysteresis in the plant model are presented and the effect of the hysteresis on the performance of both the hybrid controller and a repetitive controller are discussed. The synthesis of these control strategies with the MCCD mechanism is described in Section 6.3. The performance of the mechanism is presented in Section 6.4. Most requirements can be satisfied when applying the repetitive controller to the current hardware. Suggestions to solve the final issues with positional stability and settling time are provided, to be able to meet all stringent requirements for the final MCC mechanism on the METIS platform. We discuss the practicle implementation of the repetitive control strategy in Section 6.5. Finally, the conclusions about this experimental phase are presented in 6.6.

The results in this chapter are published in [29] and [52].

6.1 MCCD mechanism description

The MCCD mechanism is shown in Fig. 6.1. The heart of the MCCD design is its aluminum mirror with an outer diameter of 64 mm and inner diameter of 21 mm. This mirror is constraint in three DOFs (x, y, θ_z) by a stiff support and the remaining three DOFs, the angular position and focus, are controlled using three linear actuators and three linear position sensors. Fig. 6.2 defines the coordinate system and the location of the actuators and sensors. The basic concept

behind this design is depicted in Fig. 6.3. In the MCCD the actuator forces are not directly applied to the mirror. Instead, the forces act on an intermediate body to which the mirror is connected by means of a leaf springs suspension. This stress free support precisely constrains the six DOFs of the mirror and minimizes the impact of intermediate body deformations on the mirror surface accuracy.

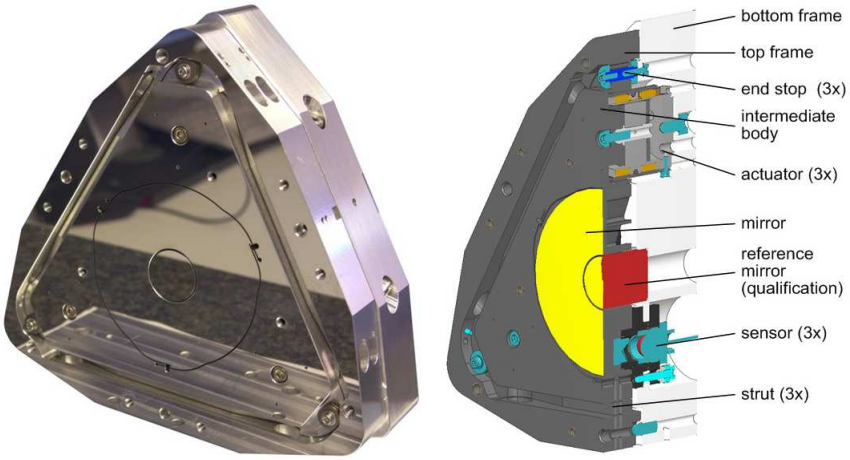

Figure 6.1: Left: Photo of the MCCD mechanism. Right: Cross-section of the MCCD along the x-axis. The critical components are indicated in the figure. Design by Janssen Precision Engineering (JPE)

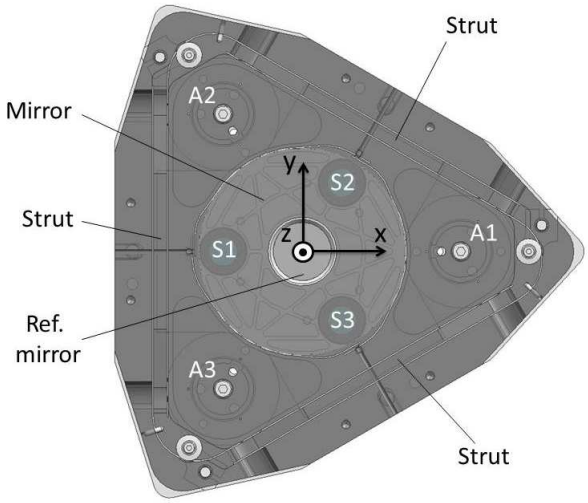

Figure 6.2: Schematic drawing of the MCCD mechanism. Triangular support structure with circular mirror body is made transparent to show the location of the sensors (S1, S2 and S3) and actuators (A1, A2 and A3). Coordinate system is also indicated.

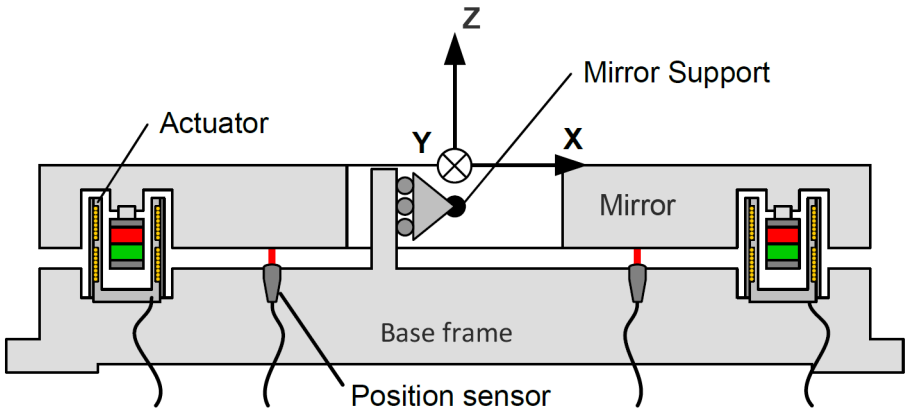

Figure 6.3: Conceptual drawing of the MCCD showing the mirror support (which defines its DoFs) and the distribution of the VCA's and the position sensors (not on scale).

As discussed, the feedforward path of the position controller relies on the reproducibility of the mechanism and its movements. Therefore, friction and backlash had to be eliminated by connecting the intermediate body to the top frame using a fully flexible suspension consisting of three struts each constraining one DOF. The elastic hinges of these struts were designed to keep the maximal stress over the complete operating range below the fatigue limit of the used aluminum (96 MPa at 108 cycles). Top frame, intermediate body, mirror, and suspensions are implemented as one monolithically integrated component and manufactured from a single piece of T6061-T6 aluminum. To limit the acceleration forces and resulting power consumption the moving parts were light weighted, but without sacrificing overall dynamic characteristics of the mechanism (e.g. stiffness/resonance frequencies).

The base frame consists of two parts, the already discussed top frame and the bottom frame on which the position sensors, the end stops, and the stator of the actuators are mounted. Together these components form the stationary part of the chopper (base frame in Fig. 6.3). Of these components, the actuators and sensors, discussed in respectively 6.1.1 and 6.1.2, are critical for the performance while the end stops are only there for emergencies. For instance during an earthquake or when the chopper mechanics or electronics fail. At these occasions, the built-in flexibility of the end stops limits the deceleration forces on the intermediate body and stresses in the mirror suspension.

The mechanism dynamics (inertia, spring constant and damping) are designed to be rotationally symmetric. The multiple-input multiple-output (MIMO) system is converted to three decoupled single-input single-output (SISO) systems by applying the following matrix transformations.

$$\begin{bmatrix} z \\ \theta_x \\ \theta_y \end{bmatrix} = \begin{bmatrix} \frac{1}{3} & \frac{1}{3} & \frac{1}{3} \\ 0 & \frac{1}{\sqrt{3}r_s} & -\frac{1}{\sqrt{3}r_s} \\ \frac{2}{3r_s} & -\frac{1}{3r_s} & -\frac{1}{3r_s} \end{bmatrix} \begin{bmatrix} z_1 \\ z_2 \\ z_3 \end{bmatrix} \tag{6.1}$$

$$\begin{bmatrix} F_1 \\ F_2 \\ F_3 \end{bmatrix} = \begin{bmatrix} \frac{1}{3} & 0 & \frac{-2}{3r_f} \\ \frac{1}{3} & \frac{1}{\sqrt{3}r_f} & \frac{1}{3r_f} \\ \frac{1}{3} & \frac{-1}{\sqrt{3}r_f} & \frac{1}{3r_f} \end{bmatrix} \begin{bmatrix} F_z \\ M_{\theta_x} \\ M_{\theta_y} \end{bmatrix} \tag{6.2}$$

(6.1) relates the three sensor readouts (z_1, z_2 and z_3) to the three DoF's of the system, where r_s is the radial distance of the sensors to the heart of the mirror. (6.2) converts the control inputs (F_z, M_{θ_x} and M_{θ_y}) for the different DoF's, to the individual force inputs (F_1, F_2 and F_3) of the actuators. Here r_f is the radial distance of the actuators to the heart of the mirror.

6.1.1 Voice coil actuators

Although Voice Coil Actuators (VCAs) are commonly available the ones employed in the MCCD are custom designed and made to satisfy the specific constraints of the low temperature and, to a lesser degree, the vacuum environment. In this custom design, the coils are fixed to the stationary part of the chopper while the permanent magnet assemblies are connected to the moving intermediate body. By making the coils part of the stator a large thermal load is avoided as their heat is directly transferred to the frame and not to the intermediate body. An additional advantage of this configuration is that the lead wires are stationary, thus avoiding fatigue issues.

Unlike in conventional VCAs the back iron is not directly attached to the permanent magnet assembly. Instead it is mounted to the stationary coil holder to reduce the moving mass. As a result the magnetic field in the back iron moves with the movement of the chopper and this introduces both magnetic stiffness and hysteresis. The effect this has on performance is discussed in Section 6.2.3.

6.1.2 Position sensors

Position measurement is provided by a commercially available three axis interferometer system. All the active components of this system are in the ambient environment as the laser source and the detector are fiber-coupled to the sensor head. Hence, for cryogenic compatibility the only issue which has to be addressed is the large difference in CTE between the titanium sensor head and the aluminum bottom frame. This has been solved by mounting the sensor in a titanium bush and bolting this bush to frame using stainless steel bolts and aluminum CTE compensation spacers. These bushes also help to suppress stray light coming from the sensor head or the target by means of an integrated labyrinth.

Because the sensor system cannot handle large angles when combined with a flat target, i.e. small mirror on the back of the main mirror, the sensor is aimed at hollow retro-reflectors. These (off-the-shelve) retro-reflectors guarantee that sufficient optical power is reflected back into the fibers even at large tip/tilt angles. At these angles the noise-level is increased, when the laser beam comes close to the apex of the retro-reflectors, and in the breadboards test the specification was not met (<30 nm peak-peak). Fortunately, the sensor drift was well below its specification allowing a re-budgeting of the contribution of each disturbance source to the overall stability. Therefore, the sensor noise specifications was increased to 30 nm (3σ) and this is met by moving the sensor heads with respect to the apex.

6.2 System identification

6.2.1 Sensors and actuator characteristics

One of the first steps after the realization and integration phase was to verify the correct operation of the position sensors. This has been done by pulling the intermediate body against the end stops in eight different configurations (three end stops on two sides). In each position the three sigma noise level has been determined and found to be always below the specified 30 nm. Next, the accuracy of the sensors has been verified by comparing the angle calculated from the sensor signals with theodolite measurements. The results plotted in Fig. 6.4 show that the measurements correlate to a high degree and the calculated gain corrections are 0.5% and 0.4% for θ_x and θ_y, respectively. These deviations can be explained by manufacturing tolerances and the resulting uncertainty in the transformation matrix (sensor to system coordinates).

Before integration on the final hardware, the actuators have been tested using customized breadboards, as reported in [51]. The force constant, or force sensitivity, was measured to be 5.7 N/A (77 K) resulting in a peak force of 48 N when the used amplifier supplies its maximal (peak) current of 9 A. The actuators can deliver a continuous force of 9 N. The cryogenic actuator constant is 7.9 N/$\sqrt{W}$. As already mentioned, the actuators exhibit hysteretic behaviour which will be discussed in more detail in Section 6.2.3.

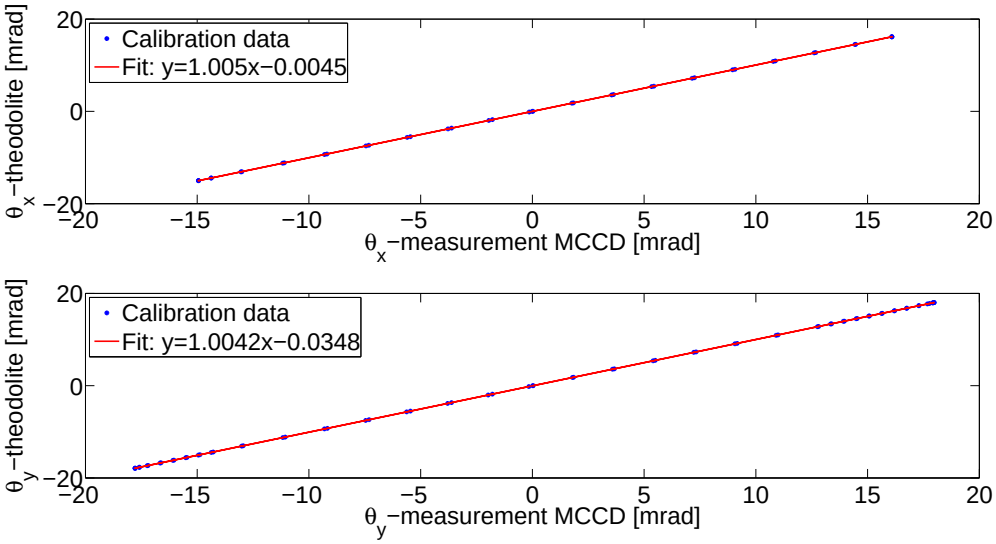

Figure 6.4: Calibration result for both rotation in θ_x and θ_y of the MCCD mirror. Reference measurement was obtained using a theodolite positioned outside the cryostat.

6.2.2 Plant dynamics

System identification is performed by the method of frequency analysis. The experimental data is generated applying a high resolution sinesweep over the frequency regime from 5Hz to 2kHz

and fitting the steady state response of the system (input and output) to a sine profile. This provides us with the phase shift and gain information required to generate the bode plot. We only use the magnitude plot for model fitting because of the limited accuracy of the phase information.

Fig. 6.5 shows the bode magnitude plot of the open loop plant for θ_x. The dominant resonance frequencies of the mechanism are clearly visible. Table 6.1 gives these dominant resonance frequencies and compares them to the results from a detailed Finite Element Analysis (FEA) [17].

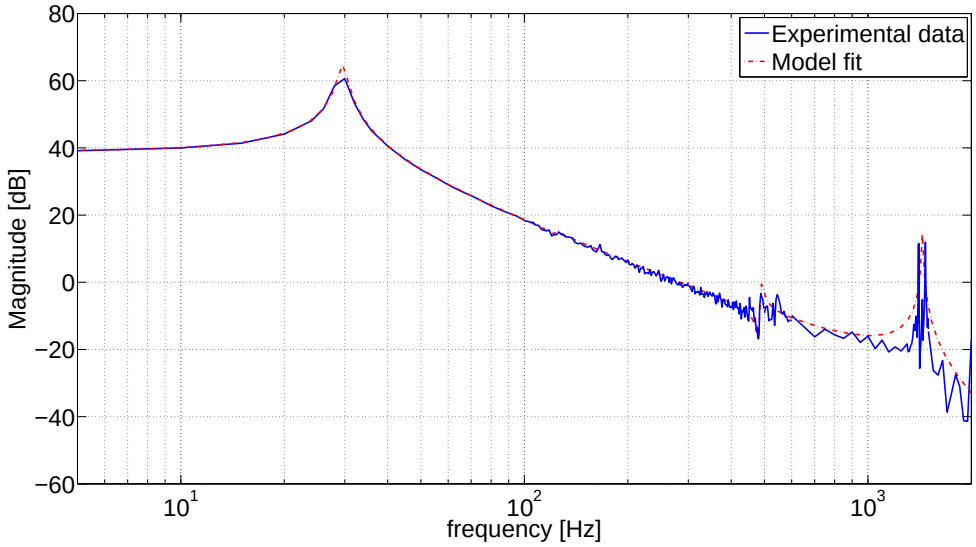

Figure 6.5: Bode magnitude plot of MCCD θ_x dynamics. Experimental data and fitted 8^{th} order model. Experimental data based on sinesweep (Freq. range 5-600 Hz and 1400-1500Hz covered with 5Hz frequency resolution. Other regime covered with 50Hz resolution)

Table 6.1: Dominant resonances of MCCD for θ_x orientation. Experimental and FEA results generated using Creo Simulate and Creo Parametric software

Measured	**FEA**
29.6 Hz	29.0 Hz
1405.0 Hz	1443.1 Hz
1470.0 Hz	1491.0 Hz

The resonant behaviour at approximately 500Hz cannot be explained by the mechanism dynamics. The same is true for a small, but relevant resonance at 125Hz. These resonances do not show up in the FEA and, despite the rotational symmetry of the MCCD, are not present in the θ_y dynamics. They are believed to originate from the test setup e.g., the cryostat, whose

structural dynamics are not symmetrical w.r.t. the introduced forces as a result of θ_x or θ_y-rotation.

Due to the influence of the cryostat, we consider a non collocated lumped mass system as shown in Fig. 6.6 to describe the θ_x-dynamics. This results in an 8^{th}-order system with 5 stable zeros, i.e. 2 complex conjugated pairs close to respectively the 125Hz and the 500Hz resonance and one zero at high frequency. Based on this system, we model the θ_x-dynamics including the dominant resonance at 29.6Hz, a skew notch at 125Hz and at 487Hz and a broad resonance at 1440Hz (to account for the two sharp resonances between 1.4 and 1.5kHz). The high frequency zero has very limited influence on the system response and we choose to ignore this in our system model.

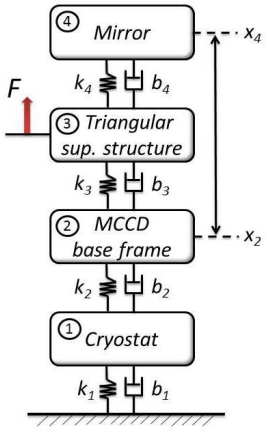

Figure 6.6: Non collocated lumped mass system representative for the dominant 8^{th}-order θ_x-dynamics. The actuator force is applied at the triangular support structure and displacements are measured at the mirror surface relative to the MCCD base frame.

The θ_y-dynamics are modelled as a 4^{th}-order plant excluding the two resonances related to the cryostat. Finally, the z-dynamics are less critical and can be approximated by a 2^{nd}-order plant.

Using the transfer function given by:

$$P(s) = \frac{a_n s^n + a_{n-1} s^{n-1} + ... + a_1 s + a_0}{b_n s^n + b_{n-1} s^{n-1} + ... + b_1 s + b_0} \tag{6.3}$$

where $a_n, ..., a_0, b_n, ..., b_0$ are coefficients to be fitted, the final system models for the differerent DoF's are given in Table 6.2.

Comparison of the simulated step response with experimental data shows a good match for the 1 mrad chop range for which the identification has been performed (see for example Fig. 6.9 (0° offset result)).

A detailed system model, including the weak resonance at 125Hz is required for an accurate FF design. This is discussed in more detail in Section 6.3.1.

Table 6.2: Laplace transform coefficients for all 3 DoF's. The given coefficients are related to the standard transfer function given in (6.3). These are rounded values taken from the 64bit floating point numbers provided by Matlab.

n	P_{θ_x}		P_{θ_y}		P_z	
	a_n	b_n	a_n	b_n	a_n	b_n
0	2.77×10^{27}	3.09×10^{25}	2.53×10^{14}	2.76×10^{12}	1.01×10^{4}	1.59×10^{4}
1	1.00×10^{23}	9.71×10^{21}	-	7.77×10^{8}	-	10.48
2	4.95×10^{21}	9.51×10^{20}	-	8.19×10^{7}	-	1
3	3.72×10^{16}	4.85×10^{16}	-	77.80	-	-
4	5.11×10^{14}	1.60×10^{15}	-	1	-	-
5	-	1.45×10^{10}	-	-	-	-
6	-	1.68×10^{8}	-	-	-	-
7	-	178.5	-	-	-	-
8	-	1	-	-	-	-

6.2.3 Non linear behaviour

The experimental results have revealed the presence of non negligible non linearities in the system. This is shown in Fig. 6.7 where the linear component of the system response is taken out to clearly expose a slightly deformed hysteresis curve.

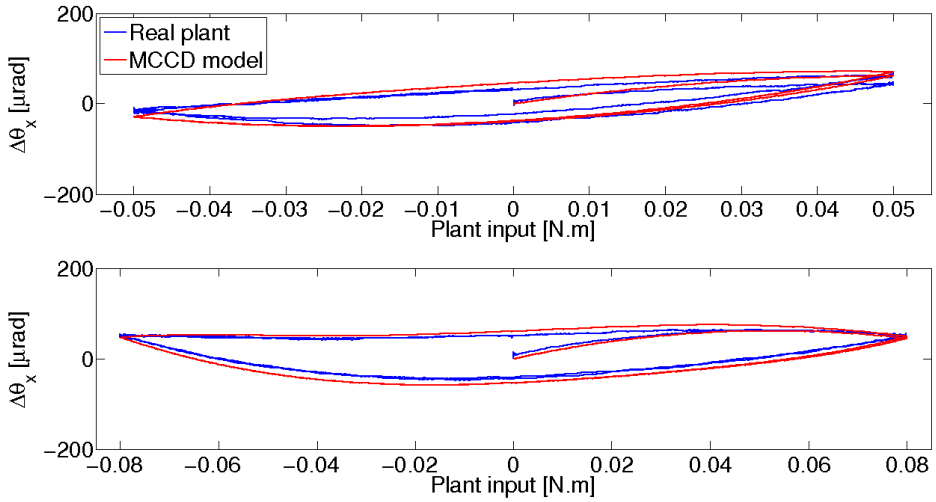

Figure 6.7: Observed hysteresis in θ_x and fitted model for sine inputs spanning different parts of the chop range (0.05Nm input corresponds to 4.5 mrad output, 0.08Nm corresponds to 7.2 mrad). Max. displacement (at 0 input) caused by hysteresis is approx. 0.7% of rotated angle. NB: Linear term of system response is taken out to clearly expose the hysteresis.

As discussed in Section 6.1.1, the hysteresis is caused by the relative displacement of the constant magnetic field, generated by the permanant magnet, with respect to the back iron in the actuators. As a result, the magnetic field strength, at any point in the back iron, depends on the orientation of the chopper, and the back iron material exhibits its magnetic hysteresis curve when the mirror is rotated.

The slight deformation of the hysteresis curve is caused by the position dependent reluctance in the magnetic circuit. The reluctance is maximal in the center position $(\theta = 0)$ and reduces with increasing angle. This introduces negative magnetic stiffness. As the reluctance of the magnetic circuit is inversely proportional to the magnetic field strength, it also makes the force constant of the actuator position dependent.

As discussed in Section 3.3 the hybrid control method includes the design of a feedback controller and of a FF signal. The non linearity has only a small effect on the response of the system and it is not necessary to consider this in the design of the feedback controller. On the other hand, the design of the FF signal is based on a model of the plant. It largely determines the settling time of the mechanism and its performance is directly related to the accuracy of the system model.

In an effort to account for the non linearity in the FF signal design, we have included a Jiles-Atherton (JA) hysteresis model [32] in the system description. The JA model is based on physical laws describing the magnetization process in ferromagnetic materials and is thought to be appropriate for the current application. In parallel we have added a non linear component in the form of a 5^{th} order polynomial to account for the deformation of the hysteresis curve. Fig. 6.8 shows the basic building blocks of the non linear MCCD model. Both operators use the angular orientation of the mechanism as input parameter and affect the input ([N.m]) to the linear plant model.

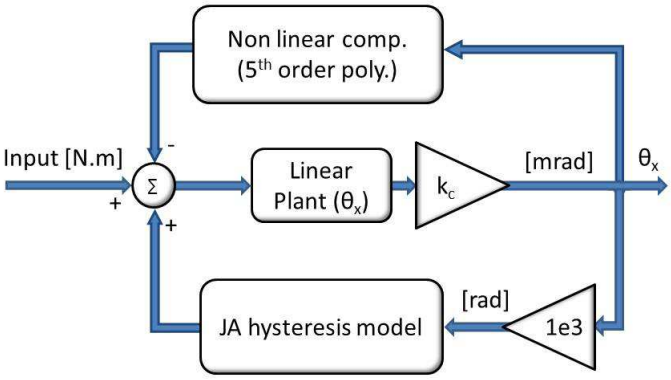

Figure 6.8: Non linear MCCD plant model, including a JA model to represent the hysteresis behaviour in the system and an extra non linear term to account for the observed deformation of the hysteresis curve.

Jiles and Atherton have derived the following relation to describe the changes in the magnetization (M) of the material as a result of variations in the magnetic field strength (H).

$$\frac{dM}{dH} = \frac{(M_{an} - M)}{(1+c)(\delta k/\mu_0 - \alpha(M_{an} - M))} + \frac{c}{(1+c)}\frac{dM_{an}}{dH}, \tag{6.4}$$

where c, k, μ_0 and α are positive real constants and δ is the sign operator. M_{an} is the anhysteretic magnetization and is defined by the following implicit equation

$$M_{an}(H_e) = M_s(coth(H_e/a) - (a/H_e)) \tag{6.5}$$

where $H_e = H + \alpha M$ is the effective magnetic field and M_s and a are positive real constants. It is known that tuning the JA model parameters is a difficult process which is strongly dependent on the choice of initial conditions and often results in non ideal solutions [37]. As we have to include 6 extra parameters in our model to also account for the non linearity, related to the positional dependent force constant of the system, tuning of the complete set of parameters becomes even more of a challenge. We have tuned the parameters by hand, after which we have used Matlabs non linear curve fitting procedure (lsqcurvefit) for fine tuning. This, however, did not result in further optimization of the parameters.

The tuned model parameters are given in Table 6.3. The model response is included in Fig. 6.7. The fit shows the same characteristic response to a sine input for different amplitudes. The accuracy of the model is however limited. This is supported by the experimental results given in Fig. 6.9, showing the response of the system to a FF-input applied at different offset positions in the chop range. The FF input has been generated on the basis of the linear model and has been designed to deliver a 1 mrad step. The response of the linear model (blue line) is independent of the offset position in the chop regime while the experimental result clearly shows the dependence on start position, which indicates hysteresis phenomena have taken place. This hypothesis is corroborated by the simulation result when we include the hysteresis model.

Table 6.3: Parameters of non linear MCCD model. The 2 left most columns give the fitted parameters of the Jiles-Atherton hysteresis model described by (6.4) and (6.5) (the k_c parameter is not part of the JA model). The columns on the right give the fitted coefficients of the 5^{th} order polynomial, which accounts for the positional dependent force constant.

JA parameters	**tuned values**	**Poly. coef.**	**tuned values**
α	1×10^{-3}	p_1	7.289990×10^{-9}
a	0.44	p_2	2.101289×10^{-9}
k	1750.70	p_3	-2.663815×10^{-6}
c	0.22	p_4	8.192315×10^{-6}
M_s	0.44	p_5	1.059444×10^{-4}
k_c	0.99	p_6	1.608167×10^{-3}

The non linear plant model provides valuable insight in the non linear behaviour of the MCCD hardware and fully explains all observed effects. However, from a control design perspective, as the model complexity drastically increases when the hysteresis model (with its 12 parameters) is included, and as the accuracy of the modelled response is limited, we have decided not to use the non linear model for the FF design.

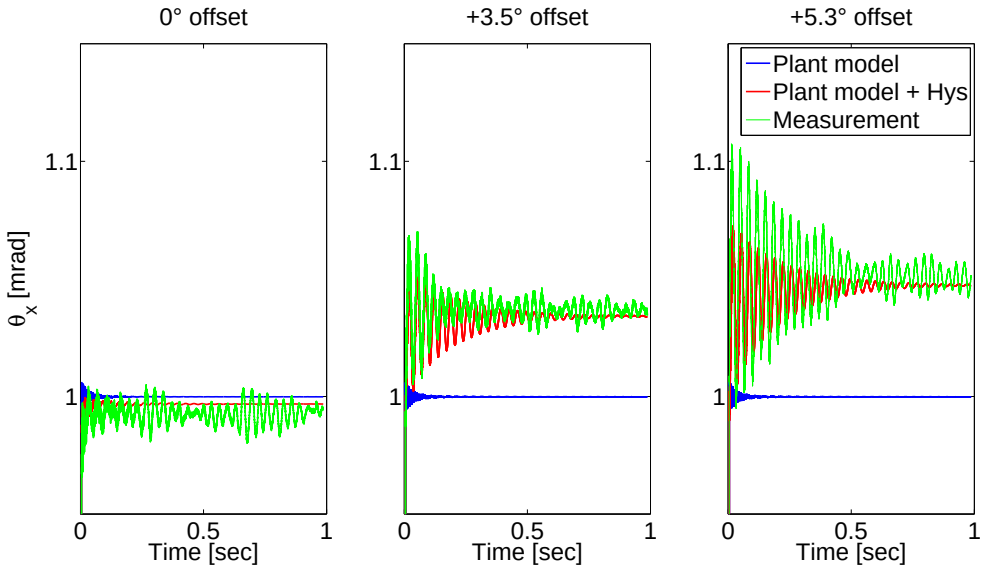

Figure 6.9: Effect of hysteresis on feedforward response (open loop). Comparison between experiment, linear model and model with hysteresis. Close up at end position for: Left: 0 to +1 mrad step Middle: 3.5 to 4.5 mrad step and Right: 5.3 to 6.3 mrad step. NB: Start position is set to zero in all plots for easy comparison.

6.3 Control synthesis

6.3.1 Hybrid controller

In this section we describe the synthesis of the hybrid controller, formulated in Section 3.3, with the MCCD hardware. We separately discuss the issues relating the FF design and the design of a closed loop controller.

FF design

We apply the method described in 3.5 for the design of the FF-signal. Here we discuss some considerations relating the implementation of the method.

We recognize that, because of the high frequency reference signal in relation to the typically limited bandwidth of the closed loop controller, fast settling can only be achieved by accurate FF design and not by error convergence after switching to closed loop. Therefore, we use the full 5 msec settling time specification for our FF signal. This maximizes the number of individual discrete steps of the FF which allows for better norm reduction of (3.11) and it reduces the maximum forces exerted on the mechanism. The effect of which is the reduction of resonant behaviour after the step as a result of model uncertainties and unmodeled dynamics. Furthermore, as this also limits the peak currents generated by the amplifier, this gives the possibility to reduce the amplifier output range. As reduction of the amplifier range typically means reduction of the amplifier noise levels, this has a direct positive effect on the positional stability of the mechanism.

Table 6.4 summarizes the result of a simulation where we apply an accurately designed FF signal based on the 2^{nd}-order MCCD plant model (including only the 29.6Hz dominant mode) to different model plant configurations. This clearly shows the necessity to include the higher order resonances in the FF-design.

Table 6.4: Influence of plant resonances on settling when applying a FF signal based on the 2^{nd}-order plant model for a step from θ_x=0 to 8.5 mrad. The resonances considered in the different plant models are given in the table. NB: The complete 8^{th}-order plant also settles within 4.9 msec when applying a FF signal based on the 8^{th}-order plant model.

Plant model	**Overshoot [μrad]**	**Settling [msec]**
2^{nd}-order (30Hz)	0	4.9
4^{th}-order (30Hz+125Hz)	29	320
4^{th}-order (30Hz+500Hz)	11	72
4^{th}-order (30Hz+1500Hz)	23	80
Complete 8^{th}-order	61	320

Feedback controller

The feedback controller for θ_x has been tuned by loop shaping. It consists of a skew notch filter, to compensate the large phase shift introduced by the dominant resonance at 29.6 Hz, an integrator, required for constant reference tracking and a first order low pass filter for high frequency cut off. The complete controller, discretized by the Tustin method, is then given by:

$$C_{\theta_x} = \frac{0.1722z^4 - 0.3337z^3 - 0.01048z^2 + 0.3337z - 0.1617}{z^4 - 3.311z^3 + 4.085z^2 - 2.228z + 0.4531}$$

In Fig. 6.10, the bode plot of both the sensitivity function $S = (1 + PC)^{-1}$ and the complementary sensitivity function $T = PC(1 + PC)^{-1}$ of the closed loop plant are given. T shows good tracking ability at low frequencies. S is tuned for sufficient amplifier noise and disturbance attenuation below 100 Hz. The slight peaking of the Bode magnitude plot of S above 200 Hz (max. of 4dB at 500Hz) is allowed because of the low sensor noise in the system. The gain and phase margins of the closed loop system are respectively 14.3 dB and 82°, from which we can conclude that the feedback loop is robustly stable. The value of γ, as defined in (10) of [30], is 0.36, so we satisfy the necessary and sufficient condition for output regulation of the hybrid controller.

Because of the symmetry in the system, and because we do not specifically shape the 125Hz and 489Hz resonances, the same controller can be applied to the θ_y DoF. For the control of the z-displacement it suffices to apply a discrete PID controller with $k_p = 89$, $k_i = 1000$ and $k_d = 0.56$ with a 4012.6 filter bandwidth (Forward Euler discretization method).

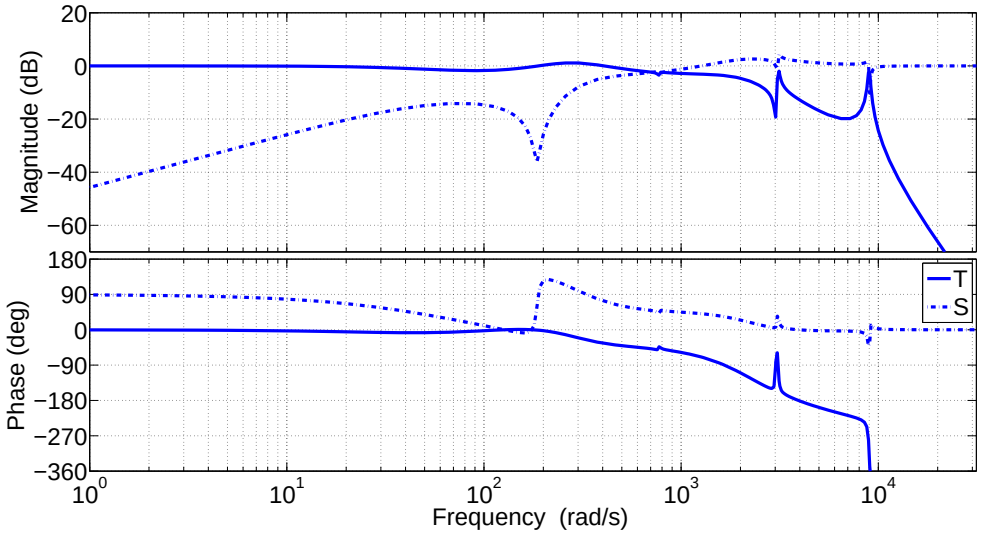

Figure 6.10: Bode plot of complementary sensitivity (T) and sensitivity function (S) of closed loop MCCD plant for θ_x.

6.3.2 Repetitive controller

Fig. 2.1 shows the repetitive control layout as it is applied to the MCCD hardware. The repetitive loop is placed in parallel with the feedback controller described in Section 6.3.1.

In our experiment, as we are interested to explore the maximum settling performance using the repetitive method, we take $Q = 1$. This allows for maximum error reduction at the cost of monotonic convergence. We avoid inversion of S_p but use an inverse of the 4^{th}-order θ_y-dynamics of the plant as our L-filter, where we add a 4^{th}-order Butterworth filter to make the transfer function proper. We are aware that sampling of a continuous time system may lead to the introduction of RHP zeros in the discrete model [4], which in turn can cause problems during system inversion. To avoid this problem we designed the filter in continuous time, after which the L-filter was discretized by the Tustin method. The resulting filter is then given by:

$$L = \frac{0.048z^4 + 6.253e-5z^3 - 0.096z^2 - 2.939e-5z + 0.048}{z^4 - 3.187z^3 + 3.876z^2 - 2.124z + 0.441}.$$

To avoid interference between the feedback controller and the repetitive loop we only close the loop after convergence of the repetitive controller.

Because of the good match between the model and the hardware, we can tune k_r, γ and the cut off frequency of the Butterworth filter offline, and no adjustments of the parameters are needed when we apply the method to the real hardware. NB: The good quality of the learned step input does not introduce significant oscillations after the step. This and the large stability margins of the feedback loop, allow us to further increase the gain of the feedback controller for better amplifier noise and disturbance attenuation. The tuned parameters are given in Table 6.5. The gain of the feedback controller is increased by a factor of 1.5.

Table 6.5: Tuned parameters of repetitive controller for θ_x and θ_y.

DoF	k_r	γ	Cut off freq. [Hz]
θ_x	0.1	8	500
θ_y	0.5	9	500

The reference profile for chopping is generated by applying the method described in [36]. This method generates a smooth 4^{th}-order reference profile while taking into account the limits (maximum jerk etc.) of the plant.

As mentioned in Section 2.3, the reproducibility is generally considered to be a measure for the tracking accuracy that can be attained by repetitive control. The reproducibility of the MCCD for chopping is $\Delta\theta < 10\mu$rad during the step and $\Delta\theta < 2\mu$rad during the integration periods.

In Fig. 6.11 the good match between the simulation and the experimental results is shown. After about 2.4 seconds (12 iterations) the repetitive controller has converged. The effect of activating the feedback controller after 4.7 seconds is clearly visible.

The compensator for θ_x is very similar but here the resonances of the L-filter are matched with the 29.6Hz and 1440Hz resonances of P_{θ_x}.

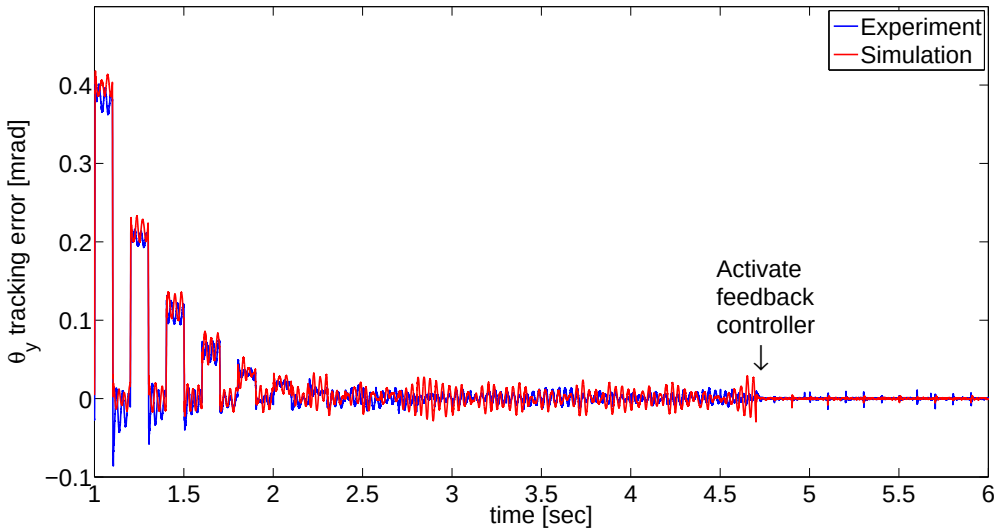

Figure 6.11: Comparison of simulation result with experiment when tracking a 5Hz chopping reference between 0 and 8.5 mrad in θ_y applying the repetitive controller. Error convergence from 1 sec onwards is shown. Feedback controller is activated after 4.7 sec.

We use a practical approach for our repetitive controller design to be able to study its general performance without the need for S_p inversion of the high order plant described in Table 6.2. We are aware that small changes in the response can occur when applying a (zero phase) Q-filter and inversion of S_p. However, for θ_y the tracking error is in the order of the reproducibility of the system which means that for this DoF no further improvements can be made. The performance of the repetitive controller is discussed in Section 6.4. Some considerations about the implementation of the method on the final MCC hardware are discussed in Section 6.5.

6.4 Performance

All tests are performed with the test setup as described in Appendix B. Table 6.6 summarizes the most important test results. All results, except for the settling time are generated applying the hybrid controller. As we use the same feedback controller, most results are applicable to both control strategies. It is well known that the influence of stochastic disturbances (system noise and external vibrations) are amplified by the repetitive method [45]. Because of this the positional stability is worse than for the hybrid approach. However, as discussed in Section 6.3.2, we could compensate for this effect by increasing the loop gain of the feedback controller.

Table 6.6: MCCD requirements and realized performance. Positional stability is defined as 3σ level, all other requirements are defined as absolute maximum.

Description	**Requirement**	**Result**	**Unit**	**Remark**
Pos. stability	$\leqslant 1.7$	$\leqslant 2.09$	[μrad]	3σ
Pos. repeatability	$\leqslant 1.7$	$\leqslant 0.4$	[μrad]	
Pos. accuracy	$\leqslant 85$	$\leqslant 1.04$	[μrad]	
Settling time in θ_x	$\leqslant 5$	32	[msec]	applying
Settling time in θ_y	$\leqslant 5$	5.6	[msec]	rep. control
Parasitic z-disp.	$\leqslant 200$	$\leqslant 3$	[μm]	
Power dissipation	< 1	0.116	[W]	for 5 Hz chop
Peak currents	$\leqslant 10$	2.75	[A]	over 8.5 mrad
Thermal stability	$\leqslant 1.7$	< 1.7	[μrad]	
Lifetime	$> 10^8$	✓	[cycles]	details in Appendix C

Most requirements are satisfied but the positional stability and the settling time specification are not fully met. The results of the test program are described in detail in [28]. In the following sections we summarize some of the critical results related to the performance of the system. The outcome of the lifetime test, which has been performed by JPE after the performace test program, is presented in Appendix C.

6.4.1 Positional stability

Fig. 6.12 shows the 2D positional stability at both observation positions when performing a 0 to +8.5 mrad chop for $\alpha = 0°$ with a chop frequency of 0.5 Hz (α is defined as the chop orientation, with $\alpha = 0°$ defined as rotation around the x-axis and $\alpha = 90°$ rotation around the y-axis). Only the last 0.5 seconds of every 1 second observation is used to allow for settling of the mechanism (applying the hybrid controller). The offsets from the mean position are shown. The red circle gives the 1.7 μrad positional stability limit. In Fig. 6.13 for both DoFs and for both observation positions the offsets from the mean position are shown in a histogram. Here the red line gives the result of a Gaussian fit to the data (applying Matlabs gauss1 fit algorithm and using a bin size of 0.1 μrad).

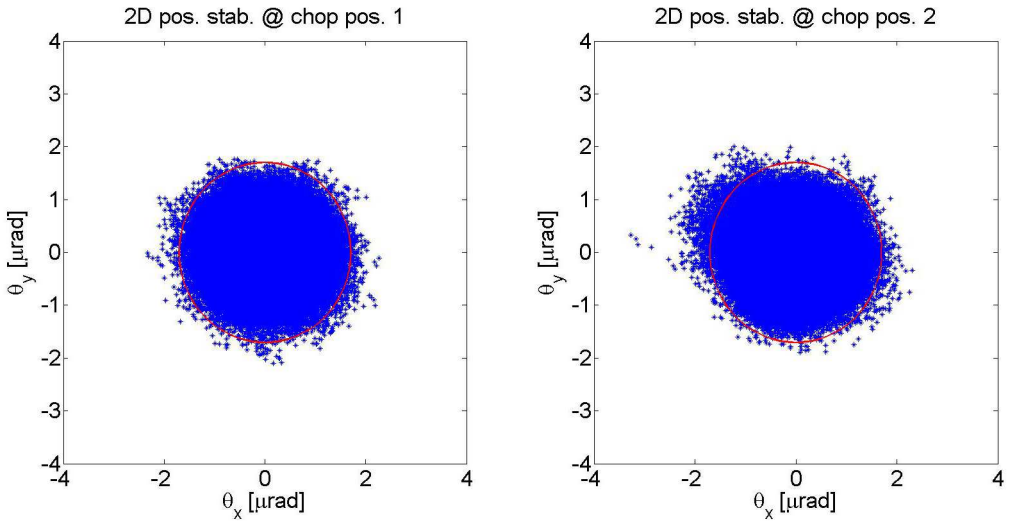

Figure 6.12: 2D positional stability for 0 to +8.5 mrad chopping in the $\alpha = 0°$ direction at both observation positions. Offsets from mean are shown.

The results shown in Fig. 6.12 and 6.13 are representative for all 8.5 mrad chop forms. In Table 6.7 the percentage of data points that lie within the 1.7 μrad circle are given for all standard chop forms at both observation positions. NB: Chopping between -8.5 mrad and +8.5mrad angles is not considered standard but is included for completeness.

We believe that the positional stability can be further improved by fine tuning of the feedback controller in the final setup (when the exact noise and disturbance levels on the E-ELT platform are known), and by reduction of the amplifier range as discussed in Section 6.3.1. In [8] the effectiveness of different strategies to reduce the negative influence of stochastic disturbances on positional stability when applying a repetitive controller is investigated. If required this approach can be considered to further reduce the influence of stochastic disturbances on the positional stability of the plant.

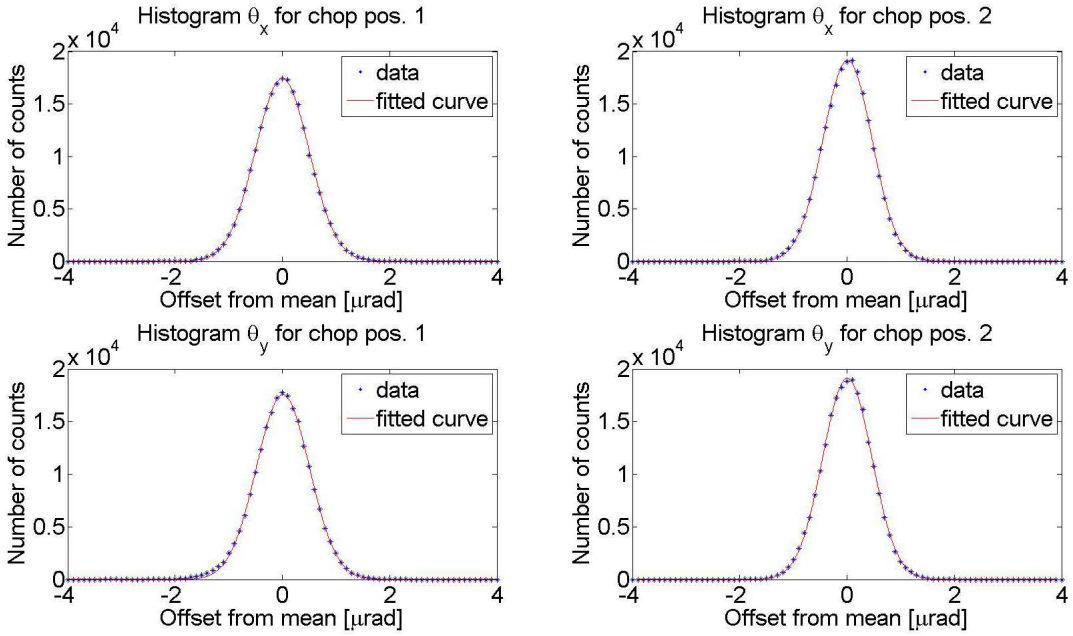

Figure 6.13: Histogram of 2D positional stability for 0 to +8.5mrad chopping. Both DoFs at both observation positions.

Table 6.7: Percentage of chopped angles within 1.7 μrad from mean chopped angle for all standard chop forms. Also included are the results when extending the chop angle to 17 mrad (not a requirement).

α [degrees]	Chop angle [mrad]		Percentage inside 1.7μrad spec [%]	
	Pos1	Pos2	Pos1	Pos2
0	0	+8.5	99.69	99.47
	0	-8.5	99.40	99.49
	-8.5	+8.5	96.91	96.94
120	0	+8.5	98.68	98.18
	0	-8.5	98.00	98.91
	-8.5	+8.5	96.85	96.81
240	0	+8.5	98.20	97.98
	0	-8.5	97.21	96.56
	-8.5	+8.5	96.54	97.44

6.4.2 Settling time

The settling time results given in Table 6.6 are generated by the repetitive controller. Fig. 6.14 shows the result of chopping in θ_y between 0 and 8.5 mrad for both the hybrid and repetitive

method. The hybrid controller converges within 1 chop cycle. The repetitive controller takes about 9 cycles but the settling time is much better. This is illustrated in Fig. 6.15 where a close up of the settling behaviour at the 8.5 mrad position after convergence is given. Since an observation typically takes minutes, the time required for learning (approx. 2 sec) is easily compensated by the much better settling performance of the repetitive controller.

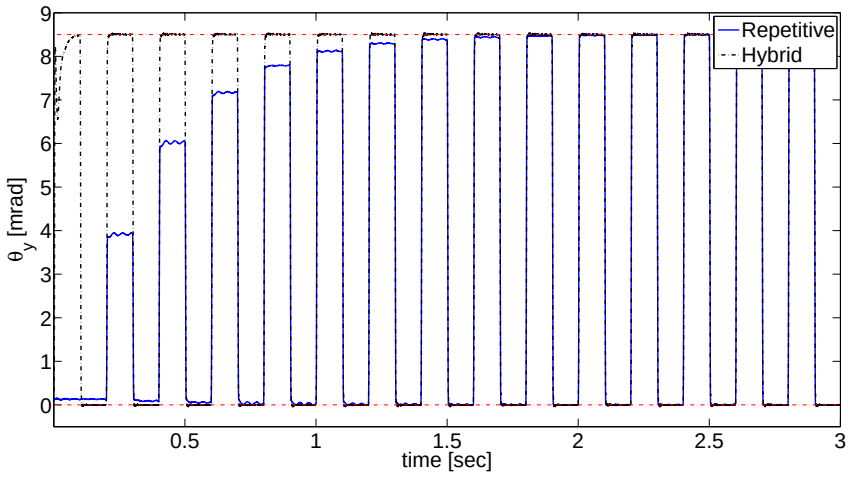

Figure 6.14: Experimental result of 5Hz chopping in θ_y between 0 and 8.5 mrad (indicated by the red dotted lines), applying the hybrid and the repetitive controller.

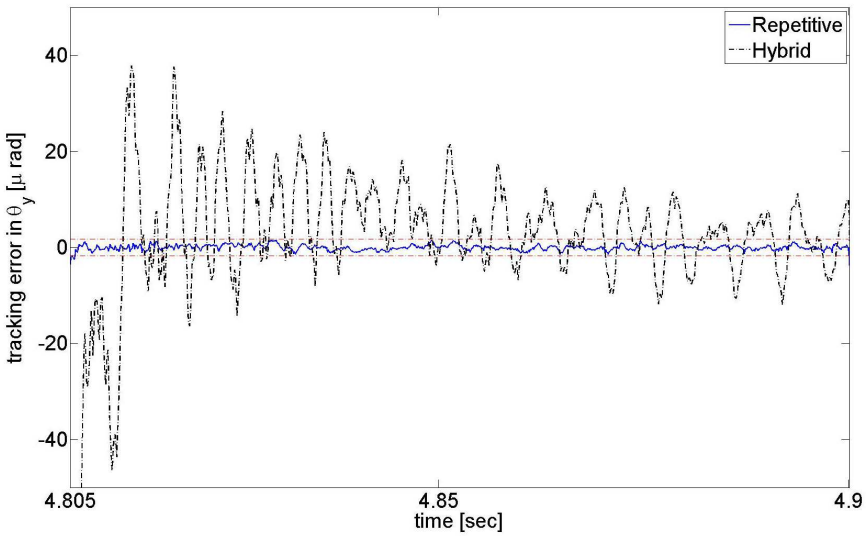

Figure 6.15: Tracking error during 5Hz chop after convergence (after 4.805 sec at θ_y= 8.5 mrad position). Tracking of the hybrid controller is limited due to the non linearities which are not accounted for in the FF design.

As discussed in Section 6.2.3, the quality of the FF signal applied in the hybrid method is limited as a result of the unmodeled non linearities in the system. This limits the performance of any model based FF method. As argued in [40], the linear repetitive controller can deal with the small non linearity in the system and there is no need for adding extra complexity by applying a non linear repetitive controller.

The difference in the settling time for θ_x and θ_y can be explained by the resonant behaviour of the experimental setup at approximately 500Hz, which is only present in the θ_x-dynamics. Including the modelled resonance at 500Hz in the L-filter design for θ_x did not improve performance because of the limited accuracy of the modelled resonance. More detailed modelling is required to correctly compensate for this effect in the L-filter design, but, as the resonance is part of the test setup and not of the MCCD hardware, we did not put further effort into solving this issue. Instead the issue has been taken up with the design engineers of the METIS team recommending to avoid low frequency resonances in the structural interface of the MCC with the METIS instrument.

6.4.3 Robustness to thermal variations

The robustness of the system to internal temperature variations as a result of chopping, was studied by performing a 5 Hz closed loop chop (applying the hybrid controller) for 5 minutes and observing possible drifts in the closed loop trajectory of the mechanism. Fig. 6.16 shows the positional repeatability during this test.

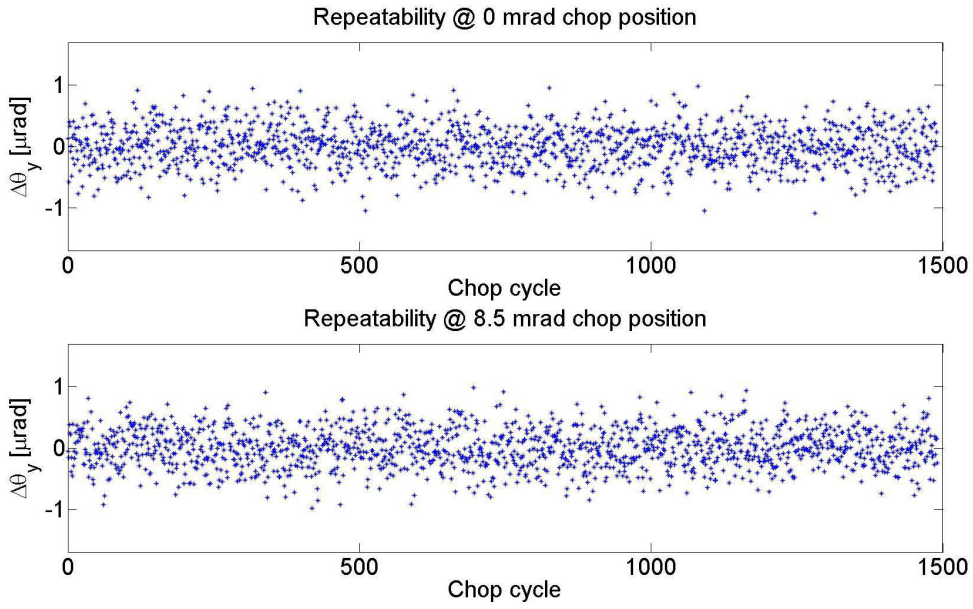

Figure 6.16: Repeatability of chopped positions when performing a 5 Hz chop over an angle of 8.5 mrad for a period of 5 minutes in the θ_y-direction. Every single dot defines the average chop position during a single integration period. No drift in the response is observed as a result of temperature variations in the mechanism.

System stability is preserved and there is no drift observable in the repeatability of the chopped positions. This is in agreement with the results of an open loop sinesweep from 5 to 100 Hz performed at both the operational temperature of 77K and at 63.5K. In Fig. 6.17 the Bode magnitude plots, which are derived from this data, are compared for the θ_x and θ_y-directions. No differences in the frequency response of the system are detected as a result of the temperature changes in the mechanism.

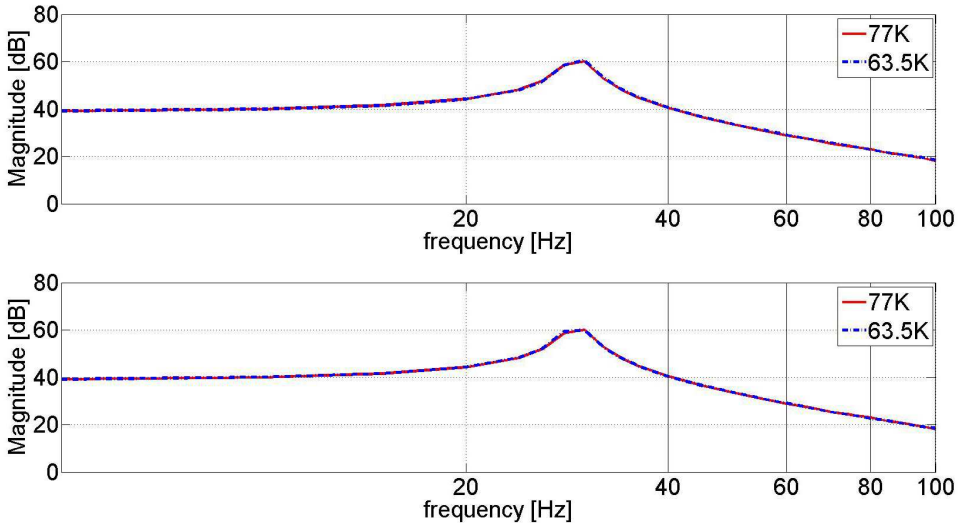

Figure 6.17: Comparison of Bode magnitude plot of plant based on sinesweep at 77K and 63.5K. Top: Result for θ_x-direction. Bottom: Result for θ_y-direction. No variation in response is detectable.

6.5 Implementation issue: Stability of repetitive controller

When applying the repetitive controller we ignore the typical design rule for stability ($|Q(1 - z^{\gamma} S_p k_r L)| < 1$), in order to maximize the learning bandwidth. Stability is of course very important for the delicate hardware, but the necessary use of a Q-filter will limit the learning bandwidth of the repetitive controller. The realizable learning bandwidth strongly depends on the quality of the system identification and the ability of the L-filter to compensate for the resonances within the required learning bandwidth. If for the final hardware fast settling can only be achieved while ignoring the rule of monotonic convergence, the repetitive method will be used to generate a satisfactory input signal, after which the learning is switched off. This signal can then be applied to either the MbFF or the hybrid approach as an FF-input. As discussed in Section 6.3.1, which one to choose will depend on the final system configuration.

We tested this scenario in simulation on the non linear MCCD model by first applying the repetitive controller to the plant for a 0 to 8.5 mrad chop sequence. The repetitive method generates an input signal which we then used as the FF input for both the MbFF and hybrid control strategies. A close up of this simulation at the 8.5 mrad position after 10 seconds of

chopping is given in Fig. 6.18. The different methods show comparable step results, which can be explained by the high accuracy of the FF signal (small positional errors during the step and accurate end position).

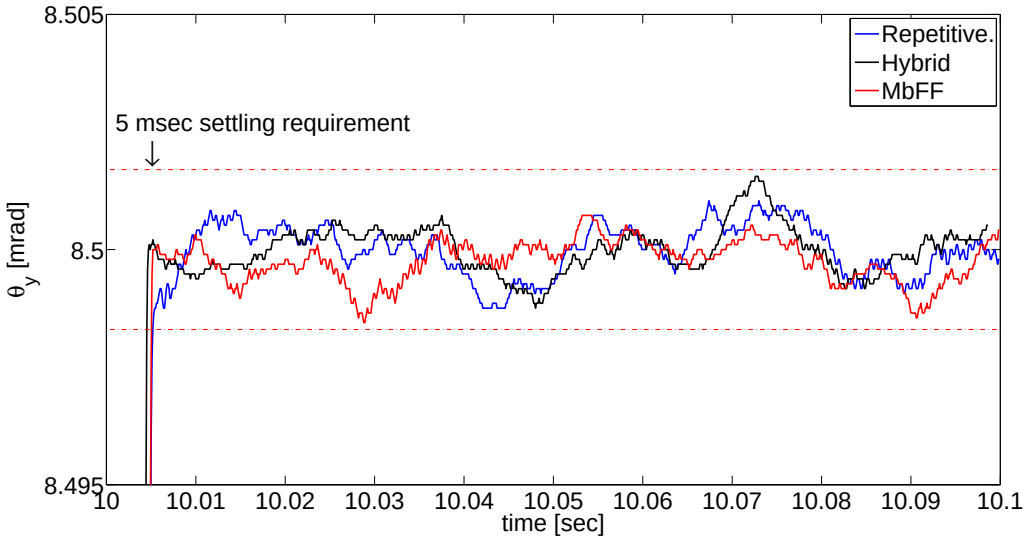

Figure 6.18: Simulation of 5Hz chopping between 0 and 8.5 mrad on the non linear plant, applying the repetitive, MbFF and hybrid controller all using the input signal learned by the repetitive method. Close up at 8.5 mrad position. Result after convergence of the repetitive controller and switching to closed loop. Red dotted lines indicate 1.7 μrad positional stability limits.

6.6 Concluding remarks

We have discussed cryogenic design considerations and presented the mechatronic design of the MCCD. We have tested the performance of the MCCD applying a hybrid control strategy and compared the results to that when using a repetitive controller.

The hybrid control strategy has been developed to eliminate the typical negative effect of the closed loop controller on settling when tracking fast reference profiles applying the standard MbFF technique. Simulation results presented in Section 3.6 show that for the considered plant uncertainties, the hybrid method out performance the MbFF technique when fast reference signals are applied.

The hybrid controller shows good stability robustness to thermal variations in the plant and positional repeatability is not influenced by internal temperature changes in the mechanism.
Early analysis results, during the development phase of the hardware, predicted a settling time of the MCCD mechanism of <6 msec when applying the hybrid controller. These results are presented in [27]. However, at this stage we did not consider the presence of hysteresis in the system.
Detailed system identification revealed the presence of significant non linearities in the mecha-

nism. The developed non linear plant model clearly explains the observed non linear behaviour of the plant. Accurate tuning of the non linear system parameters is however difficult, and the approach was considered to be too complex for implementation in the final hardware. This limits the performance of any MbFF approach (including the proposed hybrid controller).

The results of the repetitive controller are very promising. We applied an open loop learning approach to show the possible performance of the repetitive control strategy without the need for S_p inversion. The repetitive controller can handle the non linearities in the plant. When chopping in the θ_y-direction we reach the reproducibility limit of the system, which means that we make maximum use of its capabilities.
As the repetitive method is a well established control strategy with a firm mathematical background, and as it has shown its applicability to the hardware, this control strategy will be applied to the final MCC mechanism. If satisfying the stability criterion limits the settling performance, the repetitive method will be used for learning of the input signal offline after which this input can be applied as the FF-signal to the MbFF or hybrid method. Because of the high quality of the learned FF-signal both methods show comparable settling time results.

Chapter 7

Conclusions and future work

7.1 Conclusions and outlook

The challenges encountered during the development of the HIFI-FPC, have motivated us to investigate the application of advanced control strategies to cryogenic chopper mechanisms. The demonstrator project of the MCC mechanism provided us with a unique opportunity to develop and verify an advanced control strategy for high performance motion control of cryogenic mechanisms in close collaboration with the various interdisciplinary teams involved in the project.

Chapter 3 is concerned with the development of a hybrid control strategy for high performance motion control of nanopositioning mechanisms. A key aspect of this control strategy is that we perform the step applying FF only. This avoids possible negative influences of the feedback controller on settling time, which for astronomical observations would result in reduced efficiency of the observation.
Although the MCCD only exhibits continuous dynamics, the switch between open and closed loop, the interchanging of memorized control states and the results presented in [42] on hybrid output regulation, have motivated us to cast the problem in the hybrid frame work. This allowed us to define necessary and sufficient conditions to attain hybrid output regulation (during the flow dynamics) for the selected astronomical scanning strategies.
The developed control strategy forms an addition to the field of high performance motion control and can be applied as an alternative to existing methods whenever fast reference profiles (w.r.t. the closed loop system bandwidth) have to be tracked. This is confirmed by the simulation results presented in Section 3.6 and the application of the method to the HIFI-FPC presented in Chapter 5.

Chapter 4 describes the cryogenic design of the HIFI-FPC. We show that the requirement for cryogenic operation limits design freedom and makes testing and calibration of the hardware more challenging. Following from this we have formulated design rules which are generally applicable to the development of cryogenic mechanisms.
Especially for space missions, reliability is the single most important requirement, which justifies a rather rigid and conservative attitude when it comes to the application of new materials as well as actuation and sensing principles. However, the application of advanced control strategies provides a relatively fast and cost efficient way to further optimize performance of these mechanisms. We therefore conclude that the application of advanced control strategies for chopper mechanisms is vital to meet the requirements imposed by the next generation telescopes. The 37% improvement in settling time of the HIFI-FPC, when applying the hybrid controller instead of the original controller, supports this conclusion.

In Chapter 6 we present the system identification, control synthesis (both hybrid and repe-

titive control) and test results of the MCCD hardware. The final performance of the hardware is very good. Most requirements can already be met and the system shows good robustness to temperature variations in the setup.
Hysteresis has manifested itself during the final test campaign of the hardware. It is a side effect of the novel VCA design, which has been optimized to minimize the moving mass and increase the force constant of the actuator. Modelling of the hysteresis has provided us with valuable insight about the characteristics and observed non linear behaviour of the plant but did not result in a system model accurate enough to be used for FF design.
The hybrid controller requires a highly accurate system model for the design of the FF-input, as do all model based FF strategies. We conclude that a controller with the ability to learn (i.e., repetitive control) is more robust to model uncertainties and is therefore essential to meet the stringent requirements on settling time of the mechanism.

The close and interdisciplinary collaboration between the different teams during the development of the MCCD mechanism, has been one of the key ingredients to reach the excellent performance of the final hardware. When developing advanced instrumentation, particularly when involving the highly interdisciplinary field of mechatronics, following an integrated design approach is absolutely essential.

The performed test program described in Chapter 6 concludes the METIS Cold Chopper Demonstrator project. Because of the very promising results when applying the repetitive controller, it has been decided not to change the MCC design significantly for the final hardware. This means no reduction of hysteresis in the actuators. We believe that detailed tuning of the feedback controller in the final setup, and limiting the amplifier range will suffice to meet the positional stability requirement. Recommendations concerning the allowed resonance spectrum of the mechanical interface of the MCCD with the METIS instrument have been provided to the METIS design team. Implementation of these recommendations should avoid problems with the repetitive controller caused by low frequency resonant behaviour of the mechanical interface, as has been observed when chopping in θ_x during the test phase of the MCCD.

7.2 Future work

In this thesis we have adressed the problem of high performance motion control of cryogenic chopper mechanisms for scanning in astronomical observations. Here we discuss some of the issues that follow from the work presented here.

- In Section 3.6 simulation results are provided which for the considered plants show that performing the step with feedforward only results in faster settling when fast reference profiles are being considered. Rigorous analysis to define a criterion for the choice between feedforward only or feedforward in combination with a feedback controller, when applying reference profiles with high frequency content, would improve the applicability of the method.

- The result on hybrid output regulation for scanning (Section 3.4) is only valid for linear plants. The MCCD mechanism clearly shows non linear behaviour. Application of the hybrid control strategy to the MCCD would require the extension of this result to non linear systems and further investigation in the modelling of hysteresis.

- Resetting of the controller to particular initial states at the start of each new flow period is of interest as it can improve the settling time of the system for non ideal FF-inputs. Application of this strategy on real hardware still requires a rigorous proof of hybrid output regulation for scanning and work on the practical implementation of this strategy.
- To be able to study the maximum realizable performance of the repetitive controller, we avoided the use of a Q-filter. The L-filter design was based on the 4^{th} order plant dynamics and during the learning phase of the repetitive loop we did not apply any feedback control. The practical implementation of the repetitive control method on the final MCC hardware requires the use of a non causal Q-filter, inversion of the plant sensitivity function and detailed system identification to locate the relevant resonances of the plant in the final setup. If this results in limited performance of the system, we will consider the combination of repetitive control for FF learning (off line and without the application of a Q-filter) and the use of the hybrid controller (applying the learned FF-input) during operations.
- The actuator design has been optimized to reduce the moving mass and to maximize the force constant of these units. The hysteresis, which is a direct result of the mass reduction, however limits the performance of the hybrid controller. Studying the possibility to minimize hysteresis in the optimization of the actuators would be highly interesting, as repetitive control has its own limitations (e.g., random noise amplification, numerically intensive) and is not applicable for all reference profiles.

Appendix A

Experimental setup HIFI-FPC

The experimental setup that was used to test the hybrid control strategy on the HIFI-FPC, is schematically drawn in Fig. A.1. As the mechanism operates in cryogenic conditions, it is placed in a cryostat and cooled down to 4K. A theodolite was used to calibrate the HIFI-FPC sensors. The original hardware for the HIFI-FPC electronics was not available for the experiments. Therefore, we used custom-made electronics and a real-time dSpace DS1104 platform which is compatible with Matlab (our control software platform). The real setup is shown in Fig. A.2.

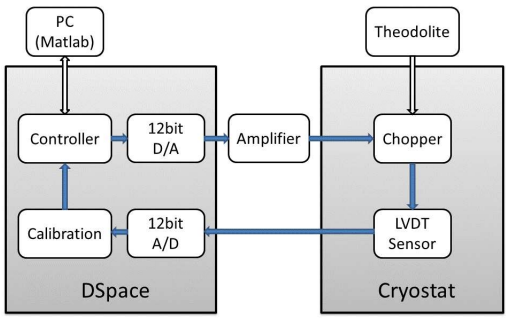

Figure A.1: Schematic drawing of experimental setup for the HIFI-FPC. Tests are performed at cryogenic temperatures.

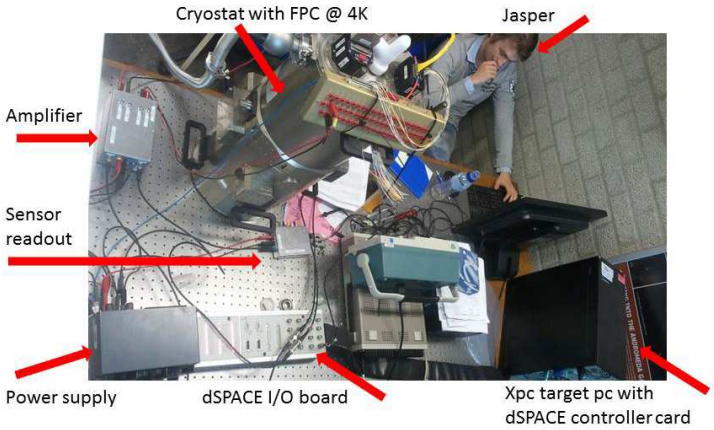

Figure A.2: Photo of HIFI-FPC test setup

Appendix B

Experimental setup MCCD

The experimental setup of the MCCD is sketched in Fig. B.1. Tests are performed in a cryostat at an operating temperature of 77K. The sensor electronics are placed outside the cryostat. The optical measurement signal is guided to the MCCD hardware by 3 glass fibers. Calibration of the 2 DoF rotational motion is performed using a theodolite. The Matlab xPC target platform is used to implement the digital controller (designed in matlab Simulink using a host PC) on a target machine. The system runs at a sampling rate of 10 kHz.

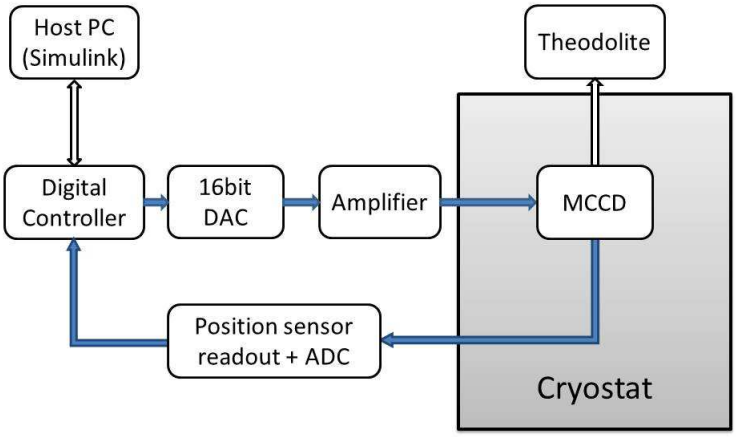

Figure B.1: Block diagram showing the general building blocks of the experimental setup for the MCCD. The MCCD is placed in a cryostat and tests are performed at an operating temperature of 77K.

Appendix C

MCCD lifetime test results

An accelerated lifetime test has been performed by JPE after finalizing all the other scheduled tests, by revolving the chop throw angle of 9 mrad around the z-axis (circular motion path). This motion is considered representative because fatigue depends on amplitude and not on frequency, acceleration, or jerk and it tests all hinges with the maximal stress/strain at the maximal number of cycles unlike a test with actual (random) chop motion. Therefore, the lifetime test represents the worst case load and accounts for manufacturing tolerances and the base material orientation (grain structure).

The test has been executed at 80 Hz, the maximal frequency allowed without overheating the actuators, during the working week while the test ran at 40 Hz during the weekends to avoid manual liquid nitrogen refills. In total the test ran for over 400 hours, but it has been stopped several times to repeat the transfer function measurements and change the operating frequency. These stops are observable in the logged Root-Mean-Square (RMS) chop motion and position error (setpoint position minus actual position) plotted in Fig. C.1 as spikes. The RMS position errors are always below 0.2 mrad and the actual chop throw is above the required chop throw of 8.5 mrad or 6.0 mrad RMS.

Neither the lifetime measurement logs (e.g. chop motion, position error, actuator current and voltage) nor the transfer function measurements revealed any change in stiffness of the flexure suspension or other sign of wear even after completing 100 million cycles. Further testing is recommendable, but the results so far imply that the chopper can meet the lifetime requirement.

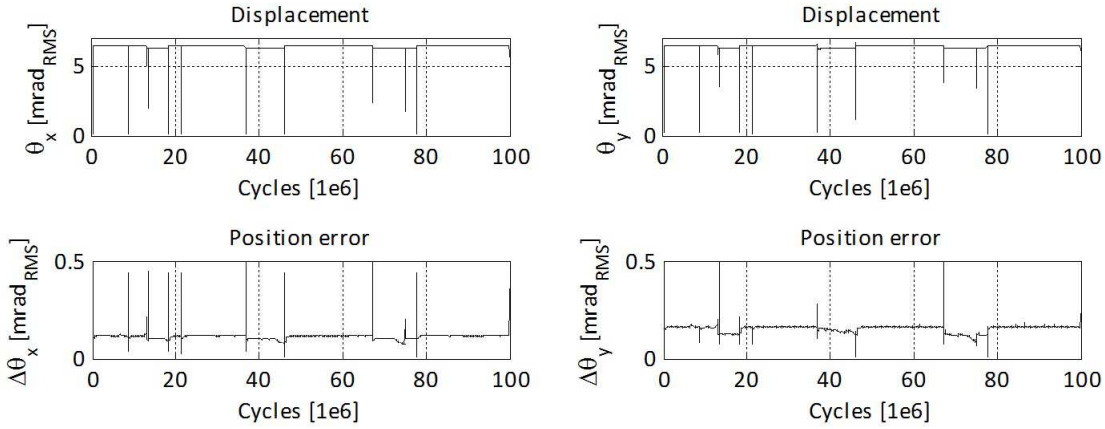

Figure C.1: Lifetime test result showing the RMS chop motion and position error as function of the cycle number for both θ_x and θ_y. This result has been published in [52].

Appendix D

MCCD project summary

The MCC demonstrator project has been initiated to show the feasibility of a high performance chopping mirror inside a cryogenic instrument at an early stage in the METIS development.

D.1 MCCD project objectives

At the start of the program the project objectives have been formulated as follows (quote from MCCD project management plan [47]): *"The purpose of the METIS Cold Chopper Demonstrator (MCCD) is to show the feasibility of the Cold Chopper for the future E-ELT METIS instrument. The accuracy of the METIS measurements will strongly depend on the performance of the chopper. Within this project we will design and build a demonstrator for the METIS chopper in order to verify that the requirements as specified can be met. An important aspect of this program will be the qualification of the control / actuator / sensors / mechanics for a 2-axis system on some breadboards. The project is successful by demonstrating the compliance of the performance of a working demonstrator model, inclusive agreed non conformances. This model will not be used within METIS, it should be reproducible for production several years later without too many changes. This has implications for the choice of the components. As the mechanism needs implementation in METIS, compliance to METIS and ESO requirements is mandatory. This also limits the freedom in selecting the electronics when the components are expected to be critical for the Chopper performance."*

D.2 MCCD project team

METIS is a collaboration between NOVA, UK-ATC, CEA Saclay, ETH Zürich, KU Leuven, MPIA and U Vienna. The MCCD project has been funded by a generous ESFRI grant from NWO as part of the METIS development program. NOVA was responsible for the project management. The design and realization of the MCC hardware (mechanics and electronics) as well as the breadboard, qualification and lifetime testing were the responsibility of JPE BV. The NOVA - optical/infrared instrumentation group was responsible for the system engineering of the project. TNO provided general consultancy. The controller design and the performance test program of the mechanism was a combined effort of the University of Groningen and SRON.

Bibliography

[1] J.W.G. Aalders, K.J. Wildeman, G.R. Ploeger and Z.N. Van Der Meij. New developments with the cryogenic grating drive mechanisms for the ISO spectrometers. Cryogenics, 29: 5502,1989.

[2] J.T. Allison and D.R. Herber. Multidisciplinary design optimization of dynamic engineering systems. American Institute of Aeronautics and Astronautics Journal, 52(4): 691710, 2014.

[3] S. Arimoto, S. Kawamura and F. Miyazaki. Bettering operation of robots by learning. Journal of Robotic Systems, 1: 123-140, 1984.

[4] K.J. Åström, P. Hagander and J. Sternby. "Zeros of sampled systems," Automatica 20(1): 31-38, 1984.

[5] M. Boerlage, M. Steinbuch, P.F. Lambrechts and M. van de Wal. Model based feedforward for motion systems. In Proceedings of the IEEE international conference on control applications, pages 1158-1163, Istanbul, Turkey, 2003.

[6] B.R. Brandl, M. Feldt, A. Glasse, M. Guedel, S. Heikamp, M. Kenworthy, R. Lenzen, M.R. Meyer, F. Molster, S. Paalvast et al. METIS: the mid-infrared E-ELT imager and spectrograph. In SPIE Astronomical Telescopes+ Instrumentation, pp. 914721-914721, International Society for Optics and Photonics, 2014.

[7] D.A. Bristow, M. Tharayil, and A.G. Alleyne. A survey of iterative learning control: A learning-based method for high-performance tracking control. IEEE Control Systems Magazine, 26(3): 96114, 2006.

[8] M. Butcher, A. Karimi and R. Longchamp. A statistical analysis of certain iterative learning control algorithms. International Journal of Control, 81(1): 156-166, 2008.

[9] H. Butler. Position control in lithographic equipment. IEEE Control Systems Magazine 31(5): 28-47, 2011.

[10] T. Chen and B. Francis. Optimal sampled-data control systems. Paragraph 3.1. Springer Verlag, 1995.

[11] J.C. Clegg. A nonlinear integrator for servomechanisms. Transactions of the American Institute of Electrical Engineers, 77 (Part II): 41-42, 1958.

[12] L. Cuiyan, Z. Dongchun and Z. Xianyi. A survey of repetitive control. In Proceedings of 2004 IEEE/RSJ International Conference on Intelligent Robots and Systems, pages 1160-1166, Sendai, Japan, 2004.

[13] S. Devasia. Should model-based inverse inputs be used as feedforward under plant uncertainty? IEEE Transactions on Automatic Control, 47(11): 1865-1871, 2002.

[14] B.G. Dijkstra, N.J. Rambaratsingh, C. Scherer, O.H. Bosgra, M. Steinbuch and S. Kerssemakers. Input design for optimal discrete-time point-to-point motion of an industrial XY positioning table. In Proceedings of the 39th IEEE Conference on Decision and Control, pages 901-906, Sydney, Australia, 2000.

[15] R.C. Dorf and R.H. Bishop. Modern control systems. 11th edition. Pearson Prentice Hall, 2008.

[16] European Southern Observatory. E-ELT instrument roadmap. The E-ELT construction proposal, ESO, C4: 3-32, 2012.

[17] M. Eggens, "Results analysis METIS chopper mirror surface deformation," MCCD project documentation, Doc: SRON-MCCD-RP-2011-00, 2011.

[18] H. Elci, R.W. Longman, M.Q. Phan, J.N. Juang and R. Ugoletti. Simple learning control made practical by zero-phase filtering: Applications to robotics. IEEE Transactions on Circuits and Systems I: Fundamental Theory and Applications, 49(6): 753-767, 2002.

[19] D.T. Emerson. Increasing the yield of our telescopes. International Astronomical Union Symposium, 170: 207-214, 1997.

[20] B.A. Francis and W.M. Wonham. The internal model principle of control theory. Automatica 12(5): 457-465, 1976.

[21] G.F. Franklin, J.D. Powell and A. Emami-Naeini. Feedback control of dynamic systems. 5th edition. Pearson Prentice Hall, New Jersey, 2009.

[22] E. Gmelin, M. Asen-Palmer, M. Reuther and R. Villar. Thermal boundary resistance of mechanical contacts between solids at sub-ambient temperatures. Journal of Physics D: Applied Physics 32(6): R19, 1999.

[23] R. Goebel, R.G. Sanfelice and A.R. Teel. Hybrid dynamical systems. IEEE Control Systems Magazine, 29: 28-93, 2009.

[24] Th. de Graauw, F.P. Helmich, T.G. Phillips, J. Stutzki, E. Caux, N.D. Whyborn, P. Dieleman, P.R. Roelfsema, H. Aarts, R. Assendorp et al. The Herschel-Heterodyne Instrument for the Far-Infrared (HIFI). Astronomy and Astrophysics 518: L6, 2010.

[25] S. Hara, T. Omata and M. Nakano. Synthesis of repetitive control systems and its applications. In 24th IEEE Conference on Decision and Control, pages 326-327, 1985.

[26] R. Huisman, J.W.G. Aalders, M.J. Eggens, J. Evers, H.M. Jacobs, B.J. Van Leeuwen, A.C.T. Nieuwenhuizen, G.R. Ploeger, K.J. Wildeman, B. Jayawardhana and J.M.A. Scherpen. Cryogenic mechatronic design of the HIFI Focal Plane Chopper. Mechatronics 21(8): 1259-1271, 2011.

[27] R. Huisman and B. Jayawardhana. On the design of hybrid output regulation for the METIS cold chopper. In Proceedings of the 7th IFAC Symposium on Robust Control Design, Aalborg, 2012.

[28] R. Huisman. Performance test report METIS Cold Chopper Demonstrator. MCCD project documentation, Doc: TR_MCCD_PT01, 2014.

[29] R. Huisman, S. Paalvast, B. Brandl, T.C. van den Dool, M. Eggens, H. Janssen, G. Aitink-Kroes, F. Molster, M. Teuwen, L. Venema and B. Jayawardhana. High performance motion control of the METIS Cold Chopper Mechanism. 2015, accepted with minor revisions.

[30] R. Huisman, J. Boomer and B. Jayawardhana. Hybrid control synthesis for output regulation with applications to fast motion nano-positioning mechanisms. 2015, under review.

[31] T.K.S.M.T Inoue, M. Nakano, T. Kubo, S. Matsumoto, and H. Baba. High accuracy control of a proton synchrotron magnet power supply. In Proceedings of the 8th World Congress of IFAC, 20: 216-221, 1981.

[32] D.C. Jiles and D.L. Atherton. Theory of ferromagnetic hysteresis. Journal of magnetism and magnetic materials 61(1): 48-60, 1986.

[33] A. Kovács. Scanning strategies for imaging arrays. In SPIE Astronomical Telescopes+ Instrumentation, pages 702007-702007, International Society for Optics and Photonics, 2008.

[34] O. Krause, D. Lemke, R. Hofferbert, A. Böhm, U. Klaas, J. Katzer, F. Höller and M. Salvasohn. The cold focal plane chopper of HERSCHEL's PACS instrument. In SPIE Astronomical Telescopes+ Instrumentation, International Society for Optics and Photonics, pages 627325-627325, 2006.

[35] G. Kroes, R. Ter Horst, J. Kragt, R. Roelfsema, R. Navarro, L. Venema, R. Lenzen, R.R. Rohloff, G. Durand, E. Pantin, S. Rayonett et al. METIS opto-mechanical design and packaging study. In: SPIE Astronomical Telescopes+ Instrumentation. International Society for Optics and Photonics, pages 77352J-77352J-12. 2010.

[36] P.F. Lambrechts, M. Boerlage and M. Steinbuch. Trajectory planning and feedforward design for high performance motion systems. Feedback 14: 15-15, 2004.

[37] D. Lederer, H. Igarashi, A. Kost and T. Honma. On the parameter identification and application of the Jiles-Atherton hysteresis model for numerical modelling of measured characteristics. IEEE Transactions on Magnetics 35: (CONF-9806101–), 1999.

[38] P. Lena. Adaptive optics: a breakthrough in astronomy. Experimental Astronomy 26: 35-48, 2009.

[39] P. Lena, D. Rouan, F. Lebrun, F. Mignard, L. Mugnier, D. Pelat, and S. Lyle. Observational astrophysics. Paragraph 9.4.1. Intrinsic emission from the instrument. 3rd edition, Springer Science & Business Media, 2012.

[40] R.W. Longman. Iterative learning control and repetitive control for engineering practice. International Journal of Control, 73(10): 930-954, 2000.

[41] J.G. Mangum, D.T. Emerson and E.W. Greisen. The on the fly imaging technique. Astronomy and Astrophysics 474(2): 679-687, 2007.

[42] L. Marconi and A.R. Teel. A note about hybrid linear regulation. In 49th IEEE Conference on Decision and Control, pages 1540-1545, Atlanta, Georgia, 2010.

[43] E.D. Marquardt, J.P. Le, R. Radebaugh. Cryogenic material properties database. In Cryocoolers 11, pages 681-687, Springer US, 2002.

[44] G. Martinet, S. Blivet, F. Chatelet, M. Fouaidy, N. Hammoudi, A. Olivier, H. Saugnac. Low temperature properties of piezoelectric actuators used in SRF cavities cold tuning systems. No. CARE-Conf-06-082-SRF, 2006.

[45] R.J.E. Merry, M.J.G. van de Molengraft and M. Steinbuch. Disturbances and model uncertainties in iterative learning control. In IEEE The Fourth International Workshop on Multidimensional Systems (NDS), pages 136-141, 2005.

[46] Military Handbook 5J. Metallic Materials and Elements for Aerospace Vehicle Structures. Paragraphs 2.3, 3.6.2, 6.3.5. Department of Defence, Washington DC, USA, 2003.

[47] F. Molster. MCCD project management plan. MCCD project documentation, Doc: MCC_PL_0001 Projectplan 2.0, 2011.

[48] T. Nakagawa, H. Matsuhara and Y. Kawakatsu. The next-generation infrared space telescope SPICA. In SPIE Astronomical Telescopes+ Instrumentation, pages 84420O-84420O. International Society for Optics and Photonics, 2012.

[49] D. Nešić, A.R. Teel, G. Valmorbida and L.Zaccarian. Finite-gain $\mathcal{L}_p$ stability for hybrid dynamical systems. Automatica, 49(8): 2384-2396, 2013.

[50] V. Ossenkopf. Optimization of mapping modes for heterodyne instruments. Astronomy & Astrophysics 495(2): 677-690, 2009.

[51] S.L. Paalvast, H. Janssen, M. Teuwen, R. Huisman, B. Brandl, F. Molster and L. Venema. Development of a 2D precision cryogenic chopper for METIS. In Proceedings of SPIE, 8450: 845020-845021, 2012.

[52] S.L. Paalvast, R. Huisman, B. Brandl, H. Janssen, B. Jayawardhana F. Molster, M. Teuwen and L. Venema. Development and characterization of a 2D precision cryogenic chopper for METIS. In SPIE Astronomical Telescopes+ Instrumentation, pages 91510D-91510D, International Society for Optics and Photonics, 2014.

[53] L.Y. Pao and W.E. Singhose. Robust minimum time control of flexible structures. Automatica 34(2): 229-236, 1998.

[54] G.L. Pilbratt, J.R. Riedinger, T. Passvogel, G. Crone, D. Doyle, U. Gageur, A.M. Heras, C. Jewell, L. Metcalfe, S. Ott and M. Schmidt. Herschel Space Observatory. An ESA facility for far-infrared and submillimetre astronomy. Astronomy and Astrophysics 518: L1, 2010.

[55] J.H. Pragt, R. Van Den Brink, G. Kroes, N. Tromp, J.B. Ochs. Piezo-driven adjustment of a cryogenic detector. In: SPIE Astronomical Telescopes+ Instrumentation, pages 70184N-70184N, International Society for Optics and Photonics, 2008.

[56] D. Roover and F. Sperling. Point-to-point control of a high accuracy positioning mechanism. In Proceedings of the American Control Conference 3: 1350-1354, Albuquerque, U.S.A., 1997.

[57] G.H. Sanders. The thirty meter telescope (tmt): An international observatory. Journal of Astrophysics and Astronomy 34(2): 81-86, 2013.

[58] T. Singh and W. Singhose. Tutorial on input shaping/time delay control of maneuvering flexible structures. In Proceedings of the American Control Conference, IEEE, 3: 1717-1731, 2002.

[59] W. Singhose, N. Singer and W. Seering. Comparison of command shaping methods for reducing residual vibration. In Proceedings of European control conference, pages 1126-1131, Rome, 1995.

[60] W. Singhose. Command shaping for flexible systems: A review of the first 50 years. International Journal of Precision Engineering and Manufacturing, 10(4): 153-168, 2009.

[61] W. Singhose and J. Vaughan. Reducing vibration by digital filtering and input shaping. In IEEE Transactions on Control Systems Technology 19(6), 2011.

[62] O.J.M. Smith. Posicast control of damped oscillatory systems. Proceedings of the IRE 45(9): 1249-1255, 1957.

[63] H. van de Stadt and J. Verkerk. Large chopping secondary mirror for the 15-m submillimeter James Clerk Maxwell telescope. Applied Optics 26(16): 3446-3454, 1987.

[64] J.P.W. Stark. The spacecraft environment and its effect on design. In Spacecraft Systems Engineering. Pages 11-39, Wiley, 2003.

[65] Y.-G. Sung and W.E. Singhose. Robustness analysis of input shaping commands for two-mode flexible systems. Control Theory and Applications, IET 3.6: 722-730, 2009.

[66] M. Tomizuka. Zero phase error tracking algorithm for digital control. ASME Journal of Dynamic Systems, Measurement and Control, 109: 65-68, 1987.

[67] D.E. Torfs, R. Vuerinckx, J. Swevers and J. Schoukens. Comparison of two feedforward design methods aiming at accurate trajectory tracking of the end point of a flexible robot arm. IEEE Transactions on Control Systems Technology, 6(1): 1-14, 1998.

[68] K. Youcef-Toumi. Modeling, Design, and Control Integration: A Necessary Step in Mechatronics. IEEE/ASME Transactions on Mechatronics, 1(1): 29-38, 1996.

[69] T. Tuma, A. Pantazi, J. Lygeros and A. Sebastian. Nanopositioning with impulsive state multiplication: A hybrid control approach. IEEE Transactions on Control Systems Technology, 21.4: 1352-1364, 2013.

[70] M. Uchiyama. Formulation of high-speed motion pattern of a mechanical arm by trial (in Japanese). Transactions of the Society for Instrumentation and Control Engineers, 14: 706-712, 1978.

[71] J. Vaughan, A. Yano, and W. Singhose. Comparison of robust input shapers. Journal of Sound and Vibration 315(4): 797-815, 2008.

[72] J.R. Wertz, W.J. Larson. Space mission analysis and design. 3rd edition, Space Technology Library, 1999.

[73] K.J. Wildeman, D.A. Beintema, G.R. Ploeger, D. Snel, J.J. Wijnbergen. Grating drive for the short-wavelength spectrometer in ISO. Cryogenics 27: 68-72, 1987.

[74] Q.Zou, K.K. Leang, E. Sadoun, M.J. Reed and S. Devasia. Control issues in highspeed AFM for biological applications: Collagen imaging example. Asian Journal of Control 6(2): 164-178, 2004.

Summary

This dissertation investigates the application of advanced control strategies to the field of chopper mechanisms for scanning in astronomical observations. To deal with noise sources and environmental influences during an astronomical observation and for the purpose of mapping an extended source, it is beneficial to use a chopper mechanism in the optical path of the scientific instrument which collects the light from the telescope. This mechanism can change the orientation of the beam on the sky (referred to as scanning) without the need to rotate the complete telescope or secondary mirror. The constant development towards bigger and better telescopes is reflected on the instrumentation and demands for ever increasing performance requirements of these chopper mechanisms. The requirements on positional stability, reproducibility and settling time are extremely high and, from a control perspective, belong to the field of high performance motion control of nanopositioning mechanisms.

To limit thermal radiation, these mechanisms are often cooled to cryogenic temperatures (< 100 K). This has a huge impact on the design, testing and operation of the hardware. The use of materials, actuation and sensing principles, lubricants and hinges for instance is limited. We describe the cryogenic design of the HIFI Focal Plane Chopper and we formulate rules applicable to the development of cryogenic mechanisms.

The extreme demands on reliability of the hardware hampers the introduction of new materials and principles in this field of engineering. Application of advanced control strategies does not require specific hardware development and can form a fast and cost efficient way to further improve the performance of cryogenic chopper mechanisms.

The motivation for this work comes from the Focal Plane Chopper (FPC) for the Heterodyne Instrument for the Far Infrared (HIFI), which during its development phase confronted us with a number of challenges to be able to meet its performance requirements. The Mid-Infrared E-ELT Imager and Spectrograph (METIS) Cold Chopper (MCC) mechanism has provided a unique opportunity to develop and test advanced control strategies capable of meeting the demands defined by the METIS instrument and the European-Extremely Large Telescope (E-ELT). We developed our control strategy in close collaboration with the other members of the MCCD project team in an integrated design approach. This is an absolute necessity for the development of such advanced instrumentation.

Typical astronomical scanning profiles combine very fast stepping maneuvers with stable or slow scan profiles during periods of integration on the source (or background). We developed a hybrid control method which guarantees output regulation during the integration periods

of these scan profiles. By performing the step applying feedforward only, we avoid possible negative influences of the feedback controller on the accuracy of the point-to-point motion. We provide necessary and sufficient conditions to satisfy the chopper scanning control problem and we prove that inaccuracy in the feedforward signal can never destabilize the hybrid system (practical stability).

We tested the performance of our hybrid control strategy on both the HIFI-FPC and the MCCD mechanism. The HIFI-FPC results show an improvement of 37% in settling time when applying the hybrid controller instead of the original controller. The applicability of the hybrid controller on the MCCD mechanism is limited because of the presence of hysteresis in the mechanism. The hysteresis is a side effect of the optimization of the VCA design, which was intended to reduce the inertia of the mirror body. Modelling of the hysteresis provided valuable insight about the characteristics of the mechanism, but did not result in a model which was accurate enough to be used for feedforward design. Inaccuracy in the plant model limits the performance of any model based feedforward technique and motivated us to test the applicability of repetitive control.

The repetitive controller is insensitive to the non linearities in the system and shows performance results which are very close to the stringent requirements set on the MCCD hardware. We have provided recommendations for final adjustments to the system which we believe will result in a MCC mechanism which will perform within specification on the final E-ELT METIS platform.

The herein developed hybrid control strategy forms an addition to the field of high performance motion control and can be applied as an alternative to existing methods whenever fast reference profiles (w.r.t. the closed loop system bandwidth) have to be tracked.

Samenvatting

In dit proefschrift wordt de toepassing van geavanceerde regelalgoritmes voor de aansturing van chopper mechanismen in astronomische observatie-instrumentatie onderzocht. De toepassing van een chopper mechanisme in het optische pad van het wetenschappelijke instrument in het focus van de telescoop, maakt het mogelijk te corrigeren voor ruisbronnen en omgevingsinvloeden. Verder vindt het chopper mechanisme toepassing in het op efficiënte wijze in kaart brengen van een uitgebreide bron. Tijdens een waarneming kan middels het chopper mechanisme de kijkrichting van de telescoop veranderd worden (het zogenaamde "*scannen*") zonder dat hiervoor de gehele telescoop of de secundaire spiegel gedraaid hoeft te worden. De ontwikkeling van steeds grotere en meer geavanceerde telescopen wordt weerspiegeld in de ontwikkeling van de instrumentatie en stelt steeds strengere eisen aan deze chopper mechanismen. De toepassing van geavanceerde regelalgoritmes vormt een belangrijk gereedschap om de extreme eisen aan positionele stabiliteit, reproduceerbaarheid en staptijd van toekomstige chopper mechanismen op een snelle en efficiënte manier verder te optimaliseren. Deze toepassing behoort tot het onderzoeksgebied van *high performance motion control* voor nanopositioneringsmechanismen.

Om thermische straling zoveel mogelijk te onderdrukken wanneer waarnemingen in het infrarood worden uitgevoerd, is het belangrijk om het chopper mechanisme te koelen tot cryogene temperaturen (< 100 K). Deze keuze heeft grote consequenties voor het ontwerp en de testprocedures. Ook het gebruik van bepaalde materialen, actuator- en sensorprincipes, smeermiddelen en scharnieren is beperkt. Verder vertragen de extreme betrouwbaarheidseisen die aan deze mechanismen worden gesteld, de introductie van nieuwe materialen en principes in dit veld. De toepassing van geavanceerde regelalgoritmes is daarentegen onafhankelijk van deze beperkingen.

De motivatie voor dit onderzoek vormde de Focal Plane Chopper (FPC) voor de Heterodyne Instrument for the Far Infrared (HIFI), en de uitdagingen die gepaard gingen met de ontwikkeling van dit mechanisme. Het Mid-Infrared E-ELT Imager and Spectrograph (METIS) Cold Chopper (MCC) mechanisme was een unieke kans om geavanceerde regelalgoritmen te ontwikkelen en te testen om aan de prestatie-eisen opgelegd door het METIS instrument en de European-Extremely Large Telescope (E-ELT) te voldoen. De hier beschreven regelstrategie werd ontwikkeld in nauwe samenwerking met de overige leden van het MCCD project team, de zogenaamde "*integrated design approach*". Deze aanpak is absoluut noodzakelijk bij de ontwikkeling van dergelijk geavanceerde instrumentatie.

De hybride control strategie, die werd ontwikkeld voor het MCCD mechanisme, garandeert *output regulation* tijdens integratieperioden. In veel scanprofielen wordt een snelle stap afgewisseld met een stabiele of langzame scan tijdens de integratieperioden op de bron (of tijdens een achtergrond meting). Door de stap uit te voeren met behulp van alleen een *feedforward* regelaar, voorkomen we mogelijk negatieve effecten van *feedback* regeling op de stap-nauwkeurigheid. In dit proefschrift worden noodzakelijke en voldoende condities gedefinieerd om te voldoen aan het "*chopper scanning control problem*". Daarbij wordt het bewijs geleverd dat onnauwkeurigheid in het *feedforward* signaal in geen geval kan leiden tot destabilisatie van het hybride systeem (zogenaamde "praktische stabiliteit").

De prestaties van de hybride regelstrategie werden getest op zowel de HIFI-FPC als op het MCCD mechanisme. Voor de HIFI-FPC heeft dit geresulteerd in een verbetering van de staptijd met 37%. Voor het MCCD mechanisme werd de toepasbaarheid van de hybride regelaar beperkt door de aanwezigheid van hysterese in het mechanisme. Deze hysterese was een bijeffect van de actuator optimalisatie met als doel een verlaging van het traagheidsmoment van het spiegellichaam. De modellering van de hysterese heeft geleid tot een dieper begrip van het gedrag van het mechanisme, maar heeft niet geresulteerd in een voldoende nauwkeurig systeemmodel om het *feedforward* signaal te kunnen tunen. Beperkte nauwkeurigheid van het systeemmodel heeft een negatieve invloed op de prestaties van elke *feedforward* strategie die op dit systeemmodel baseert. Dit vormde de motivatie om de toepasbaarheid van de repeterende regelmethode te testen.

De repeterende methode is ongevoelig voor het niet-lineaire gedrag van het systeem. Bij toepassing van deze methode benaderen de prestaties van het MCCD mechanisme de strenge eisen die aan de MCCD hardware gesteld zijn. Met een paar laatste kleine aanpassingen aan het uiteindelijke ontwerp is het daarom zeer waarschijnlijk dat het mechanisme binnen specificaties zal functioneren op het E-ELT METIS platform.

De ontwikkelde hybride regelstrategie vormt een aanvulling op het gebied van de *high performance motion control* en kan toegepast worden wanneer snel variërende referentie profielen (t.o.v. de *closed loop* systeem bandbreedte) moeten worden gevolgd.